



UNIVERSITÀ DEGLI STUDI DI SALERNO
FACOLTÀ DI SCIENZE MATEMATICHE, FISICHE E NATURALI

Dipartimento di Fisica "E.R. Caianiello"

Tesi di Dottorato di Ricerca in Fisica

X ciclo - Nuova Serie (2008-2011)

**Nb nanoporous ultrathin films:
matching effects and interconnected wires**

Michela Trezza

Advisor:

Prof. Carmine Attanasio

Università degli Studi di Salerno

Coordinatore:

Prof. Giuseppe Grella

Università degli Studi di Salerno

Contents

Introduction	1
Bibliography	5
1 Theoretical and experimental background	9
1.1 Brief review of superconductivity	10
1.2 Key properties of vortices	15
1.3 Superconducting nanostructures for controlling vortex dynamics	17
1.3.1 Pinning due to antidots	18
1.3.2 Magnetic dots	27
1.4 Superconductivity in one dimension	37
1.4.1 Phase slips in one dimension	38
1.4.2 Free energy barrier	40
1.4.3 Appearance of resistance in 1D superconducting wire	44
1.4.4 Quantum phase slips	52
1.4.5 Other properties of 1D superconducting nanowire	59
Bibliography	67
2 Fundamentals of porous silicon and applications	75
2.1 History of porous silicon	75
2.2 Basics of the porous silicon formation process	77
2.2.1 Electrochemical etching of porous silicon	77
2.2.2 Chemistry of the formation of porous silicon	80

2.2.3	Pore size and morphology	83
2.2.4	Anodization parameters	85
	Bibliography	89
3	Matching effects: experimental results	93
3.1	Evidence of fractional matching states	94
3.1.1	Sample fabrication	96
3.1.2	Experimental results and discussion	97
3.2	J_c enhancement due to antidots	109
3.2.1	Sample fabrication	110
3.2.2	Experimental results and discussion	112
	Bibliography	117
4	Vortex pinning with artificial magnetic nanostructures	121
4.1	Introduction	121
4.2	Sample fabrication	123
4.3	Experimental results and discussion	127
	Bibliography	133
5	1D superconductivity in porous Nb ultrathin films	135
5.1	Introduction	135
5.2	Sample fabrication	137
5.3	Experimental results and discussion	138
5.3.1	Resistive transition	139
5.3.2	I - V measurements	142
	Bibliography	145
	Conclusions	149
	Publications	151

Introduction

When the applied magnetic field is higher than the lower critical field but below the upper critical field, a type-II superconductor allows magnetic flux to penetrate it in the form of vortices, a tiny normal area surrounded by supercurrents. Driven by the Lorentz force of a passing external current or by thermal activation, vortices can move. Their motion induces energy dissipation and eventually can destroy the superconductivity. Recent advances in nanofabrication have led to tremendous possibilities for implementing superconducting pinning structures and controlling the motion of vortices. The dynamics of vortices in confined superconducting geometries has generated much interest, including studies of fundamental properties about vortex matter and devices based on the motion of the vortices. During the past decades, a lot of efforts have been devoted to introducing artificial pinning centers into superconductors to stabilize and pin the vortex lattice against the external driving force, thus giving rise to higher critical currents [1–10]. This is of practical importance since superconductors are required to maintain high critical currents for potential technological applications. Generally there are two different kinds of artificial pinning centers. The first one are the random imperfections, for example heavy-ion radiation damage [11], cold work induced dislocations [12], disordered hole arrays [13–15], etc. The other one are periodic defect arrays such as antidots (holes) [1–4, 7, 16], dots [6], and magnetic dots [5, 17, 18].

Recent advances in micro- and nanofabrication technologies have made possible to produce superconductors with carefully controlled arrays of artificial defects [4–10, 19–21] with pores size and interpore spacing comparable to the relevant length scales of

superconductors such as the coherence length $\xi(T)$ and the penetration depth $\lambda(T)$, which are generally under submicron scales. As one of the most efficient and easiest methods, introducing periodic hole arrays into superconducting films has attracted much interest [4, 7–9]. Moreover, superconducting films containing periodic hole arrays also provide a unique platform to understand vortex motion and pinning in the presence of regular pinning centers. The interplay between the periodic pinning forces and the elastic repulsive vortex-vortex interaction generates a variety of novel vortex phenomena such as the commensurate effect [19, 22], the rectification and phase locking of the vortices [20], composite fluxline lattices [23], which are not observed in the continuous superconducting films.

The commensurate effect between the vortex lattice and the underlying periodic artificial pinning array is one of the intriguing properties in superconducting films with periodic hole arrays [7, 8, 23, 24]. It appears as minima in the magnetic field dependence of the resistance, $R(H)$, or as maxima in the field dependence of the critical current, $I_c(H)$, when the vortex lattice is commensurate with the underlying periodic artificial pinning array, i.e., when the external magnetic field corresponds to integer multiples or fractions of the so-called first matching field H_1 . This effect is normally interpreted as a result of the pinning enhancement [25–28], i.e., vortices are more difficult to move at matching fields. Thus, a pinning enhancement occurs and high critical current (or resistance minima) are achieved. A similar effect has also been observed in superconducting wire networks [29–31]. The wire networks are one dimensional (1D) multiconnected superconducting thin strips whose width w is comparable to the superconducting coherence length $\xi(T)$. So, a superconducting film containing a periodic hole array can resemble a superconducting wire network at temperatures close to T_c . Both these mechanisms have been used to interpret the commensurability effects observed in transport measurements on superconducting films containing an array of holes at temperatures close to T_c . For example, in aluminum films containing periodic hole arrays, Fiory et al. associated the magnetoresistance oscillations to commensurate vortex pinning [1], whereas Pannetier et al. attributed these oscillations to wire

network properties [30]. In order to understand the related physics and for possible applications, it is necessary to distinguish these two mechanisms and identify the real origin of the commensurability effect.

This thesis presents some investigation of vortex dynamics in superconducting Nb ultrathin films with different artificial pinning centers: magnetic and non-magnetic. Evidence of 1D superconductivity observed in these structures will be also discussed.

In chapter 1, after a brief introduction to the main aspects of the superconductivity, the relevant concepts of the vortex dynamics, such as flux-flow resistivity and the vortex pinning, are discussed. Implementation of artificial defects, including pinning holes, magnetic dots, and different pinning arrangements of periodic and quasi-periodic pinning arrays, are presented. Finally the basics of 1D superconductivity are introduced.

In chapter 2 the different stages of the porous silicon formation are explained. The anodization parameters that influence the final characteristics of the fabricated layers are also discussed and the porous silicon photoluminescence is briefly described.

In chapter 3 transport properties of perforated Nb ultrathin films deposited on porous silicon are presented. Resistive transitions and critical current measurements as a function of the applied magnetic field show matching effect between the vortex lattice and the structure of the pinning array.

In chapter 4 the electromagnetic interaction between the vortex lattice and magnetic pinning centers in Nb films deposited on nanoporous Al_2O_3 substrates containing an array of Ni nanowires was investigated by transport measurements in the presence of magnetic field applied perpendicularly to the samples surface. The (H, T) phase diagram was studied for these systems and compared to the one of a plain Nb film.

In chapter 5, resistive transitions and current-voltage characteristics measured on perforated Nb ultrathin bridges deposited on porous Si are reported. Due to the reduced dimensions of the pores diameter as well as of the interpore distance the experimental observations strongly call to mind features of 1D superconductivity.

Bibliography

- [1] A.T. Fiory, A.F. Hebard, and S. Somekh, *Appl. Phys. Lett.* **32**, 73 (1978).
- [2] A.N. Lykov, *Solid State Commun.* **86**, 531 (1993).
- [3] A. Castellanos, R. Wördenweber, G. Ockenfuss, A.v.d. Hart, and K. Keck, *Appl. Phys. Lett.* **71**, 962 (1997).
- [4] V.V. Moshchalkov, M. Baert, V.V. Metlushko, E. Rosseel, M.J. van Bael, K. Temst, Y. Bruynseraede, and R. Jonckheere, *Phys. Rev. B* **57**, 3615 (1998).
- [5] M.J. Van Bael, K. Temst, V.V. Moshchalkov, and Y. Bruynseraede, *Phys. Rev. B* **59**, 14674 (1999).
- [6] A. Hoffmann, P. Prieto, and I.K. Schuller, *Phys. Rev. B* **61**, 6958 (2000).
- [7] U. Welp, Z.L. Xiao, J.S. Jiang, V.K. Vlasko-Vlasov, S.D. Bader, and G.W. Crabtree, *Phys. Rev. B* **66**, 212507 (2002).
- [8] T.C. Wu, P.C. Kang, L. Horng, J.C. Wu, and T.J. Yang, *J. Appl. Phys.* **95**, 6696 (2004).
- [9] S. Raedt, A.V. Silhanek, M.J. Van Bael, R. Jonckheere, and V.V. Moshchalkov, *Physica C* **404**, 298 (2004).
- [10] J. Hua, Z.L. Xiao, D. Rosenmann, I. Beloborodov, U. Welp, W.K. Kwok, and G.W. Crabtree, *Appl. Phys. Lett.* **90**, 072507 (2007).

-
- [11] L. Civale, A.D. Marwick, T.K. Worthington, M.A. Kirk, J.R. Thompson, L. Krusin-Elbaum, Y. Sun, J.R. Clem, and F. Holtzberg, *Phys. Rev. Lett.* **67**, 648 (1991).
- [12] J.W. Ekin, *J. Appl. Phys.* **62**, 4829 (1987).
- [13] J. Hua, Z.L. Xiao, D. Rosenmann, I. Beloborodov, U. Welp, W.K. Kwok, and G.W. Crabtree, *Appl. Phys. Lett.* **90**, 072507 (2007).
- [14] M. Trezza, S.L. Prischepa, C. Cirillo, R. Fittipaldi, M. Sarno, D. Sannino, P. Ciambelli, M.B.S. Hesselberth, S.K. Lazarouk, A.V. Dolbik, V.E. Borisenko, and C. Attanasio, *J. Appl. Phys.* **104**, 083917 (2008).
- [15] M. Trezza, S.L. Prischepa, C. Cirillo, and C. Attanasio, *Europhys. Lett.* **88**, 57006 (2009).
- [16] J. Eisenmenger, M. Oettinger, C. Pfahler, A. Plettl, P. Walther, and P. Ziemann, *Phys. Rev. B* **75**, 144514 (2007).
- [17] J.I. Martín, M. Vélez, J. Nogués and I.K. Schuller, *Phys. Rev. Lett.* **79**, 1929 (1997).
- [18] M. Vélez, J.I. Martín, J.E. Villegas, A. Hoffmann, E.M. Gonzáles, J.L. Vincent and I.K. Schuller, *J. Magn. Magn. Mater.* **320**, 2547 (2008).
- [19] U. Welp, Z.L. Xiao, V. Novosad, and V.K. Vlasko-Vlasov, *Phys. Rev. B* **71**, 14505 (2005).
- [20] J. Van de Vondel, C.C. de Souza Silva, B.Y. Zhu, M. Morelle, and V.V. Moshchalkov, *Phys. Rev. Lett.* **94**, 57003 (2005).
- [21] G.R. Berdiyrov, M.V. Milosevic, and F.M. Peeters, *Phys. Rev. B* **74**, 174512 (2006).

-
- [22] V.V. Metlushko, U. Welp, G.W. Crabtree, Zhao Zhang, S.R.J. Brueck, B. Watkins, L.E. DeLong, B. Ilic, K. Chung, and P.J. Hesketh, *Phys. Rev. B* **59**, 603 (1999).
- [23] M. Baert, V.V. Metlushko, R. Jonckheere, V.V. Moshchalkov, and Y. Bruynseraede, *Phys. Rev. Lett.* **74**, 3269 (1995).
- [24] K. Harada, O. Kamimura, H. Kasai, T. Matsuda, A. Tonomura, and V.V. Moshchalkov, *Science* **274**, 1167 (1996).
- [25] Z. Jiang, D.A. Dikin, V. Chandrasekhar, V.V. Metlushko, and V.V. Moshchalkov, *Appl. Phys. Lett.* **84**, 5371 (2004).
- [26] W. Vinckx, J. Vanacken, V.V. Moshchalkov, S. Mátéfi-Tempfli, M. Mátéfi-Tempfli, S. Michotte, and L. Piraux, *Eur. Phys. J. B* **53**, 199 (2006).
- [27] A. Terentiev, D.B. Watkins, L.E. De Long, L.D. Cooley, D.J. Morgan, and J.B. Ketterson, *Phys. Rev. B* **61**, 9249 (2000).
- [28] M. Velez, D. Jaque, J.I. Martin, F. Guinea, and J.L. Vicent, *Phys. Rev. B* **65**, 94509 (2002).
- [29] A. Bezryadin and B. Pannetier, *J. Low Temp. Phys.* **98**, 251 (1995).
- [30] A. Bezryadin and B. Pannetier, *J. Low Temp. Phys.* **102**, 73 (1996).
- [31] A.N. Grigorenko, G.D. Howells, S.J. Bending, J. Bekaert, M.J. Van Bael, L. Van Look, V.V. Moshchalkov, Y. Bruynseraede, G. Borghs, I.I. Kaya, and R.A. Stradling, *Phys. Rev. B* **63**, 052504 (2001).

Chapter 1

Theoretical and experimental background

In this chapter, firstly a brief review of the superconductivity is presented, including the Meissner effect, the phenomenological description of superconductivity, the Ginzburg-Landau theory and the BCS microscopic theory. I also discuss the vortex response in a superconductor and the relevant concepts for describing vortex dynamics, such as the flux-flow resistivity and the vortex pinning by defects. I continue with a review of some recent results connected to the pinning in superconductors. Both theoretical and experimental investigations will be included. I discuss different implementations of artificial pinning in superconducting films, including holes, magnetic dots, and different arrangements of periodic and quasi-periodic pinning arrays. Then I introduce the basics of superconductivity in one dimension (1D). A review of the studies on 1D superconducting wires will be presented. I discuss various theoretical proposals and the corresponding experimental implementations.

1.1 Brief review of superconductivity

One hundred years ago on April 8, 1911, H. Kamerlingh Onnes discovered superconductivity in liquid helium in Leiden, where zero resistivity of mercury was measured (Fig. 1.1) [1]. In his notebook, he wrote *resistance practically zero*. He referred to the phenomenon of zero resistivity as *superconductivity*. Subsequent measurements of the resistance for other materials at the liquid helium temperature were performed, and many metals and alloys were found to be superconducting below a well-defined critical transition temperature T_c . A second fundamental hallmark associated with a superconductor is the exclusion of magnetic flux, discovered by W. Meissner and R. Ochsenfeld in 1933. The combination of zero resistance and perfect diamagnetism results in a clear distinction between a superconductor and a hypothetical perfect conductor; this difference involves the different response that each would have for different histories of cooling below the transition temperature and applying a magnetic field. If we start by cooling through T_c and then apply a magnetic field, both the superconductor and the perfect conductor would exclude the field.

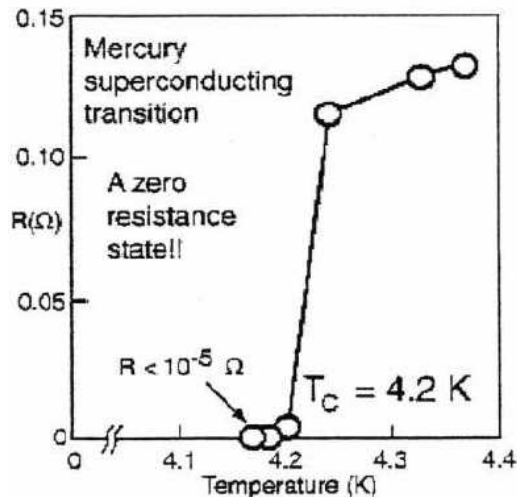


Figure 1.1: Resistive transition of mercury as measured by Kamerlingh Onnes.

If we reverse the order by first applying the field and then cooling through T_c , the

superconductor and the perfect conductor behave differently, the superconductor excludes the flux whereas the perfect conductor would remain fully permeated by the field. These observations argue that the transition associated with superconductivity is a phase transition independent of its history.

However, perfect conductivity, and with it the Meissner effect, does not persist to arbitrarily high magnetic fields [2]. For each temperature there is a well-defined critical field $H_c(T)$, at which superconductivity disappears. Figure 1.2 shows an universal curve of the temperature dependence of H_c . The temperature dependence of the critical field H_c , for many superconductors, is well described by the empirical relation

$$H_c(T) = H_c(0) \left[1 - \left(\frac{T}{T_c} \right)^2 \right] \quad (1.1)$$

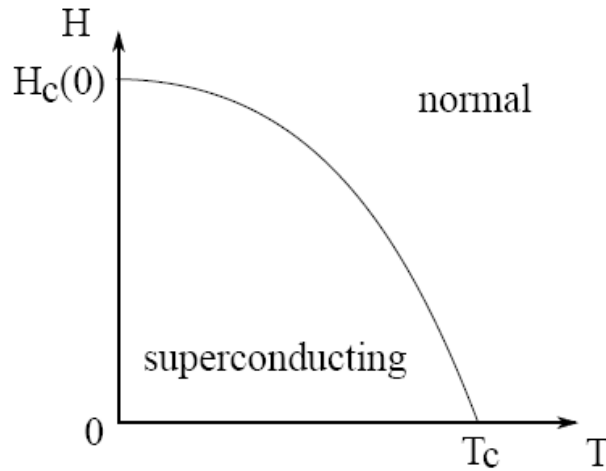


Figure 1.2: *The temperature dependence of the critical field.*

The first successful phenomenological theory of superconductivity was published in 1935 by brothers F. and H. London. Their theory described two basic electrodynamic properties of superconductivity concerning the characteristics of a perfect conductivity and the Meissner effect. The second London equation also introduced the penetration depth $\lambda(0)$, characterizing a length scale over which a magnetic field exponentially decreases into the superconductor at zero temperature. The temperature dependence

of $\lambda(T)$ in terms of $\lambda(0)$ can be written, as the temperature approaches T_c , as

$$\lambda(T) = \lambda(0) \left(1 - \frac{T}{T_c}\right)^{-1/2} \quad (1.2)$$

In 1952, V.L. Ginzburg and L. Landau (GL) introduced a mathematical theory of the superconducting phase transition which does not purport to explain the microscopic mechanisms giving rise to superconductivity. Instead, it examines the macroscopic properties of a superconductor with the aid of general thermodynamic arguments. Ginzburg and Landau argued that the free energy of a superconductor near the superconducting transition can be expressed in terms of a complex order parameter ψ which described how deep into the superconducting phase the system is. In the GL theory the electrons that contribute to superconductivity were proposed to form a superfluid. In this interpretation $|\psi|^2$ indicates the fraction of electrons that has condensed into a superfluid. The GL equations produce many interesting and valid results. The most important of these is its prediction of the existence of another characteristic length in a superconductor: the coherence length ξ which characterizes the distance over which the superconducting order parameter can vary. The coherence length ξ is found to diverge as the temperature approaches T_c according to the expression:

$$\xi(T) = \xi(0) \left(1 - \frac{T}{T_c}\right)^{-1/2} \quad (1.3)$$

The ratio $\kappa = \lambda/\xi$ is known as the Ginzburg-Landau parameter. It has been shown that type-I superconductors are those with $0 < \kappa < 1/\sqrt{2}$ and type-II superconductors ones with $\kappa > 1/\sqrt{2}$. For type-II superconductors the phase transition from the normal state is of the second order, whereas for type-I it is of the first order.

In 1957, based on the GL theory, Abrikosov proved the existence of a so-called mixed state in type-II superconductors. In this mixed phase, above the first transition

field H_{c1} , an increase in the flux density is expected until the magnetic field reaches another critical field H_{c2} , eventually destroying the superconductivity and entering the normal state (Fig. 1.3). H_{c1} is called the lower critical field and H_{c2} is the upper critical field.

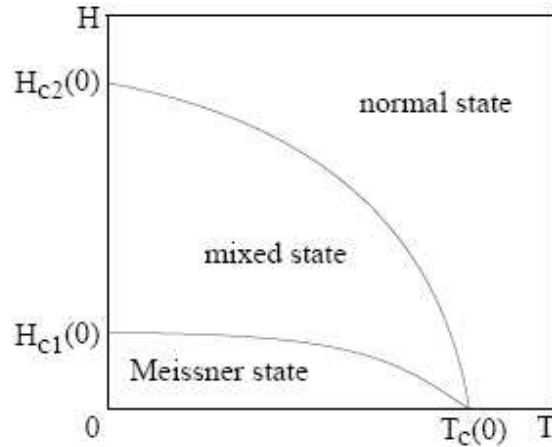


Figure 1.3: Phase diagram for a type-II superconductor.

Abrikosov found that in type-II superconductors in a high magnetic field, the field penetrates in quantized tubes of flux which are most commonly arranged in a hexagonal array as a consequence of a negative normal-superconductor interfacial energy. In order to maximize the contribution of interface energy, flux penetrates the superconductor in many discrete flux quanta or *fluxons*, each fluxon containing a single flux quantum given by

$$\Phi_0 = \frac{h}{2e} = 2.07 \times 10^{-15} Tm^2 \quad (1.4)$$

The structure of a fluxon consists of a short-range (of order ξ) normal core, where the order parameter vanishes, surrounded by a long-range (of order λ) vortex of supercurrent.

Later, L.N. Cooper first, and J. Bardeen and J.R. Schrieffer (BCS) then, introduced

the concept of the *Cooper pairs* in 1957 and the microscopic theory of superconductivity finally moved a revolutionary step [3]. At the superconducting state, electrons tend to bind in pairs, thereby they have a lower energy level than in the Fermi-sea ground state. BCS theory starts from the assumption that there is some attraction between electrons, which can overcome the Coulomb repulsion. An electron moving through a conductor will attract the nearby positive charges in the lattice. This deformation of the lattice causes another electron, with opposite spin, to move into the region of higher positive charge density. The two electrons then become correlated due to the Pauli exclusion principle. The electrons in Cooper pairs interact by exchanging phonons. The BCS theory predicted that a minimum energy $E_g = 2\Delta(T)$ is required to break the Cooper pairs. $\Delta(T)$ is the energy gap between the ground state and the quasi-particle excitations of the system and it is of the order of $k_B T_c$, where k_B is the Boltzmann constant. BCS theory correctly predicts the Meissner effect and the variation of the penetration depth with temperature. It also describes the variation of the critical magnetic field with temperature and relates the value of the critical field at zero temperature to the value of the transition temperature and the density of states at the Fermi energy. Moreover, the BCS theory reproduces the isotope effect, which is the experimental observation that, for a given superconducting material, the critical temperature is inversely proportional to the isotopic mass of the constituent element. In 1959, Gorkov was able to show that the GL theory is a limiting form of the BCS theory when the temperature is close to T_c [4].

1.2 Key properties of vortices

As described previously, each vortex in type-II superconductors is surrounded by a circulating screening current. The vortices in a bulk superconductor are subject to a repulsive force from neighboring vortices due to the interaction with the circulating currents. As the applied magnetic field is increased further beyond H_{c1} , the density of fluxons increases, and vortex-vortex repulsion, when the vortex space is comparable to the penetration depth λ , leads to the formation of a triangular array in order to maintain the lowest energy of inter-vortex interaction. The triangular lattice constant a_0 can be described as:

$$a_0 = \left(\frac{2}{\sqrt{3}} \right)^{1/2} \sqrt{\frac{\Phi_0}{B}} \quad (1.5)$$

where B is the applied magnetic field.

In the presence of a transport current density J the flux line lattice of a superconductor in the mixed state experiences a bulk Lorentz force $\mathbf{F}_L = \mathbf{J} \times \mathbf{B}$. The Lorentz force will cause the vortex motion, leading to energy dissipation and a non zero resistance. So, the flux flow of vortices leads to a dissipation, which can be characterized by the vortex viscosity:

$$\eta = \frac{\Phi_0 H_{c2}}{\rho_n} \quad (1.6)$$

where ρ_n is the normal-state resistivity of the material. However, fluxons are easily pinned by regions of weaker superconductivity, such as microstructural defects. A vector sum of these elementary pinning forces (f_p) opposes the Lorentz force.

In order to have a type-II superconductor suitable for technological applications, so that it can carry high currents in the presence of the flux line without or with

little dissipation, the flux lines have to be pinned. This can be achieved usually by artificial means, such as dislocations, heavy-ion radiation damage, grain boundaries, etc. More recently, with the development in nanofabrication, submicron pinning holes or magnetic dots have been implemented in superconducting thin films in order to increase pinning force. When a perpendicular magnetic field is applied, the field induces vortices to enter the sample and their movement causes the resistance increases significantly. However, at certain special applied fields, the period of the vortex lattice coincides with the one of the hole array, resulting in a very stable state with all vortices pinned by the holes. Both the density and mobility of free vortices drop dramatically to a level comparable to the zero field situation. The commensurate effect is one of the intriguing properties in superconducting films with periodic hole arrays [5–8]. It appears as minima in the magnetic field dependence of the resistance, $R(H)$, or as maxima in the field dependence of the critical current, $I_c(H)$, when the vortex lattice is commensurate with the underlying periodic artificial pinning array, i.e., when the external magnetic field corresponds to integer multiples or fractions of the so-called first matching field H_1 , where $H_1 = \Phi_0/A$ is defined as one flux quantum, $\Phi_0 = h/2e$, per unit cell area, A , of the pinning array. This effect is normally interpreted as a result of the pinning enhancement [9–11], i.e., vortices are most difficult to move at matching fields. Thus, a pinning enhancement occurs and high critical current (or resistance minima) can be achieved.

When a vortex is near the inhomogeneities in superconductors, the force between the vortex and the defect tends to pin the vortex in place. A calculation carried out by Mkrtychyan and Schmidt [12] shows that it is always energetically favorable for a vortex to be attracted by a cavity in the superconductors before the number of trapped vortices reaches a critical value, which largely depends on the superconductor and the cavity parameters. With vortices pinned in the pinning centers, the superconductors can now sustain a finite current without flux motion and dissipation. The current at which the threshold force is required to cause vortex motion is referred to as the *critical current*.

The experimental implementation of artificial pinning sites in superconducting films will be discussed in more detail in the next section.

1.3 Superconducting nanostructures for controlling vortex dynamics

Reducing the dissipation in type-II superconductors caused by the motion of vortices is an important issue for scientists. In order to achieve the lower dissipation, increasing the vortex pinning would be the first intuitive way to do so. Therefore a larger pinning force f_p and a larger critical current density J_c will be achieved in the superconductors, which can be useful for practical applications. Recent advances in nanofabrication have enabled implementations of artificial periodic vortex pinning lattices in superconducting films. Such structures are typically produced with defect arrays such as nanoscale holes through the film [5, 7, 13–18], dots [19], and magnetic dots [20–24]. These structures result in a substantial magnetic field dependence of the critical current.

The critical current in periodic pinning structures typically exhibits commensurate behavior with maxima when the applied magnetic field H corresponds to one flux quantum, Φ_0 , per unit cell area, a_0^2 , of the pinning array, assuming that it is square. Here a_0 is the lattice constant of the pinning arrangement. For fields far from these matching values, the dynamics of interstitial vortices, which are not located on the strong pinning sites but are more weakly confined through interactions with the strongly pinned vortices, lead to lower critical currents. Recently, a wide variety of experiments have been performed on such pinning arrays.

1.3.1 Pinning due to antidots

One approach for controlling the vortex motion in superconductors is to create submicron holes by using lithographic and etching techniques. These submicron holes are usually referred to as *antidots* in the thin films, which act as well-defined pinning centers. Mkrtchyan and Shmidt studied theoretically the interaction between a vortex and an antidot in a type-II superconductor [12]. Under the assumption that the hole radius is $r \ll \lambda$, where λ is the penetration depth, capturing a single vortex by the pore is always energetically favorable. After a vortex has been captured, the vortex free energy undergoes a qualitative change, and it may result in a potential barrier between the vortex and the cavity so that the capture of subsequent vortices in the cavity largely depends on the superconductor and the cavity parameters, which could be energetically favored or not.

Therefore, the commensurate effect is often observed in superconductors containing periodic defect arrays. This effect represents itself as minima in the field dependence of the resistance, $R(H)$ [25], or maxima in the field dependence of the critical current $J_c(H)$ [13, 15, 18, 26–28] at certain particular magnetic fields, $H_n = nH_1$, where H_1 is the first matching field, n is an integer which corresponds to the flux quantum number in each unit cell (Fig. 1.4). In some cases, the commensurate effect can also be observed even when n is a fractional number [29, 30]. An antidot with diameter \emptyset can trap at least one vortex [12, 31, 32], though the presence of the Bean-Livingstone barrier around the holes makes the entrance of a fluxon in some cases very difficult, especially at low temperature [29]. If the holes are sufficiently large, they can pin multiquanta vortices [32] up to a *saturation number* n_S given by $n_S = \emptyset/4\xi_S(T)$, where $\xi_S(T)$ is the temperature dependent superconducting coherence length [12]; it is defined as the maximum number of vortices that fits into a pore with diameter \emptyset . Therefore, the limiting number of the flux lines which can be pinned by a hole can be controlled by varying temperature (in this way $\xi_S(T)$ varies) or by changing the size (diameter \emptyset) of the pore.

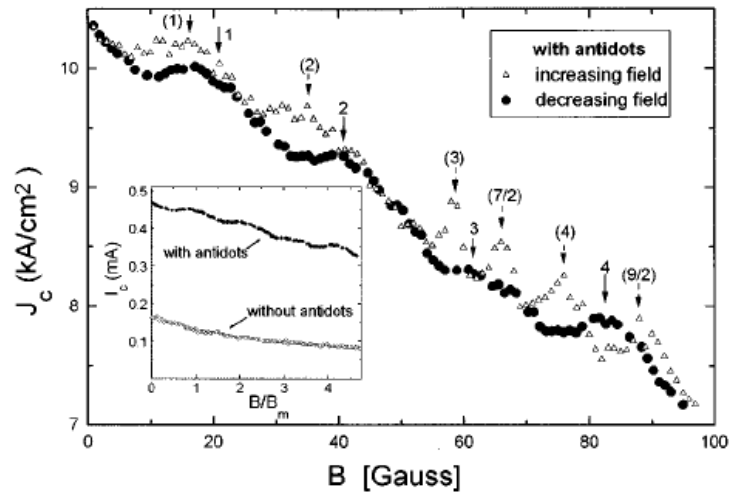


Figure 1.4: Critical current density and critical current (inset) as a function of magnetic field for YBCO films with and without antidots. The magnetic field is oriented normal to the film surface at $T = 0.95 T_c$. The matching fields are indicated by the solid and dashed arrows for decreasing and increasing magnetic field, respectively [15].

Before discussing some experiments on the pinning structures, it is worth noting that all the experiments involving superconductors with antidots have to be performed very close to T_c to avoid that the background pinning in the film reduces the influence of pinning from the antidots [33].

The composite flux-line lattices consisting of single or multiquanta vortices at the antidots and single vortices at interstitial positions have been studied by Baert et al. [7] in superconducting Pb/Ge multilayers with a square lattice of submicron holes. The authors demonstrated that the periodic arrays of antidots could be successfully used in order to stabilize such composite flux phases. They have investigated the vortices pinned at the holes and at the interstitial positions and then they have found that the mobility of the vortices at the interstices were strongly temperature dependent, which made it possible to see the transition between an *insulating* (fully localized vortices) and a *metallic* (a collective delocalized state) behavior by tuning the temperature.

In order to find the optimum size for antidots, Moshchalkov et al. [16] introduced regular arrays of submicron holes in superconducting Pb/Ge multilayers and single

WGe films. Comparative measurements of critical current densities J_c and pinning forces f_p for several well-defined antidot diameters d have showed that pinning centers with a size (diameter d) considerably larger than the temperature dependent superconducting coherence length $\xi(T)$ are much more efficient than pinning centers with the diameter of the same order of $\xi(T)$ (Fig. 1.5). That is, antidots with a larger size than $\xi(T)$ can provide a larger pinning force f_p , and therefore provide a larger critical current density J_c . Moreover, it was suggested from the experiments that the antidot size realizing the optimum pinning was field dependent: smaller antidots optimize pinning in lower fields and larger antidots optimize pinning in higher fields. Crossover between different pinning regimes is controlled by the saturation number n_S that defines the largest possible number of flux lines trapped by an antidot.

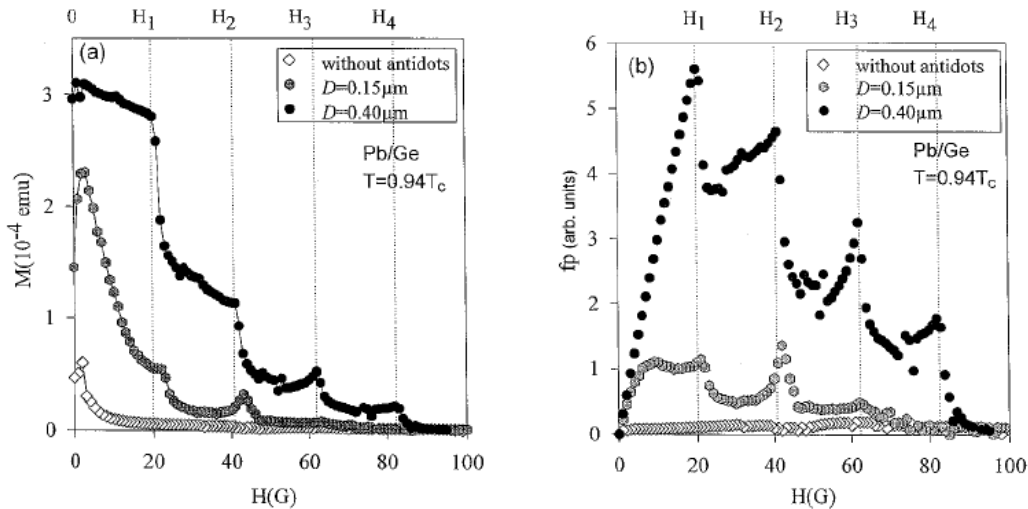


Figure 1.5: The magnetization curves and pinning forces of the antidots with different diameters. The matching fields are indicated by dashed lines [16].

Welp et al. also have demonstrated that the perforated structure of anodized aluminum foils can provide a periodic pinning potential in superconductors [34]. In this work, Nb films containing triangular array of pores with 45 nm diameter and 100 nm interpore spacing have been fabricated using anodized aluminum oxide as substrate. Pronounced matching effects in the magnetization and periodic oscillations in the superconducting

critical temperature vs field were observed. Figure 1.6 shows the phase diagram of the porous Nb film and of a reference sample. One can immediately observe that the introduction of the dense hole array provided by the alumina template strongly modifies the superconducting phase of a plain Nb thin film [10, 34]. As a result, at the matching field, the upper critical magnetic field is increased at the matching values, as a consequence of the Little-Parks effect [35].

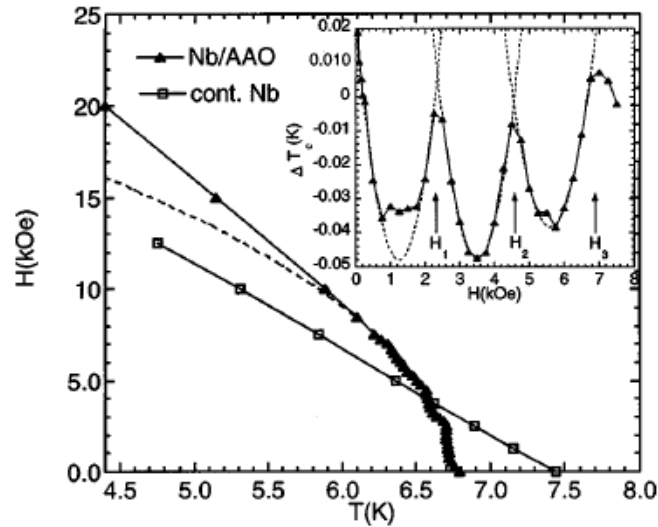


Figure 1.6: *Superconducting phase diagram of the Nb/AAO sample (solid symbols) and of a continuous reference sample (open symbols). The inset shows the oscillatory variation of $T_c(H)$ taken as the difference between the measured value and that obtained from the parabolic fit. The first three matching fields are indicated [34].*

A pronounced bump around $H = H_1$ and weak shoulder at the second matching field $H = H_2 = 2H_1$ are observed. The non linear temperature variation of H_{c2} of the perforated film is well described by a parabolic dependence as shown by dashed line in Fig. 1.6. In order to improve the visualization of the periodic anomalies, the inset shows the $R(T)$ transition width as a function of the field. Cusps in ΔT_c occurring periodically at multiples of the first matching field H_1 are observed.

In some cases, the commensurability effects can also be observed even at fractional matching fields. Baert et al. [29] have studied flux phases in superconducting Pb/Ge

multilayers with a square lattice of submicrometer holes. Sharp peaks in the magnetic field dependence of the critical current at integer and fractional matching fields have been observed. At integer fields an artificial *flux line crystal* is formed, consisting of a stable square lattice of single or multiple flux quanta trapped by the antidots. Moreover, fractional flux lines patterns at $H = H_{k/l}$ have been identified. Since the holes act as very strong pinning centers, the distribution of the fluxons is determined by the available square pattern of holes. The optimization of the vortices positions for $H < H_1$ leads to the formation of larger square flux lattices with the period $a_{k/l}$ with sites exactly falling onto the sites of the square lattice of pores with period a (Fig. 1.7).

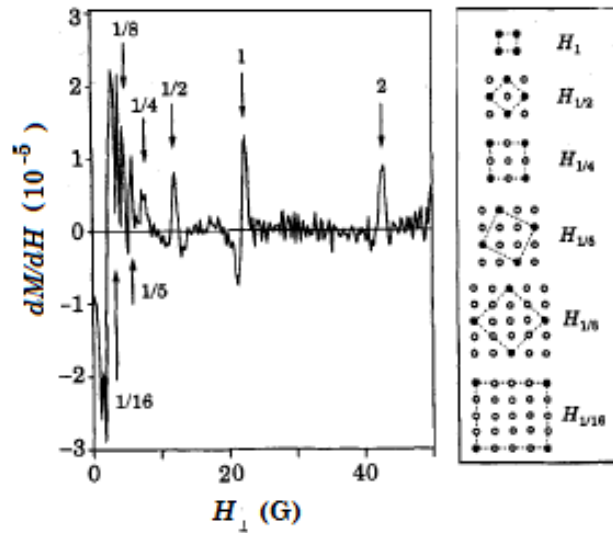


Figure 1.7: On the left side, the derivative dM/dH for a Pb/Ge multilayer with a square lattice of holes is shown. The matching fields are indicated by the arrows. On the right side, the corresponding flux patterns, for the fractional quantization, for one unit cell are shown. The filled holes represent the holes occupied by vortices [29].

Both the pinning properties of square and rectangular arrays were simulated numerically by Reichhardt et al. [36]. In both cases, the critical depinning force shows maxima only at certain integer matching fields where the vortices can form highly ordered lattices. For rectangular arrays the depinning force and the commensurability

effects are anisotropic, with a higher depinning force along the long direction, where the matching effects were considerably reduced. The authors also found that for higher fields, the matching effects were reduced and certain peaks were absent.

The anisotropy in the depinning force and the commensurability effects were experimentally realized by Van Look et al. [37]. Instead of employing rectangular pinning arrays, authors in this paper presented measurements on square arrays with rectangular shaped submicron holes, fabricated on a superconductor Pb film by an electron-beam lithography and etching. In this work two types of antidots are considered: antidots fully perforating the superconducting films and the ones that perforate the film only up to a certain depth. In both systems, they observed a distinct anisotropy in the pinning properties, reflected in the critical current J_c , which depend on the direction of the applied electrical current. Although the mechanism responsible for the effect is very different in the two systems, they both show a higher critical current when the current is applied along the long side of the rectangular antidots. In the case of rectangular antidots fully perforating the superconductor, the vortex-vortex interaction was found to be anisotropic, which was responsible for the higher critical current. On the contrary, the vortex-vortex interaction was isotropic for the case of rectangular blind antidots. Instead, the shape of the pinning sites and the fact that a vortex could move around freely within the blind antidots is the cause of the anisotropy in the critical current (Fig. 1.8).

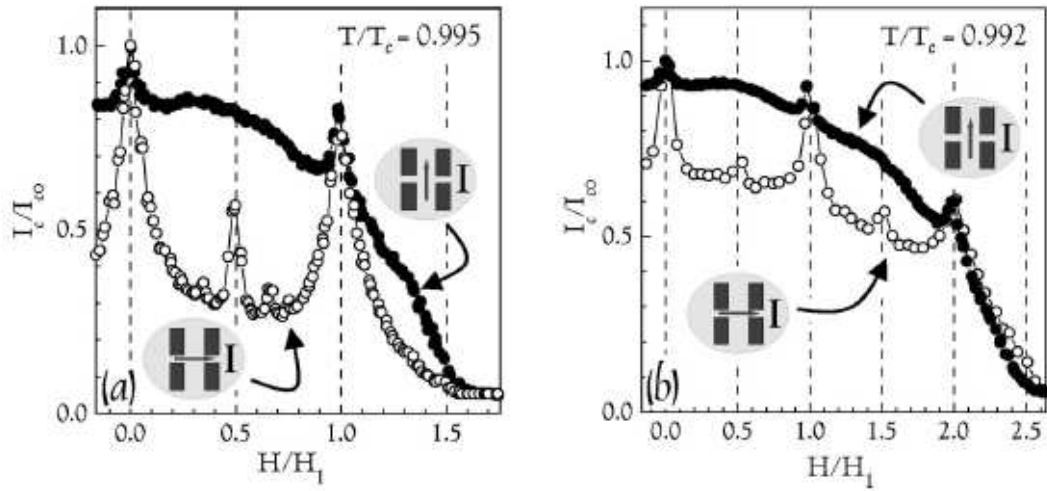


Figure 1.8: Normalized critical current I_{cx} and I_{cy} as a function of normalized magnetic field H/H_1 measured with a current in the x (open symbols) and y directions (solid symbols), respectively. Where (a) $T/T_c = 0.995$ and (b) $T/T_c = 0.992$, and H_1 is the first matching field [37].

The enhancement of the flux pinning strength at the pinning holes is widely assumed to be responsible for the critical current enhancement. However Patel et al. [38] claimed that the origin of the matching effect in such systems could be a hole-induced suppression of the critical temperature. Superconducting Nb films containing regular triangular arrays of antidots were investigated near the zero-field critical temperature. The authors found dips in the resistance vs magnetic field curves at matching fields where the magnitude of magnetic flux threading each unit cell is an integer number of the flux quantum. By comparing the magnetic field dependence of the resistance and critical temperature in perpendicular and parallel magnetic field directions, they observed that the matching effects in porous Nb films originated from hole-induced suppression of the critical temperature rather than the widely assumed flux pinning enhancement. The baseline derived is based on a wire network analysis matched to the $R(H)$ curves (Fig. 1.9). In fact, a superconducting film containing a periodic hole array should resemble a superconducting wire network [19, 39, 40] when the width w of superconducting strips forming between the pores is comparable to the superconducting coherence length ξ .

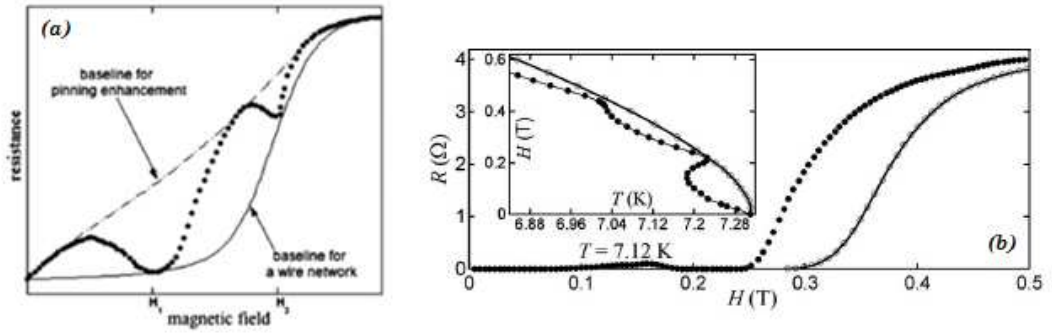


Figure 1.9: *Theory proposal and measurements in order to demonstrate the origin of anti-dots pinning enhancement. (a) A schematic approach to identify the origin of the resistance dips in $R(H)$ curves at integer matching fields. The solid circles represent typical experimental measurements. The dashed and solid curves are reference baselines expected for pinning enhancement at matching fields and hole-induced T_c suppression at non integer flux quantum fields (wire network), respectively. (b) $R(H)$ curves at $T/T_c = 0.97$ and $H(T)$ phase diagram (inset). Both curves $R(H)$ and $H(T)$ obtained in parallel fields (open circles) form the wire network baselines for those in perpendicular fields (solid circles) [38].*

In addition to the studies of square and triangular arrays, Misko et al. [41, 42] have studied the critical current J_c as a function of the applied magnetic field Φ_0 for quasi periodic pinning arrays, such as one dimensional chains and two dimensional array of pinning centers placed on the nodes of a fivefold Penrose lattice (Fig. 1.10). The enhancement of the critical current was observed in the simulation results, suggesting that the Penrose lattice of pinning sites provides huge increase in $J_c(\Phi_0)$ even compared to triangular pinning arrays. Moreover, it is worth underlining that the Penrose lattice provides a tool to control the magnitude, sharpness and position of the peaks of $J_c(\Phi_0)$.

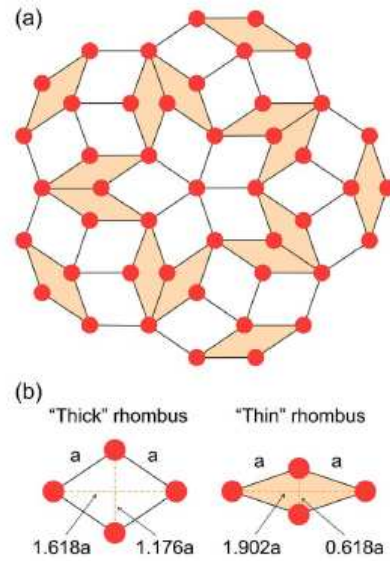


Figure 1.10: *The structure of a fivefold Penrose lattice. (a) The elemental building blocks are rhombuses with equal sides a and angles which are multiples of $\theta = 36^\circ$. (b) There are rhombuses of two kinds: those having angles 2θ and 3θ (so called thick), and rhombuses with angles θ and 4θ (so called thin) [42].*

Later, experiments for studying such fivefold Penrose pinning arrays were carried out [43–45]. A direct comparison of three different periodic arrays and quasi-periodic pinning arrays of antidots in superconducting Nb films has been investigated by Kemmler et al. [45]. In this experiment, the essential features in the $I_c(H)$ patterns as predicted by Misko et al. [41] were confirmed. A significant enhancement in $I_c(H)$ was found for quasi periodic pinning arrays in comparison to the one in samples with randomly distributed antidots or not antidots, but not as strong as triangular hole lattices (Fig. 1.11). In contrast to the plain and random samples the Penrose and triangular arrays showed clear matching effects, with identical first matching field H_1 . The triangular array showed very pronounced matching peaks at H_1 and H_2 . Instead, it is worth underlining that for Penrose lattice it was possible to have a broader distribution in the magnetic field for the critical current enhancement. Comparing absolute values of I_c for the Penrose and triangular array shows that very close to T_c critical currents at $H = 0$, H_1 and H_2 are quite similar; however, due to the stronger reduction in I_c of the triangular array between matching fields, the critical current for the Penrose array

is superior, in particular, for small fields, below H_1 . The random sample always gives significantly smaller I_c than the triangular and Penrose arrays.

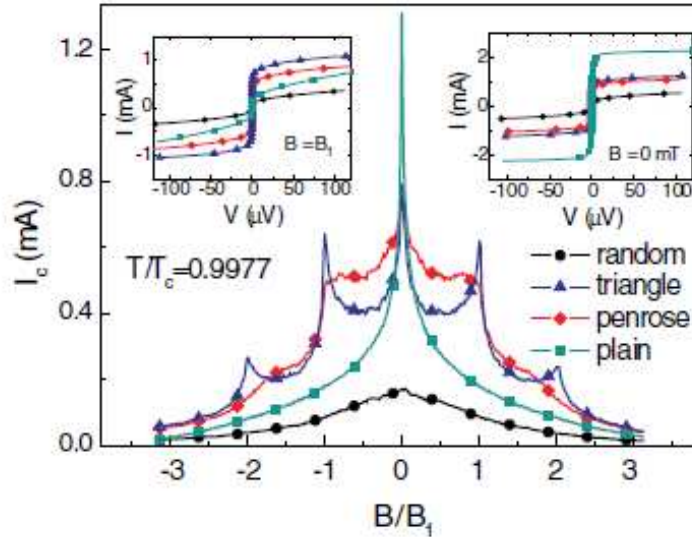


Figure 1.11: Comparison of four different antidot arrangements of the magnetic field dependence of the critical current I_c . Insets: I vs V at $H = 0$ (right) and $H = H_1$ (left) [45].

1.3.2 Magnetic dots

A different approach rather than using antidots for introducing pinning centers in the superconductors is to utilize submicron magnetic dots [8, 46, 47]. The magnetic character of the dots can induce stronger pinning effects than similar non magnetic pinning centers [22]. In addition, large enough dot magnetization may create vortices in the superconducting film. This results not only in the observation of clear pinning effects when the vortex lattice interacts with the array of the magnetic dots but also it has been observed a rich behavior of the vortex dynamics that can be tuned by modifying the properties of the pinning array [22]. The ability to tune in situ the pinning potentials via changes of the magnetic configuration presents an unique opportunity provided by magnetic pinning centers. Martin et al. [48] first reported

the study of the pinning interaction between the vortex lattice and ordered arrays of submicron magnetic dots. In their work, triangular arrays of magnetic dots have been fabricated by electron beam lithography to study pinning effects on Nb thin films. The resistivity versus magnetic field shows a set of minima at constant field intervals. Every minimum appears when there is an integer number of vortices per unit cell of the array of magnetic dots (Fig. 1.12). The nature of the pinning mechanism induced by magnetic dots was principally determined either by a magnetic interaction between the magnetic dot and the magnetic moment of the vortex, or by a local suppression of the superconductivity due to the ferromagnetic proximity around the magnetic dot. The authors also pointed out that no indication of periodic pinning has been found in arrays of non magnetic dots measured at similar temperatures, current and field ranges, suggesting that the pinning due to the ordinary proximity effect is too weak to be observed. This confirms that the effects produced by the array of the Ni dots are mainly of magnetic origin. Moreover, they argue that the pinning is more relevant in the temperature range where the coherence length, ξ , is close to the size of the pinning site.

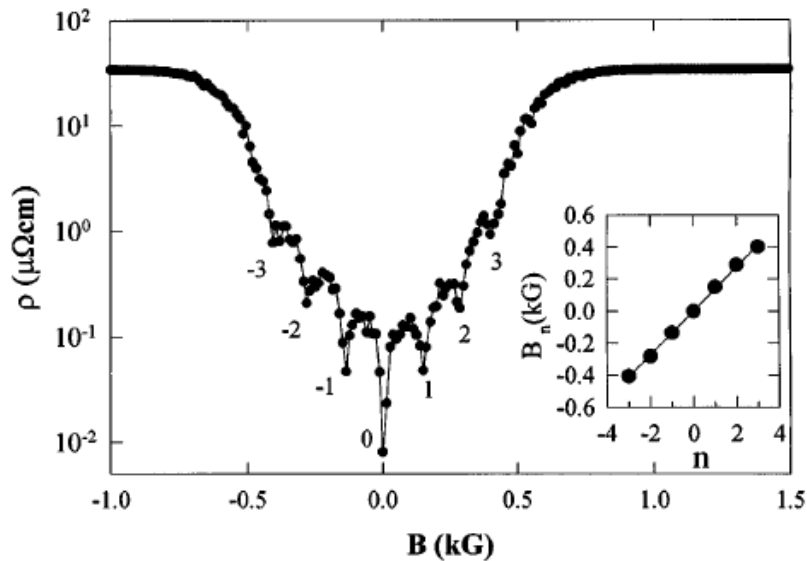


Figure 1.12: Field dependence of the resistivity of a Nb thin film with a triangular array of Ni dots. Inset shows the position of the minima versus the index number n [48].

Similar magnetic dots were studied by Van Bael et al. [20] by utilizing magnetization hysteresis loop measurements. They report on the magnetic properties of elongated submicron magnetic islands and their influence on a superconducting film. Periodic lattices of Co islands act as efficient artificial pinning arrays for the flux lines in a superconducting Pb film deposited on top of the Co islands. The influence of the magnetic state of the dots on their pinning efficiency is investigated in these films, before and after the Co dots are magnetized (Fig. 1.13).

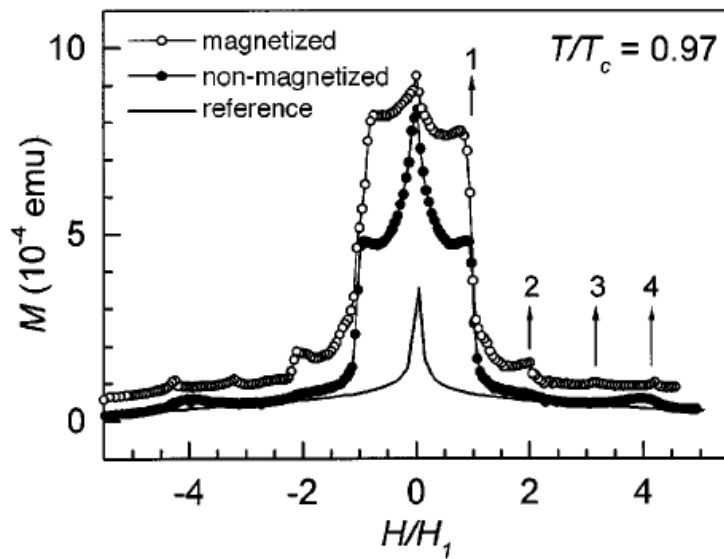


Figure 1.13: Upper half of the magnetization loop M vs H/H_1 at $T/T_c = 0.97$ for a Pb film on a triangular lattice of Co dots before (filled symbols) and after (open symbols) magnetizing the dots, and for a reference Pb film (line) [20].

The magnetization is shown as function of H/H_1 , where H_1 represents the first matching field for which the density of flux lines equals the density of dots. This implies that an one-to-one matching of the triangular vortex lattice onto the pinning array can be established at the first matching field H_1 . The presence of the lattice of Co dots results in a very strong enhancement of the width of the magnetization loop compared to the reference Pb film without dots. Moreover, pronounced anomalies are observed for T close to T_c at certain multiples of H_1 . These matching effects indicate that the lattice of Co dots creates a strong periodic pinning potential for the flux lines in the

Pb film that is deposited on top of it, similar to thin films with an antidot lattice [20].

A systematic study about the influence of size and separation of the individual magnetic pinning centers has been developed by Hoffmann et al. [19]. While there is some dependence on the dot size, the periodic pinning changes its character drastically, as soon as the separation between dots becomes comparable to the coherence length of the superconductor. In addition, the comparison between the periodic pinning of magnetic dot arrays and non magnetic dot arrays shows that the former generally present more pronounced periodic pinning. This indicates conclusively a magnetic contribution to the pinning mechanism. Figure 1.14(a) shows the magnetoresistance $\rho(H)$ for four Nb films with the same thickness covering a same square array with different Ni dot diameter. Magnetoresistance minima are observed for all samples at equidistant magnetic field intervals. For all four samples, the Ni dots were arranged on a square lattice with a lattice constant of 400 nm, thus the matching peaks occur for all samples at the same magnetic fields.

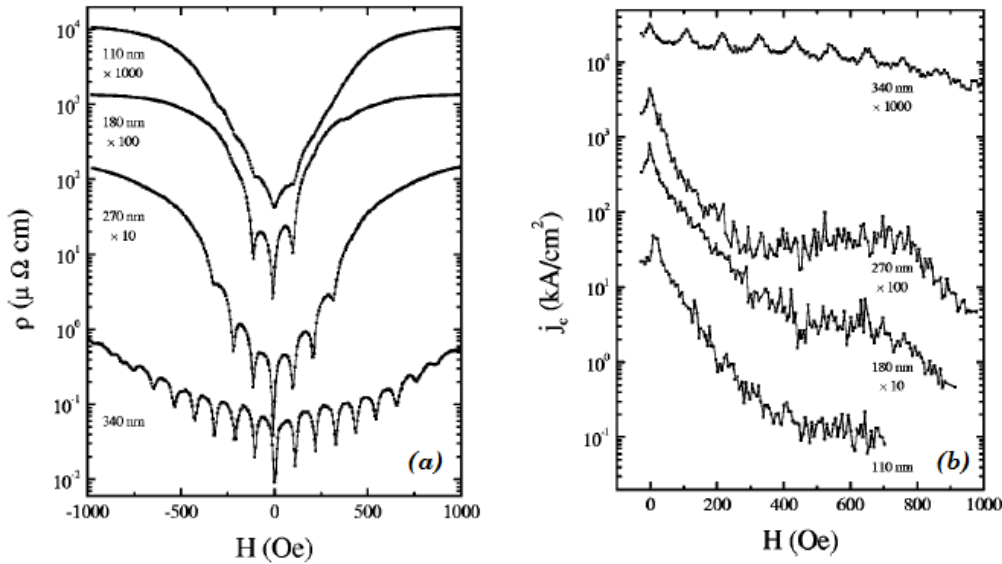


Figure 1.14: (a) The magnetoresistance $\rho(H)$ for four Nb films with different Ni dot diameter and a square array with a lattice constant of 400 nm. (b) Magnetic field dependence of the critical current density J_c for Nb films with different Ni dot diameter and a square array with a lattice constant of 400 nm [19].

It is worth underlining that the periodic pinning becomes much more pronounced for larger magnetic dots. The number and depth of matching peaks increases with increasing dot diameter. This observation is generally independent from the temperature or bias current density [19]. Moreover, the magnetic field dependence of the critical current density J_c [see Fig. 1.14(b)] shows that the behavior of the sample with the largest (340 nm) Ni dots is qualitatively different than the ones with smaller dots. Periodic critical current density matching peaks are only observed for the largest Ni dots, while the matching peaks are absent for the smaller ones. However, besides the increase in size there is also a decrease in the separation of the Ni dots, since for all the samples the lattice constant for the magnetic dot array is kept constant. Thus it is a priori not clear if the enhancement of the periodic pinning observed for the largest Ni dots is due to their size or their separation. Figure 1.15 shows the magnetoresistance for two samples with the same Nb thickness covering a same square array with a lattice constant of 600 nm and different Ni dot diameter.

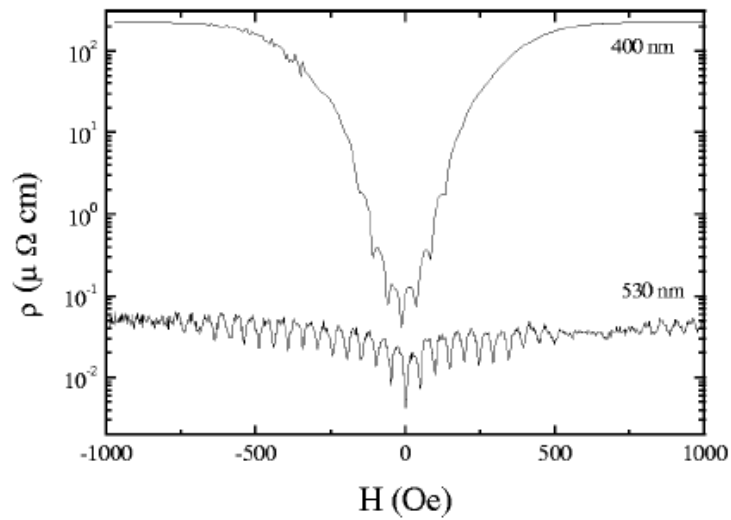


Figure 1.15: *Magnetoresistance curves for 100 nm thick Nb films with square arrays of Ni dots with dot diameter of 400 nm (top curve) and of 530 nm (bottom curve) [19].*

Clearly, the sample with bigger dots shows many more matching peaks. In addition, more importantly for the sample with 400 nm Ni dots on a 600 nm square array (see

Fig. 1.15, upper curve) the matching effects are much less pronounced than for the sample with 340 nm Ni dots on a 400 nm square array [see Fig. 1.14(a), lowest curve]. This unambiguously shows that the dot separation and not the dot size is responsible for the strong enhancement of the periodic pinning effects [19].

Another interesting work about matching effects linked to the magnetic antidots was presented by Hallet et al. [24]. Dense arrays of ordered ferromagnetic nanowires have been used to create periodic magnetic pinning centers in thin superconducting NbN films. Matching effects have been observed up to 2.5 T (11th matching field) and at low temperature. Also an appreciable enhancement of the superconducting properties has been recorded (Fig. 1.16).

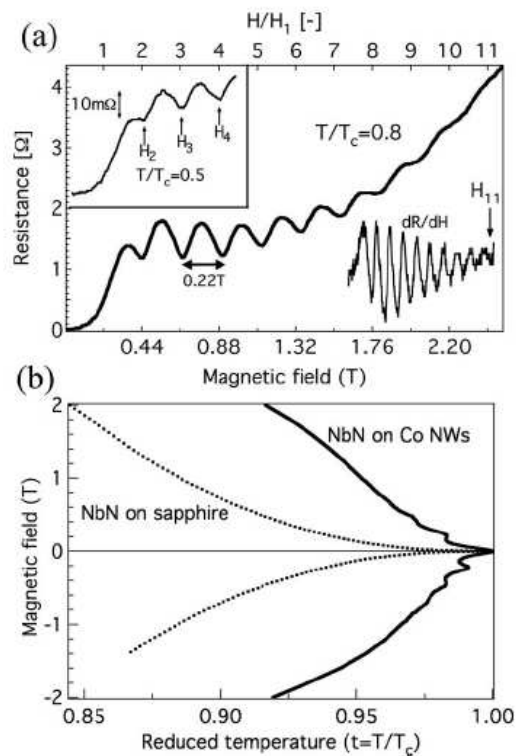


Figure 1.16: (a) *Magnetoconductance curve at $T/T_c = 0.75$ for a 25 nm thick NbN film on top of an array of 75 nm in diameter Ni nanowires. Top inset: magnetoconductance curve at $T/T_c = 0.5$. Bottom inset: derivative of the curve obtained at $T/T_c = 0.75$.* (b) *Phase diagram of a 25 nm thick NbN film deposited on top of an array of 60 nm in diameter Co nanowires (solid line) and on a flat sapphire substrate (dotted line) [24].*

Numerous oscillations, caused by matching effects are visible, showing the strong influence of the pinning center array on the vortex lattice. The oscillations are observed over the whole magnetic field range, i.e., up to 2.5 T as depicted from the derivative curve in the bottom inset. In addition, at the temperatures considered, the small spacing between the pinning centers is of the order of the superconducting coherence length ξ . As a result, the thin film behaves in fact more like an one dimensional wire network. Such networks are known to show numerous matching effects since no vortices can be placed in the interstitial sites [24]. Figure 1.16(b) compares the superconducting phase diagram for a 25 nm thick NbN film sputtered on an array of Co nanowires (solid line) with the one obtained for the same NbN film deposited on a flat sapphire substrate (dotted line). Superconductivity takes place below the corresponding curves. The critical magnetic field is strongly enhanced, which means that the sample can be used at much higher fields before vortices start to move causing dissipation [24].

Instead of employing square magnetic pinning arrays, Martin et al. [49] have performed measurements on rectangular magnetic dot arrays obtaining very interesting effects. Magnetotransport reveals the existence of two pinning regimes that correspond to two types of resistivity minima with different constant field intervals (Fig. 1.17).

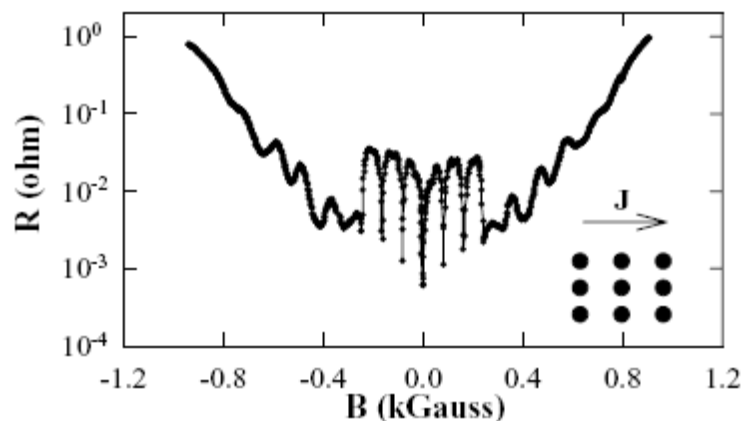


Figure 1.17: *Field dependence of the resistivity of a Nb film with a rectangular array of Ni dots ($a \times b = 400 \text{ nm} \times 625 \text{ nm}$) measured at $T/T_c = 0.98$. A sketch of the current configuration with respect to the dot array is shown [49].*

The relation with the array lattice parameters indicates that a reconfiguration in the vortex lattice from rectangular to square is induced artificially by the interaction with the dot array. Two types of minima are clearly present; narrow and deep at low fields, whereas at higher fields (above 300 G) they are broader and shallower. Two different field regimes can be clearly identified. At low fields, the minima are sharp with spacing that corresponds well with the matching field calculated for a rectangular vortex lattice with one vortex per unit cell. However, at high fields, the dissipation minima become broader and their spacing increases to a value which is close to the matching field of a square vortex lattice of parameter equal to the short side of the rectangular array. Thus, at low fields, the vortex lattice is distorted by the strong pinning potential into a rectangular configuration that matches the Ni dot rectangular array $a \times b$ cell, whereas at high fields vortex-vortex interactions become dominant and there is a reconfiguration transition in the vortex lattice, which adopts a more symmetric square configuration that is only matched along the short side of the rectangular array cell [22]. A similar reconfiguration transition from low-field rectangular vortex lattice to high-field square has been observed in Nb films grown on a Si substrate with a rectangular array of non magnetic artificial defects [50]. However, in this case, the reconfiguration field was significantly smaller than in a sample with a rectangular array of Ni dots of similar geometrical dimensions. This indicates again a reinforced pinning in the case of the magnetic dots in comparison with non magnetic defects.

Besides the reconfiguration transition, the anisotropy in the periodic pinning as a function of the direction of motion of the vortex lattice relative to the array may play an important role. Figure 1.18 shows the magnetoresistance of a Nb film on top of a $400 \text{ nm} \times 500 \text{ nm}$ rectangular array of Ni dots with the transport current along the long and short sides of the rectangular array cell (i.e. $\theta = 0^\circ$, solid symbols and $\theta = 90^\circ$, open symbols) [22]. The same matching field is found in both directions caused by the commensuration condition of one vortex per unit cell. However, a clear anisotropy appears in the background dissipation at low fields (i.e. away from the matching conditions): the resistivity is much lower for $\theta = 90^\circ$, i.e. when the vortex

lattice moves along the long side of the array cell, than for $\theta = 0^\circ$, i.e. when the vortex lattice moves along the short side of the array cell.

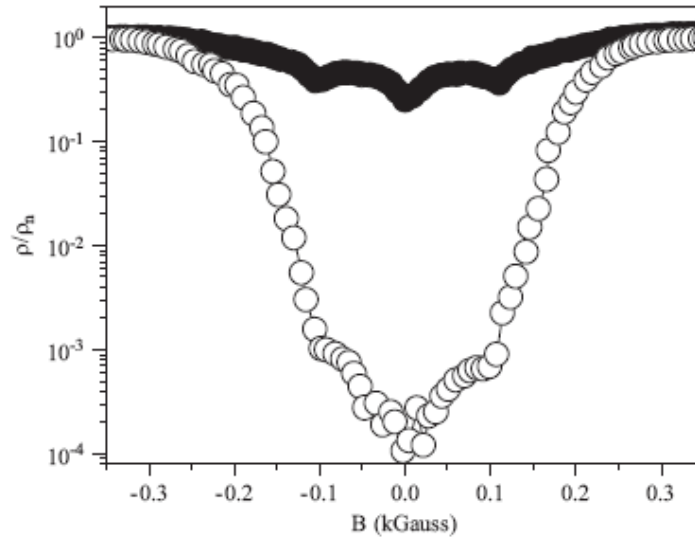


Figure 1.18: *Magnetoconductance curves for a 100 nm thick Nb film with a (400 nm × 500 nm) rectangular array of Ni dots measured at $T/T_c = 0.995$ with the transport current along the long and short sides of the rectangular array cell (i.e. $\theta = 0^\circ$, solid symbols and $\theta = 90^\circ$, open symbols) [22].*

This behavior has been predicted [36] by numerical simulations that indicate that a rectangular array of pinning centers induces an easy direction of motion for the vortex lattice along the short side of the array cell.

As I have already discussed before, the interaction between the vortex lattice and periodic arrays of pinning centers is stronger for particular, well-defined vortex densities, for which commensurability develops between the vortex lattice and the array. These matching effects appear as very sharp peaks (minima in the resistance or maxima in the critical current) as a function of the applied magnetic field. This suggests collective vortex pinning and implies a high degree of order with long vortex lattice correlation lengths. However, commensurability effects between the vortex lattice with arrays lacking periodic order (quasi periodic and random arrays) have been recently observed, implying in some cases that local order is sufficient to induce matching ef-

fects. Villegas et al. [43] have investigated vortex lattice dynamics in superconducting Nb thin films with quasi periodic arrays of magnetic pinning centers. The magnetoresistance exhibits minima for well-defined applied fields, related to matching effects between the vortex lattice and the array [Fig. 1.19(b)].

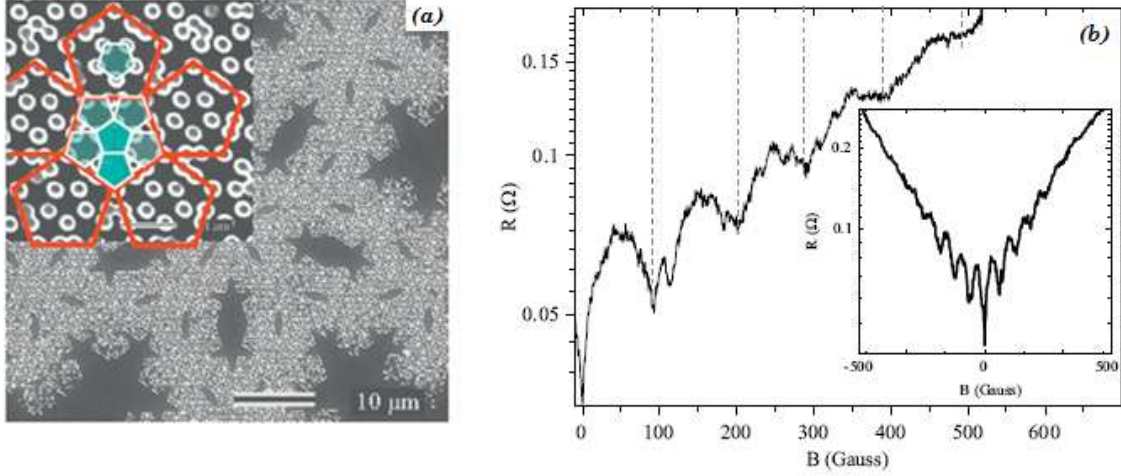


Figure 1.19: (a) Scanning electron microscopy image of a pentagonal quasi periodic array of Ni dots. The inset shows a higher magnification image where self-similar pentagons are highlighted (blue and red). (b) Magnetoresistance of a 100 nm thick Nb film on top of a pentagonal quasi periodic array of Ni dots, at $T/T_c = 0.985$. Vertical lines mark the main minima. Inset: the curve as in (b) zoomed out [43].

The quasi periodic series of minima implies that the lattice adopts the pentagonal symmetry of the array at different length scales. The long period magnetoresistance oscillations imply matching to the array geometry over the length scale of the interdot distance [smaller (blue) pentagons in Fig. 1.19(a)], while the shorter period corresponds to commensurability over longer length scales [larger (red) pentagons in Fig. 1.19(a)].

1.4 Superconductivity in one dimension

Even if the subject of one dimensional (1D) superconductivity is many decades old, it continues to be a topic of great interest and a fundamental field in the condensed matter research area. The central challenge in the study of thin superconducting wires is to understand how the superconductivity is affected when approaching 1D limit. Continual advances in fabrication techniques have allowed researchers to create wires of ever shrinking size, resulting in an increasing number of observed effects that shed light on this basic question. Earlier studies have predicted that when the wire width is smaller than its phase coherence length $\xi(T)$ intrinsic thermal [51, 52] and quantum [53–55] fluctuations play an increasingly important role in this limit, causing the wires to remain resistive much below the superconducting transition temperature T_c . Phase slip processes are responsible for resistance in superconducting nanowires. At high temperatures (but below the transition temperature T_c) this resistance is caused by thermally activated phase slips (TAPS), namely the system makes a transition across a potential barrier between two different metastable states. At sufficiently low temperatures the general expectation is that the system would tunnel through the barrier between two metastable states, constituting a quantum phase slip event (QPS). Until now there are several experimental observations of TAPS which are in agreement with the predictions of the theoretical models. But observations of QPS remain a subject of strong debate. In the following I will first discuss the physics of phase slip phenomenon and then the models of TAPS and their experimental observation. The chapter ends with a discussion of theoretical models for QPS and by outlining some experimental works that claim observation of QPS.

1.4.1 Phase slips in one dimension

Within the phenomenological model of superconductivity proposed by Ginzburg and Landau (GL) in 1950, the superconducting electrons are described by the complex order parameter

$$\psi = \psi_0 e^{i\phi} \quad (1.7)$$

where ψ_0 is the magnitude and ϕ is the phase of the order parameter. The density of the superconducting electrons is given by $n_S = |\psi|^2 = \psi_0^2$, which is non zero below the superconducting transition temperature T_c .

For a superconducting nanowire, in the absence of magnetic field, the supercurrent is driven by phase gradients, with a velocity given by

$$v_S = \frac{\hbar}{2m} \nabla \phi \quad (1.8)$$

where m is the mass of the electrons. The supercurrent through a wire of cross sectional area A can be written as

$$I_S = J_S A = n_S e v_S A = \frac{e\hbar}{2m} \psi_0^2 \nabla \phi A \quad (1.9)$$

Due to conservation of current we also have that $\psi_0^2 \nabla \phi = \text{constant}$.

The process of phase slip was first introduced by Little in 1967 [56]. This theory was developed in order to understand the mechanism of the supercurrent decay in thin wires. Little's argument is based on the assumption that the superconducting order parameter is defined locally as well as globally in a thin wire. The local amplitude of order parameter is subject to thermal fluctuations. As the order parameter reaches zero

somewhere along the 1D wire the phase changes by 2π in a process known as a phase slip. In figure 1.20 the complex order parameter $\psi = |\psi(x)|e^{i\phi(x)}$ of a thin wire ring is plotted as a function of the position x along the ring. Two possible configurations, ψ_0 (with no vortex, $n = 0$) and ψ_1 (with one vortex, $n = 1$), are shown. ψ_1 makes an excursion around zero in the Argand plane near the point A while ψ_0 does not make such an excursion. The state ψ_1 corresponds to a phase difference of 2π along the ring and leads a nonzero supercurrent.

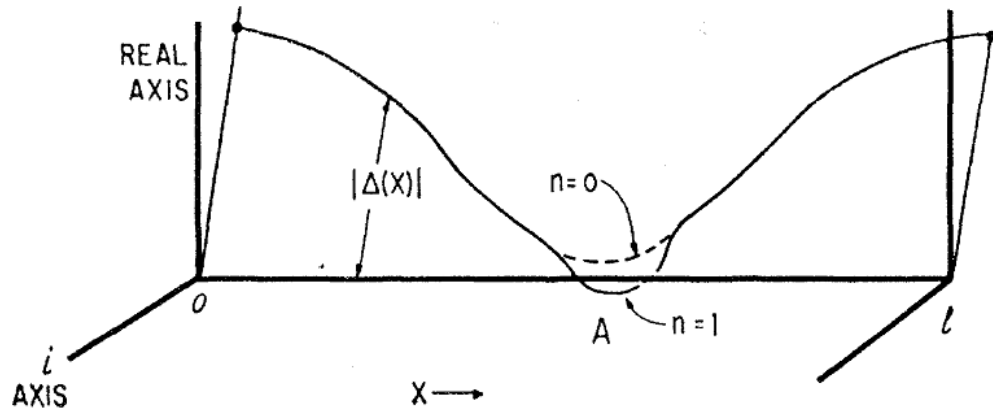


Figure 1.20: The superconducting order parameter is plotted as a function of the position along a superconducting ring. The two possible configurations shown correspond to the order parameter $\psi_0(x)$, with no vortex present in the ring ($n = 0$), and to the order parameter $\psi_1(x)$, with one vortex present in the ring ($n = 1$). Near the point A , $\psi_1(x)$ makes an excursion around zero on the Argand plane, while $\psi_0(x)$ does not. The transition from $n = 1$ to $n = 0$ constitutes a phase slip event. This event can be considered a vortex, with its normal core, passing across the wire. The transition between the $n = 1$ and $n = 0$ state can only occur if the order parameter reaches zero somewhere along the wire [56].

The state ψ_0 , on the other hand, corresponds to zero phase difference and corresponds to zero net supercurrent. The transition from ψ_1 to ψ_0 constitutes a phase slip event that topologically requires the order parameter curve to cross the x -axis. Precisely the condition $\psi = 0$ needs to be satisfied at some point in time along the wire. Hence, a phase slip event is equivalent to vortex core passing across the nanowire [57]. After each phase slip event, the phase difference between the ends of the wire can only change

by an integer multiple of 2π . The phase difference between the leads is defined by the number of times the order parameter goes around zero on the Argand plane. Little's idea about phase slippage was further developed also in other works [51, 58, 59].

Within Little's model, a finite resistance occurs at constant voltage bias, according to the following explanation. The voltage applied to the ends of the wires increases the phase difference between the wire, and thus tends to increase the supercurrent (Eq. 1.9). Simultaneously, the phase slips occurring stochastically at any point along the wire tend to decrease the supercurrent. A dynamic non-equilibrium steady state is reached at a supercurrent value that is linearly dependent on the applied voltage. This leads to a finite resistance. By the processes of phase slips the energy introduced by the voltage source is dissipated as heat rather than converted into kinetic energy of the supercurrent.

Thus, as I will discuss later, the process of phase slip leads to dissipation and the wire acquires a non-zero electrical resistance. This resistance is defined by an equation containing the temperature dependent energy barrier. This barrier is determined by the condensation energy required to locally suppress the order parameter to zero. The minimum energy barrier corresponds to fluctuations in which the order parameter is suppressed in wire segments with lengths of the order of coherence length $\xi(T)$. Hence TAPS causes nanowires to remain resistive at any nonzero temperature. In the following section the expression for the energy barrier for phase slip processes in a nanowire will be derived.

1.4.2 Free energy barrier

The calculation of the energy barrier for phase slips was done by Langer and Ambegaokar (LA) [58]. Using the time dependent GL theory, they found that the value of minimum free energy barrier that separates two stationary states of a 1D superconductor is

$$\Delta F(T) = \frac{8\sqrt{2}}{3} \frac{H_c^2(T)}{8\pi} A\xi(T) \quad (1.10)$$

where H_c is the thermodynamical critical field, A is the cross sectional area of the wire and ξ is the GL coherence length. The minimum volume over which the phase slip can occur is $\sim A\xi(T)$ and the condensation energy involved is $\sim A\xi(T)H_c^2(T)/8\pi$. Here, we have assumed that the diameter of the wire is smaller than the coherence length ξ such that entire cross section of the wire is normal during a phase slip process. Recalling that near T_c

$$H_c(T) \propto \left(1 - \frac{T}{T_c}\right) \quad (1.11)$$

and

$$\xi(T) \propto \left(1 - \frac{T}{T_c}\right)^{-1/2} \quad (1.12)$$

Eq. 1.10 leads to temperature dependence of the barrier as

$$\Delta F(T) = \Delta F(0) \left(1 - \frac{T}{T_c}\right)^{3/2} \quad (1.13)$$

Now we would like to find an expression for energy barrier comparable with the experimental data; to do this we begin with $\Delta F(0)$ as

$$\Delta F(0) = \frac{8\sqrt{2}}{3} \frac{H_c^2(0)}{8\pi} A\xi(0) \quad (1.14)$$

Recognizing now that GL coherence length is defined by

$$\xi^2(T) = \frac{\hbar^2}{4m|\alpha(T)|} \quad (1.15)$$

where

$$\alpha(T) = -\frac{2e^2}{mc^2} H_c^2(T) \lambda_{eff}^2(T) \quad (1.16)$$

with λ_{eff} the effective penetration depth and c the speed of light. At zero temperature we have

$$\xi^2(0) = \frac{\hbar^2 c^2}{8e^2 H_c^2(0) \lambda_{eff}^2(0)} \quad (1.17)$$

Thus, using this expression to eliminate $H_c(0)$ from Eq. 1.14, we get

$$\Delta F(0) = \frac{8\sqrt{2}}{3} \frac{1}{8\pi} \frac{\hbar^2 c^2}{8e^2 \xi^2(0) \lambda_{eff}^2(0)} A \xi(0) \quad (1.18)$$

Recalling that, in the dirty limit

$$\frac{1}{\lambda_{eff}^2(0)} = \frac{l}{\lambda_L^2(0) \xi_0} \quad (1.19)$$

where ξ_0 is the Pippard coherence length, λ_L the London penetration depth and l the mean free path, $\Delta F(0)$ becomes

$$\Delta F(0) = \frac{\sqrt{2}}{3} \frac{A}{8\pi} \frac{\hbar^2 c^2}{e^2 \xi(0) \lambda_L^2(0)} \frac{l}{\xi_0} \quad (1.20)$$

At this point, we will eliminate the London penetration depth, given by

$$\frac{1}{\lambda_L^2(0)} = \frac{4\pi n_S(0)e^2}{mc^2} = \frac{4\pi ne^2}{mc^2} \quad (1.21)$$

where n is the density of the normal electrons. At zero temperature, almost all the electrons are paired and the density of superconducting electrons is equal to the total density of electrons $n_S(0) = n$. The free energy barrier now becomes

$$\Delta F(0) = \frac{\sqrt{2}}{3} \frac{A}{2} \frac{\hbar^2}{e^2 \xi(0)} \frac{l}{\xi_0} \frac{ne^2}{m} \quad (1.22)$$

From the microscopic BCS theory

$$\xi_0 = \frac{\hbar v_F}{\pi \Delta(0)} \quad (1.23)$$

where v_F is the Fermi velocity and $\Delta(0)$ is the superconducting gap at zero temperature, so

$$\Delta F(0) = \frac{\sqrt{2}}{3} \frac{\pi \hbar}{2e^2} \frac{A}{\xi(0)} \frac{ne^2 l}{mv_F} \Delta(0) \quad (1.24)$$

From Drude model of metals follows that the resistivity of a wire can be written as

$$\frac{1}{\rho} = \frac{ne^2 l}{mv_F} \quad (1.25)$$

and using this expression in Eq. 1.24 we arrive at

$$\Delta F(0) = \frac{\sqrt{2}}{3} \frac{\pi \hbar}{2e^2} \frac{A}{\xi(0)} \frac{1}{\rho} \Delta(0) \quad (1.26)$$

The BCS gap at zero temperature is given by $\Delta(0) \cong 1.76k_B T_c$. Thus, we get

$$\Delta F(0) = 0.83 \frac{R_Q}{R_N} \frac{L}{\xi(0)} k_B T_c \quad (1.27)$$

where $R_Q = \pi\hbar/2e^2 = h/4e^2$ is the quantum resistance of Cooper pairs and $R_N = \rho L/A$ is the normal state resistance of the wire with length L . As a final simplification, we define a parameter c which allows us to express the free energy barrier as a function of temperature given as

$$\Delta F(T) = \Delta F(0) \left(1 - \frac{T}{T_c}\right)^{3/2} = c k_B T_c \left(1 - \frac{T}{T_c}\right)^{3/2} \quad (1.28)$$

where

$$c = 0.83 \frac{R_Q}{R_N} \frac{L}{\xi(0)} \quad (1.29)$$

1.4.3 Appearance of resistance in 1D superconducting wire

Superconducting nanowires never show zero resistance, although resistance does decrease exponentially upon cooling [51, 56, 58, 60–62] (see Fig. 1.21). The origin of this resistive behavior lies in the occurrence of thermally activated slips of the phase of the GL order parameter. During a phase slip, a small normal segment appears on the nanowire for a short time causing the loss of phase coherence [63]. Typical dimensions of such fluctuations are of the order of the superconducting coherence length. Generally, since the wire diameter is assumed smaller than the coherence length, it is clear that each such fluctuation should disrupt the flow of supercurrent and thereby impart a non zero resistance to the wire [64]. Such fluctuations are more commonly called thermally activated phase slips (TAPS) because the fluctuations

thermally activate the system over the free energy barrier, which changes the phase by 2π , thus providing the phase slip.

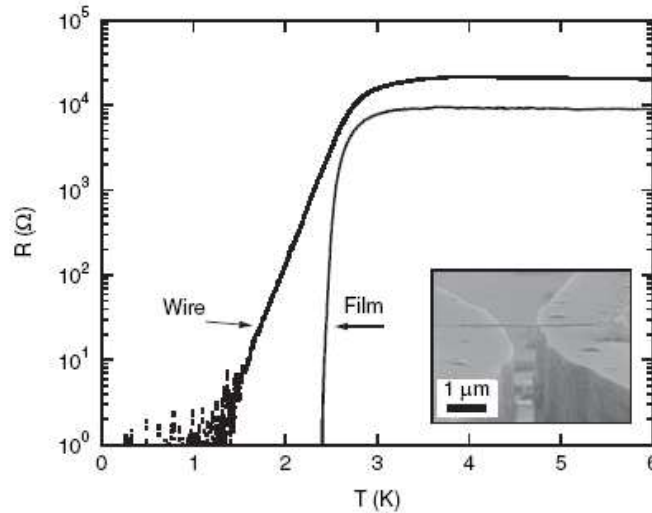


Figure 1.21: *Resistance vs temperature curve of a nanowire of amorphous indium oxide, together data obtained from a similarly prepared wide film. The transition is broad significantly more than one in similar 2D film, signaling the approach to the 1D limit. Inset: A scanning electron micrograph of a typical device [62].*

In order to derive the resistance from TAPS we must first include the effect of the bias current in the wire. This makes the free energy landscape tilted, compared to the zero bias case (see Fig. 1.22).

Due to thermal fluctuations, the phase jumps over the barrier constituting a phase slip event. Because of the tilt the phase slip in one direction is more favorable than in the other as the energy barrier is lowered in one direction and increased in the other. The amount by which the free energy is lowered or raised was given by Anderson and Dayem [65] and it can be written as

$$\delta F = \frac{hI}{2e} \quad (1.30)$$

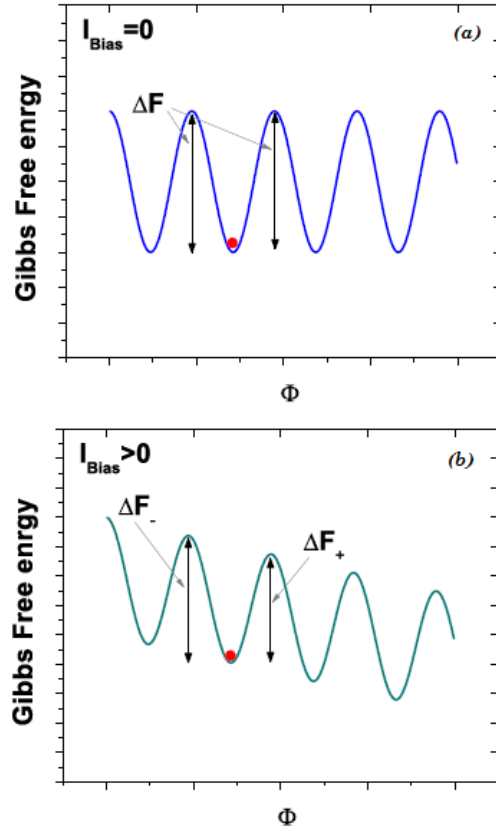


Figure 1.22: Free energy diagram. (a) When no bias current is applied, the energy barriers for positive phase slips (change the phase by 2π) and negative phase slips (change the phase by -2π) are the same. (b) With a bias current the free energy barrier for a positive state is smaller than the one for a negative phase slip. Hence the rate of the positive phase slips exceeds the one for negative phase slips, resulting in a measurable resistance.

If the system wants to go over the barrier with a frequency Ω , it will be successfully excited with a probability set by the Boltzmann factor $\exp(-\Delta F/k_B T)$. The phase of the system will then be lost at a rate

$$\begin{aligned} \frac{d\phi}{dt} &= \Omega \left[\exp\left(\frac{-\Delta F + \delta F/2}{k_B T}\right) - \exp\left(\frac{-\Delta F - \delta F/2}{k_B T}\right) \right] = \\ &= 2\Omega e^{-\Delta F/k_B T} \sinh\left(\frac{\hbar I}{4ek_B T}\right) \end{aligned} \quad (1.31)$$

Now, the resistance can be derived from this by using the Josephson relation:

$$\frac{d\phi}{dt} = \frac{2eV}{\hbar} \implies V = \frac{\hbar\Omega}{e} e^{-\Delta F/k_B T} \sinh\left(\frac{hI}{4ek_B T}\right) \quad (1.32)$$

Differentiating the expression for the voltage we get

$$\frac{dV}{dI} = \frac{h}{4e^2} \frac{\hbar\Omega}{k_B T} e^{-\Delta F/k_B T} \cosh\left(\frac{hI}{4ek_B T}\right) \quad (1.33)$$

The frequency Ω is a prefactor that gives how often a phase slip is attempted and it will be discussed in more detail shortly. Using Ohm's law and recalling that the hyperbolic cosine is equal to one when $I \ll 4ek_B T/h$, the resistance of a superconducting wire can be written as

$$R_{LAMBH} = R_Q \frac{\hbar\Omega}{k_B T} e^{-\Delta F/k_B T} \quad (1.34)$$

where $R_Q = h/4e^2$ is the quantum resistance for Cooper pairs. Here the resistance is denoted R_{LAMBH} from Langer, Ambegaokar, McCumber and Halperin [51, 58].

The value of the prefactor was derived by McCumber and Halperin [51] using time dependent GL theory. They found the expression for the temperature dependent attempt frequency

$$\Omega = \frac{L}{\xi(0)} \left(\frac{\Delta F}{k_B T}\right)^{1/2} \frac{1}{\tau_{GL}} \quad (1.35)$$

where $1/\tau_{GL} = 8k_B(T_c - T)/\pi\hbar$ is the GL relaxation time which characterizes the relaxation rate of the superconductor in the time dependent GL theory. The full dependence of the LAMBH resistance can now be written as

$$R_{LAMH}(T) = A \left[\left(1 - \frac{T}{T_c} \right)^{3/2} \frac{T_c}{T} \right]^{3/2} \exp \left[-c \left(1 - \frac{T}{T_c} \right)^{3/2} \frac{T_c}{T} \right] \quad (1.36)$$

where

$$A = R_Q \frac{8}{\pi} \frac{L}{\xi(0)} \left(0.83 \frac{L}{\xi(0)} \frac{R_Q}{R_N} \right)^{1/2} \quad \text{and} \quad c = 0.83 \frac{L}{\xi(0)} \frac{R_Q}{R_N} \quad (1.37)$$

Early experiments in 1970s by Lukens et al. [60] and Newbower et al. [61] in separate measurements of single crystal tin whiskers with diameters $\sim 0.5 \mu\text{m}$ confirmed LAMH theory (Fig. 1.23).

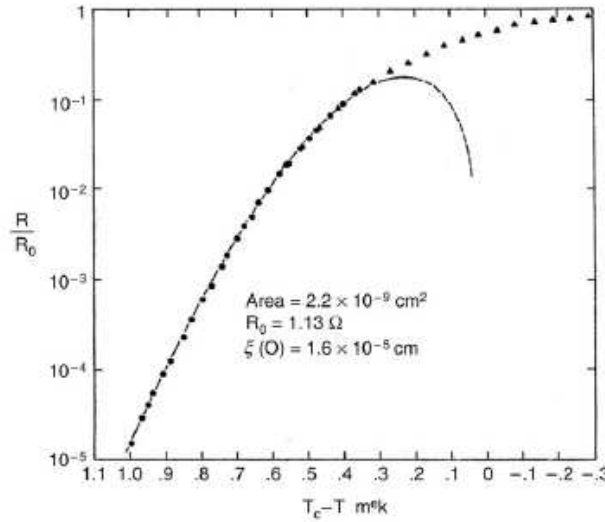


Figure 1.23: Data (symbols) from Lukens, Warburton, and Webb [60] and their fit to LAMH theory (dashed line).

They found that the resistance of the wire is well described by the LAMH theory. However, both the reports show some deviation from the theory as $T \rightarrow T_c$ but this is to be expected as the theory is only valid when $\Delta F \gg k_B T$ while as $T \rightarrow T_c$, $\Delta F \rightarrow 0$. Also the agreement between the LAMH theory and the data of Newbower et al. is good, but they further found that they could improve their fits by including a parallel normal channel such that

$$R^{-1}(T) = R_{LAMH}^{-1}(T) + R_N^{-1}(T) \quad (1.38)$$

However, it has been established by several experiments on ultra thin nanowires that LAMH fit explains the resistive transitions in homogeneous nanowires. The analysis of LAMH model was also done with the data obtained from measurements on bridges (of width w) seamlessly connecting two coplanar superconducting films [66]. The shape of the measured $R(T)$ curve is in perfect agreement with the overall shape of the curve computed using the standard LAMH theory (see Fig. 1.24). This agreement is observed over a range of 11 orders of magnitude of the resistance. The only disagreement found by the authors with LAMH model is that the pre-exponential factor had to be modified in order to obtain a reasonably low critical temperature of the bridge. The critical temperature is used as an adjustable parameter in the fitting procedure.

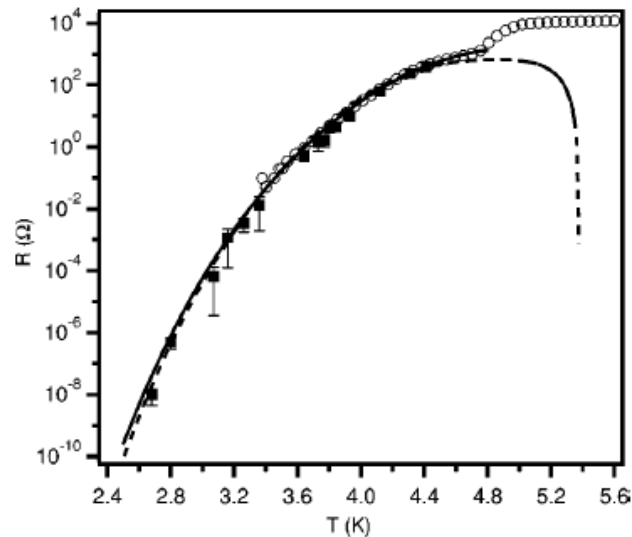


Figure 1.24: *Resistance vs temperature curve. Open circles represent data that have been directly measured while the dashed curve gives the best fit generated by LAMH formula [66].*

This behavior is in agreement with the prediction [58] that superconducting channels of width $w \sim \xi(T)$ should exhibit a 1D behavior, i.e., nucleation of vortices is unfavorable

in such channels. Such condition is true for this sample [66].

Rogachev et al. [52] have shown that in the absence as well as in the presence of magnetic field the resistance of a MoGe nanowire follows the predictions of the LAMH model. The data and the fit to the LAMH theory are shown in Fig. 1.25.

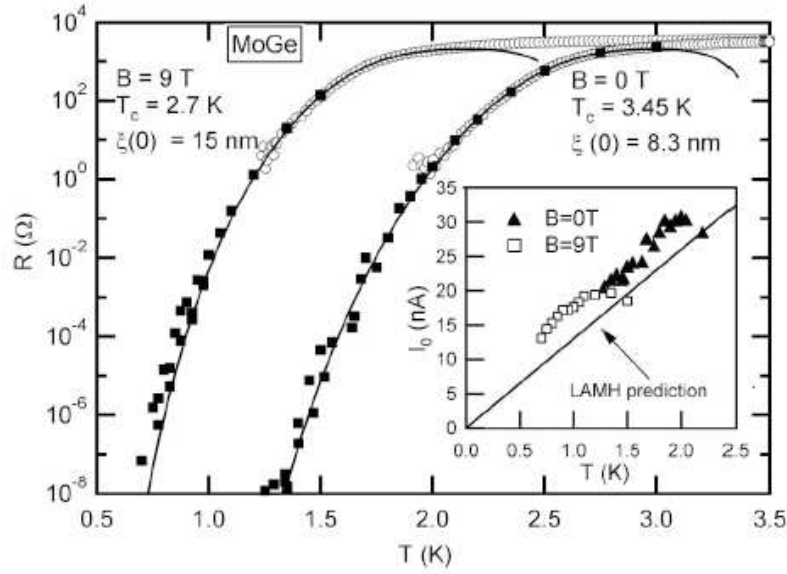


Figure 1.25: Resistance versus temperature for the MoGe nanowire at zero magnetic field and at 9 Tesla. Open circles represent zero bias current measurements and black squares indicate the resistance values obtained from the fit of the non linear portion of dV/dI curves. Solid lines are the fits to the LAMH theory. Extracted fitting parameters T_c and $\xi(0)$ are indicated. The inset shows the experimental dependence of the parameter I_0 on temperature (solid and open symbols) and the theoretical value $I_0 = 4ek_B T/h$ (solid line) [52].

The LAMH fit gives an excellent description of all resistance data in a range of 11 orders of magnitude. The authors also find good agreement with the LAMH model for data taken in magnetic field $\mu_0 H = 9$ Tesla. It is therefore concluded that the resistance in studied nanowires is determined by thermally activated phase slips even in high magnetic fields [52].

Rogachev and Bezryadin [67] have shown that thin continuous Nb nanowires, 7-15 nm in diameter, present resistive transitions that are well described by the LAMH model of thermally activated phase slip. Moreover, TEM measurements have revealed

that these wires are polycrystalline, having grain sizes of about 5 nm. The data and the fits are shown in Fig. 1.26. The authors use two fitting parameters: the superconducting coherence length $\xi(T)$ and the critical temperature T_c . The $R(T)$ data follow the LAMH theory very well.

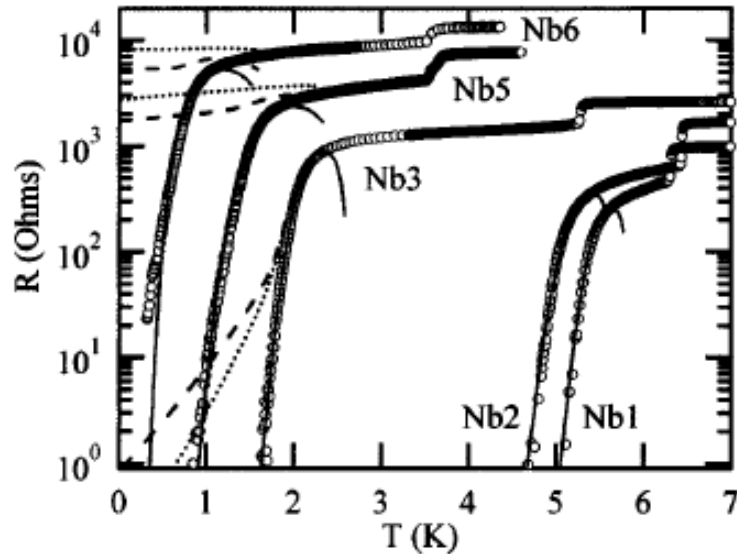


Figure 1.26: *Temperature dependence of the resistance of superconducting Nb nanowires. Solid lines show the fits to the LAMH theory. The dashed lines are theoretical curves that include the contribution of quantum phase slips into the wire resistance [68], with generic factors [67].*

In all these measurements presented on nanowires there is no evidence of quantum phase slips (QPS) in the resistance vs temperature data. In these cases the entire wire transition can be explained by LAMH fit that incorporates only TAPS. However, deviations from LAMH model have been found in many experiments [53, 68–70]. A contribution due to macroscopic quantum tunneling of phase slips was then introduced to explain the characteristic low temperature resistance tails observed in some cases.

1.4.4 Quantum phase slips

At sufficiently low temperatures, it is expected that quantum tunneling would dominate over thermally activated phase slips in nanowires. In other words, at sufficiently low temperatures quantum fluctuations of the order parameter would lead to phase slips, i.e., quantum phase slips (QPS). Observations of QPS were first reported by Giordano [53] in late 1980's. The experiments were done on In wires with a diameter of about 50 nm. It was found that close to T_c the results agreed well with the TAPS model where the phase slips occur when the phase passes over the free energy barrier. But at low temperatures the model failed qualitatively to explain the weak temperature dependent resistance *tails* (see Fig. 1.27). These resistance tails were attributed to the macroscopic quantum tunneling (MQT) of the phase in which the state of the system is not thermally activated over the free energy barrier but rather tunnels through the barrier [71]. In another study by Giordano et al. [72], the superconducting state of PbIn wires was studied. The samples which had the smallest diameters showed significant dissipation below T_c .

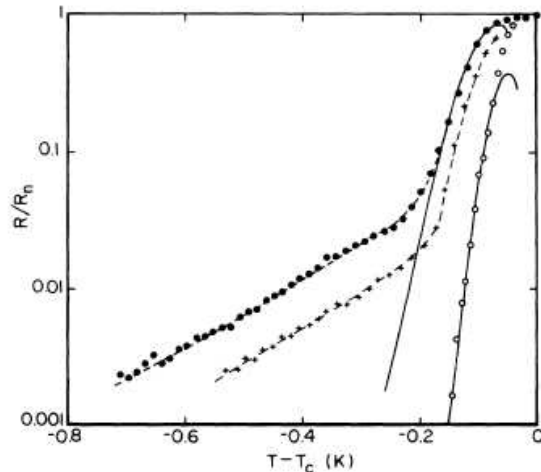


Figure 1.27: Resistance normalized by the normal state resistance as a function of temperature for three In wires. The sample diameters were 40 nm (dot symbol), 50 nm (cross symbol) and 72 nm (open symbol). The solid lines are fits according to the LAMH model and dashed lines are fits to a QPS theory [72].

At that time, no quantitative theory for MQT in wires existed for comparison with Giordano's data. So he derived an expression for the MQT rate in a wire in analogy with the well known theory of MQT in other systems, such as Josephson junctions [73]. Giordano proposed a heuristic argument that the resistance from MQT follows a form similar to that of LAMH model, except that the appropriate energy scale is \hbar/τ_{GL} instead of $k_B T$ [72]. Hence the expression for the resistance due to QPS is given by

$$R_{QPS} = B \frac{\pi \hbar^2 \Omega_{QPS}}{2e^2 (\hbar/\tau_{GL})} e^{-a \Delta F / (\hbar/\tau_{GL})} \quad (1.39)$$

where

$$\Omega_{QPS} = \frac{L}{\xi(T)} \sqrt{\frac{\Delta F}{\hbar/\tau_{GL}}} \frac{1}{\tau_{GL}} \quad (1.40)$$

and a and B are possible numerical factors of the order of unity. The factor $L/\xi(T)$ must be inserted to account for the number of independent positions at which MQT could occur (because of the existence of discrete energy levels). Due to QPS it is expected that sufficiently narrow wires would have non zero resistance even if $T \rightarrow 0$. If we consider only TAPS we would expect the resistance to approach zero as $T \rightarrow 0$, since the thermal fluctuations scale with the temperature. The total resistance of the superconducting channel at any temperature is given by the the sum of the resistances due to thermal and quantum fluctuations, i.e., $R = R_{LAMH} + R_{QPS}$. Unless R is small compared to R_N , the resistance measured will be significantly reduced because of the current carried by the parallel normal channel. Lau et al. [68] proposed taking this effect into account to predict the total resistance as

$$R = [R_N^{-1} + (R_{LAMH} + R_{QPS})^{-1}]^{-1} \quad (1.41)$$

The authors performed measurements of a large number of amorphous MoGe wires with various widths and lengths. They found a systematic broadening of the superconducting transition with decreasing cross-sectional areas, which can be described quantitatively by a combination of thermally activated phase slips close to T_c and QPS at low temperatures. Using a simple model with only two free parameters of order of unity for the entire family of curves, they found good agreement with the data over a wide range of samples. These nanowires were formed by method of molecular templating using carbon nanotubes. In this work over 20 samples were measured and a representative set showing the resistance vs temperature data of eight different wires was presented [Fig. 1.28(a)]. The $R(T)$ curves display a broad spectrum of behaviors, including some superconducting samples with resistance as high as $40 \text{ K}\Omega$ ($\gg R_Q$). It indicates that the relevant parameter controlling the superconducting transition is not the ratio of R_Q/R_N [74], but appears to be the resistance per unit length or equivalently, the cross-sectional area.

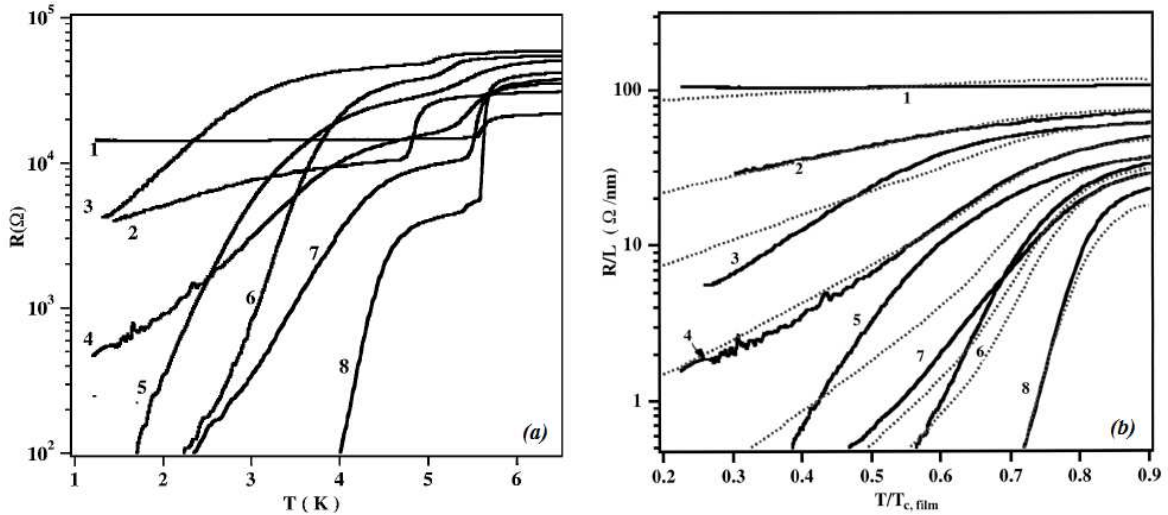


Figure 1.28: (a) Resistance as a function of temperature for eight different MoGe nanowires. (b) Resistance per unit length vs temperature normalized to T_c (solid lines) for the same eight samples as shown in (a). The dotted lines are fits using Eq. 1.41 and sample parameters. The two free parameters used are $a = 1.3$ and $B = 7.2$ for the whole family of the curves [68].

From Fig. 1.28(b) is clear that the resistances of longer wires ($R_N/L < 20\Omega/nm$) drop sharply below T_c . The transition widths broaden with increasing values of R_N/L , and resistances of the shortest wires ($R_N/L > 80\Omega/nm$) barely change with temperature down to 1.5 K. They found that the broad resistive transitions observed in the wires cannot be described by LAMH theory alone but the contribution of QPS has to be added to obtain agreement with the experimental data. To get the resistance due QPS the Eq. 1.39 was used. These fits are shown as dotted lines in Fig. 1.28(b). The most significant fact was that the entire family of curves could be fitted with only one set of values for a and B ($a = 1.3$ and $B = 7.2$). So Lau et al. [68] fitted their data including the effects of both thermally activated phase slips and macroscopic quantum tunneling of phase and obtained good agreement. Due to these facts, the authors concluded that they were indeed observing QPS effects.

Another work in which the authors state the existence of the QPS effects is the one of Tian et al. [75]. Electrical transport measurements were made on single crystal Sn nanowires to understand the intrinsic dissipation mechanisms of a 1D superconductor. Sn nanowires were fabricated by electrodepositing tin into a porous membrane. The 1D channels of the pores were found to be aligned almost parallel to each other and perpendicular to the surface of the membrane without interconnecting channels between the adjacent pores. While the resistance of wires of diameter larger than 70 nm drops precipitously to zero below T_c , a residual resistive tail extending down to low temperature was found for wires with diameters of 20 and 40 nm (Fig. 1.29). Specifically, when the logarithm of the resistance is plotted versus temperature, two distinct linear sections are found. A high temperature linear section is found immediately below T_c . Another linear section extends from just a few tenths below T_c down to the lowest temperature of measurement at 470 mK. The residual resistance is found to be ohmic at all temperatures below T_c .

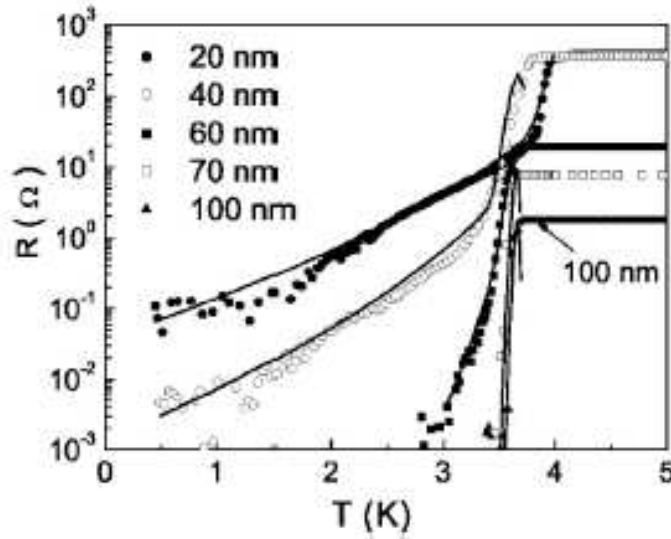


Figure 1.29: Resistance vs temperature in low temperature range for Sn nanowire arrays. The solid lines for 20, 40 and 60 nm wire diameters are the calculation results based on TAPS model near T_c and QPS model below T_c with four adjusting parameters, while those for 70 and 100 nm wires were made using only the TAPS model with two fitting parameters [75].

These findings are suggestive of a thermally activated phase slip process near T_c and quantum fluctuation induced phase slip process in the low temperature regime. The data are fitted by an equation of the form $R = R_{LAMH} + R_{QPS}$. The authors are able to fit to the data well with four free parameters over the full temperature range.

A microscopic theory of QPS in nanowires was proposed by Golubev and Zaikin (GZ) [54, 76] using the renormalization theory. Within this model if the wire is short enough so that only one phase slip event can happen at a time, we can neglect the effects of interaction of the phase slips [77]. In this limit the QPS rate is given by ($\hbar = 1$ was used in the theory)

$$\Gamma_{QPS} = \frac{S_{QPS}}{\tau_0} \frac{L}{\xi} e^{-S_{QPS}} \quad (1.42)$$

where the action S_{QPS} is given by

$$S_{QPS} = A_{GZ} \frac{R_Q}{R_N} \frac{L}{\xi} \quad (1.43)$$

with A_{GZ} being a numerical constant, $R_Q = h/4e^2$, and τ_0 is the characteristic response time of a superconducting system that roughly determines the duration of each QPS event, ξ is the superconducting coherence length [54, 76]. The effective time averaged voltage V_{eff} , due to fluctuations, can be calculated from the QPS rate using the Josephson relationship. Thus the effective resistance for 1D superconducting nanowire due to QPS is given by the expression

$$R_{QPS}(T) = \frac{V_{eff}}{I} = R_N \left(\frac{\xi}{L} \right) \tau_0 \Gamma_{QPS} = A_{GZ} R_Q \left(\frac{L}{\xi} \right) e^{-S_{QPS}} \quad (1.44)$$

Contrary to TAPS, the QPS contribution has a rather weak temperature dependence far from the critical temperature and should produce a finite resistance even at $T \rightarrow 0$ for sufficiently narrow wires [54, 76].

Zgirski et al. [78] found reasonable agreement of the data obtained from measurement Al nanowires with the GZ model. In their work, they report experimental evidence for a superconductivity in ultranarrow 1D aluminum nanowires. They found that for thicker wires the $R(T)$ dependencies were relatively narrow with quasi linear slope in logarithmic scale. These experimental data can be fitted with a reasonable accuracy within the model of thermally activated phase slips. But for thinner wires with diameters of the order of 11 nm or smaller, the transitions become wider and the data can not be fitted alone within the theory of TAPS with a reasonable set of parameters. But they got agreement with the GZ model of QPS, as shown in Fig. 1.30.

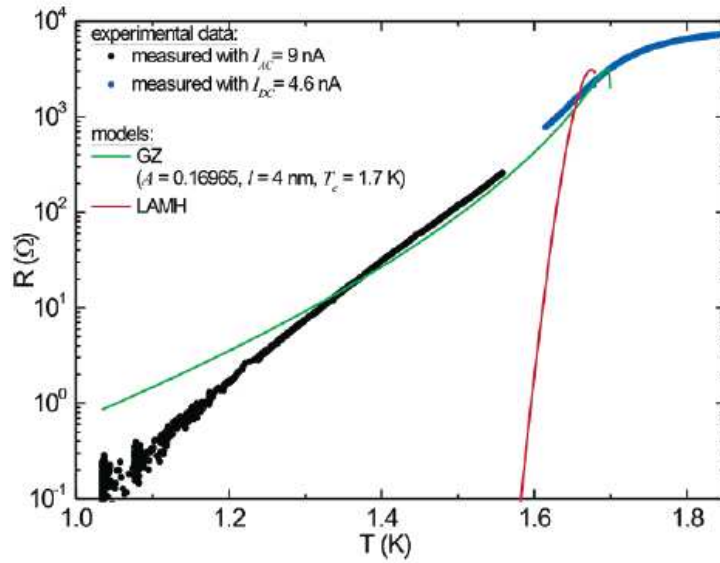


Figure 1.30: $R(T)$ dependence for the Al nanowire with diameter of 11 nm. Green line shows the result of the fit to the GZ model with A , l , and T_c being fitting parameters. The same set of parameters was used to show corresponding effect of thermally activated phase slips on the $R(T)$ transition (red line) [78].

The correspondence between the GZ model and the experimental data is rather good.

In a subsequent work, Zgirski et al. [77] showed that with the progressive reduction of the diameter of an aluminum nanowire with length $L = 10 \mu\text{m}$, the gradual broadening of the resistive transition could be explained with the GZ model (Fig. 1.31). The best fit with LAMH theory is shown for two nanowire samples. Clearly, LAMH model can not correctly explain the data. However, the fitting done using the GZ model, gives reasonable agreement.

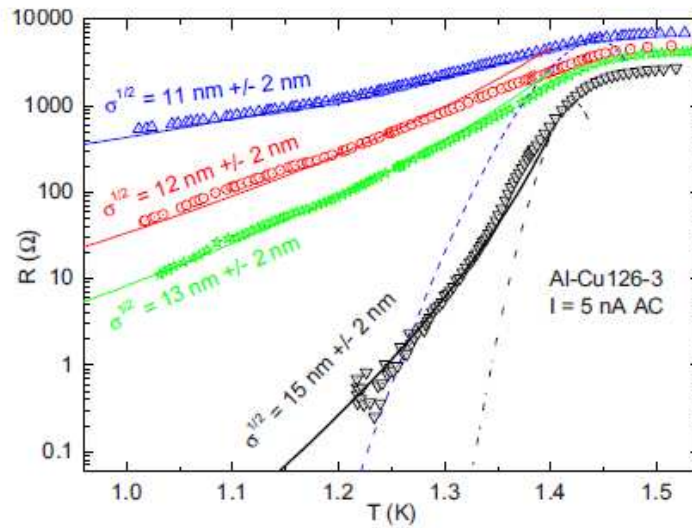


Figure 1.31: Resistance vs temperature for the thinnest samples obtained by progressive reduction of the diameter of the same aluminum nanowire Al-Cu126-3 with length $L = 10 \mu\text{m}$. The LAMH model fitting is shown with dashed lines for 11 and 15 nm samples. Fitting using the GZ model is shown with solid lines [77].

1.4.5 Other properties of 1D superconducting nanowire

Several works highlight, beyond the widening of the resistive transitions, also other features of the 1D superconducting nanowires [55, 62, 63, 79–83].

Transport properties of a superconducting NbN nanowire are studied experimentally and theoretically by Elmurodov et al. [79]. Different attached leads allowed them to measure I - V characteristics of different segments of the wire independently. The system exhibits clear hysteresis with finite jumps in I - V curves (Fig. 1.32). Each jump corresponds to phase slip lines entering the sample, which was confirmed by numerical simulations using the time dependent GL theory. Moreover, the experimental results show that extending the length of the segment the number of jumps in the I - V curves increases indicating an increasing number of phase slip phenomena. The number and size of these jumps strongly depend both on the length of the wire and the heat transfer properties of the system [79].

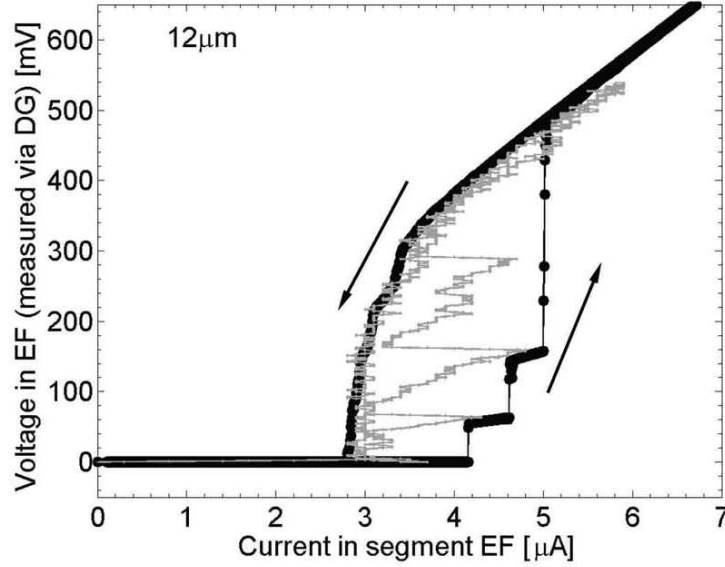


Figure 1.32: Voltage-current characteristic of a NbN nanowire $12 \mu\text{m}$ long, 70 nm wide, and 75 nm thick; under current drive (black curve) or voltage drive (grey curve) condition. Base temperature is 4.2 K and no external magnetic field is applied [79].

Applying a constant voltage to superconducting nanowires Vodolazov et al. [80] have found that the I - V characteristics exhibit an unusual S -like behavior (see Fig. 1.33). This behavior is the direct consequence of the dynamics of the superconducting condensate and of the existence of two different critical currents: J_{c2} at which the pure superconducting state becomes unstable and $J_{c1} < J_{c2}$ at which the phase slip state is realized in the system. If one starts from the superconducting state and increases the current, the superconducting state switches to the resistive superconducting or normal state at the upper critical current J_{c2} . With decreasing current it is possible to keep the sample in this state even for currents up to $J_{c1} < J_{c2}$ (which the authors call the lower critical current). The superconducting resistive state is realized as a periodic oscillation of the order parameter in time at one point of the superconductor. When the order parameter reaches zero in this point, a phase slip of 2π occurs. Such a state is now called a phase slip state and the corresponding point a phase slip center [80].

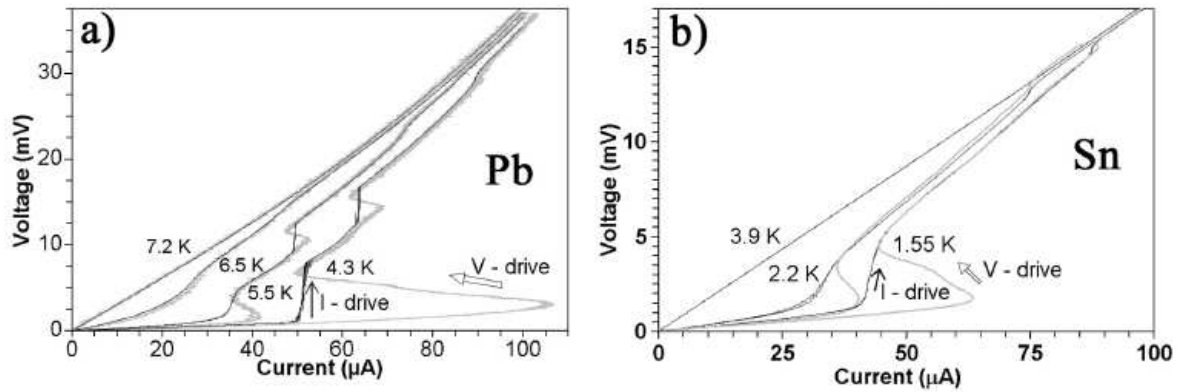


Figure 1.33: Current-voltage characteristics at different temperatures of (a) a Pb nanowire (diameter 40 nm, length 22 μm) and (b) a Sn nanowire (diameter 55 nm, length 50 μm). Results are shown for the current driven mode (black curves) and the voltage driven mode (grey curves) [80].

The meaning of the current J_{c1} is that for $J < J_{c1}$ the phase slip solution cannot be realized (in the absence of fluctuations) and thus the current J_{c1} is the critical current at which phase slip phenomena start to appear [80]. The authors state that this unusual property is typical for superconducting nanowires.

Hopkins et al. [63] used a pair of suspended DNA molecules as templates for superconducting MoGe nanowires. Because the resulting wires are very thin, comparable to the DNA molecules themselves, they are susceptible to thermal fluctuations typical for 1D superconductors and exhibit a nonzero resistance over a broad temperature range. Moreover, the authors observed resistance oscillations as a function of magnetic field in these nanowires that are different from the usual Little-Parks oscillations [see Fig. 1.34(b)]. The oscillations period is 456 μTesla , so the authors observed that this period is not controlled by the geometrical area defined by the nanowires and the edges of the leads. Instead, they found that in the low magnetic field regime (when no vortices are present in the leads), the period is controlled by Φ_0 divided by a new quantity: the product of the lead width ($2l \sim 9$ to 15 μm) and the interwire spacing ($2a \sim 0.3$ to 4 μm) [see Fig. 1.34(a)]. The authors developed a model that accurately describes the period, magnitude and temperature dependence of the observed magnetoresistance oscillations.

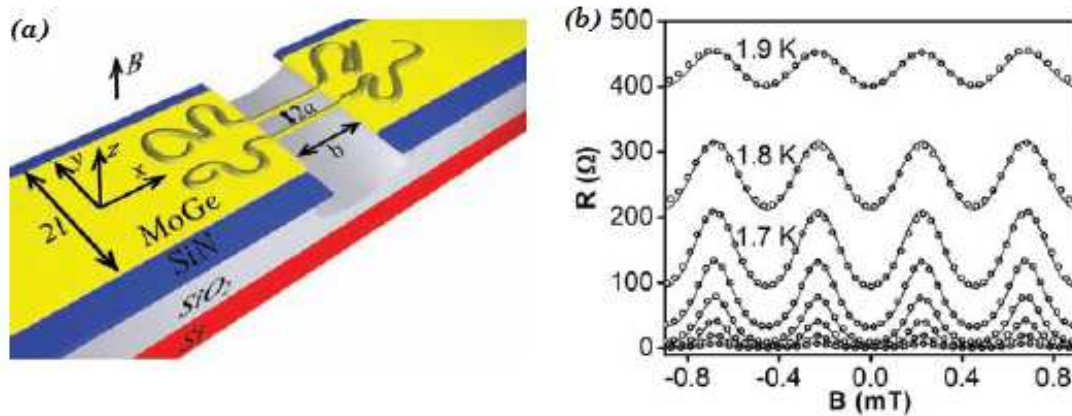


Figure 1.34: (a) Schematic of the DNA-templated two-nanowire device. Two strands of DNA are stretched across a trench etched into SiN/SiO₂ on a Si chip. The molecules and the banks are coated with superconducting MoGe. The dimensions are indicated. (b) Resistance versus magnetic field measurements at temperatures from 1.2 to 1.9 K. The lines are theoretical fits. The oscillations period is $456 \mu\text{T}$ [63].

The results from an experimental study of the magnetotransport of superconducting wires of amorphous indium oxide have been presented by Johansson et al. [62]. They found that, below the superconducting transition temperature, the wires exhibit clear, reproducible, oscillations in their resistance as a function of magnetic field (Fig. 1.35). The authors have explained these magnetoresistance oscillations as follows: one possibility is that the wires are not uniform in thickness, allowing regions near the center of the wire to remain normal while superconductivity is maintained along the edges. This may lead to an effective geometry that is similar to a mesoscopic superconducting ring, where periodic oscillations of the order parameter may appear. A related possibility is that, in a disordered superconducting wire, the vortex cores find energetically preferable locations close to the center of the wire while supercurrents can still flow unhindered near the edge rendering the central region normal and inducing an effective multiply connected geometry. Both scenarios would require the wire to be somewhat wider than the superconducting coherence length ξ to allow well separated superconducting paths to form [62]. Moreover, the authors have also observed that the amplitude of the oscillations is strongly temperature dependent and is almost fully

suppressed at $T = 1K$, while the frequency shows no temperature dependence.

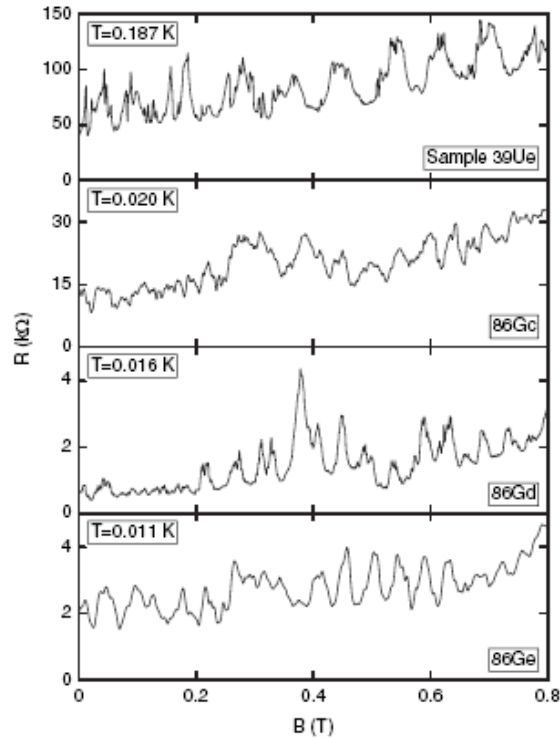


Figure 1.35: Resistance vs magnetic field data for four different nanowires, displayed in a narrow magnetic field range for clarity [62].

However, as I have already hinted at the beginning of this chapter, a superconducting film containing a hole array should resemble a superconducting wire network at temperature close to T_c .

Both these mechanisms have been used to interpret the commensurability effects observed in transport measurements on superconducting films containing an array of holes at temperatures close to T_c . For example, in aluminum films containing periodic hole arrays, Fiory et al. associated the resistance oscillations as a function of magnetic field to commensurate vortex pinning [13], whereas Pannetier et al. attributed these oscillations to wire network properties [84]. No methods exist to distinguish these two mechanisms.

At the end of the chapter, I will introduce the results of a recent research con-

ducted by Baturina et al. [85]. It is a study of transport properties of continuous and nanoporated TiN films. Applying a magnetic field to porous films, the authors observed magnetoresistance oscillations at well defined values of the applied magnetic field. In addition to the fundamental dips at $H_n = nH_1$, where n is an integer and H_1 is the first matching field, secondary dips at $H/H_1 = 1/4, 1/3, 2/5, 1/2, 3/5, 2/3$ and $3/4$ are observed (Fig. 1.36).

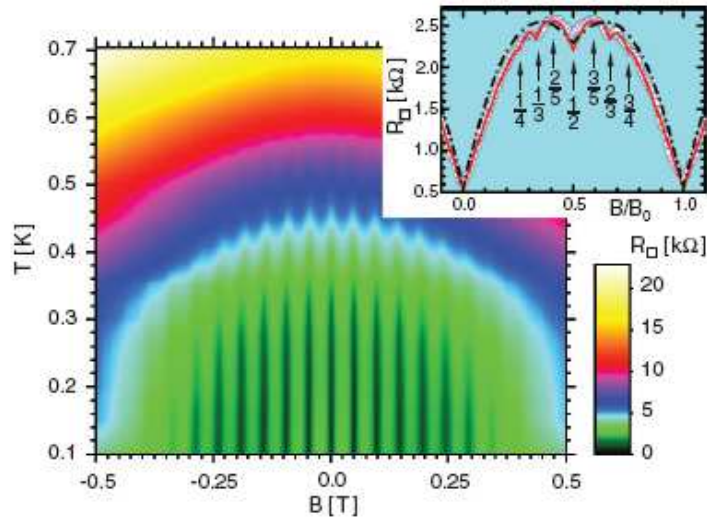


Figure 1.36: *The two-dimensional colour map of the resistance in the temperature - magnetic field plane for a nanoporated sample. The colour scale quantifying the magnitudes of the resistance is given at the lower right corner. The inset shows the experimental data of the magnetoresistance (open circles) vs reduced magnetic field H/H_1 , at temperature 0.11 K [85].*

Magnification of the resistive curve (see inset in Fig. 1.36) reveals a fine structure reflecting the collective behavior of the multiconnected superconducting film [85]. The previous observations reported a $H/H_1 = 1/2$ feature in square Josephson junction arrays [86–88], proximity-effect junction arrays [89–91], perforated films and superconducting wire networks [37, 92–94]. Instead, the full set of dips was observed in the magnetoresistance curves of square Josephson junction arrays [87, 88] and in proximity-effect junction arrays [91] and in the critical temperature variation in square superconducting wire networks [92]. A description of the observed magnetoresistance oscillations is based on the solution of the GL equation on the superconducting network

in the presence of the magnetic field [92].

The most intriguing aspect of the observed magnetoresistance oscillations is an extremely wide temperature region of their presence. The MR oscillations in the perforated films and in superconducting nanowires, were usually found close to T_c [13, 19, 37, 38, 92]. The authors also observe that as a rule the low temperature boundary for the MR oscillations to appear corresponds to the temperature at which the ratio $w/\xi(T) \leq 5$, where w is the width of the superconducting constriction and $\xi(T)$ is the superconducting coherence length. This brings to the mind the Likharev's result [95] that the weak link cannot accommodate an Abrikosov vortex if $w < w_c$ and transforms into a Josephson junction, where the critical width w_c was evaluated to be equal to $4.41 \xi(T)$.

Bibliography

- [1] H. Kamerlingh Onnes, Leiden Comm. **120b**, **122b**, **124c** (1911).
- [2] J.B. Ketterson and S.N. Song, Superconductivity, Cambridge University Press (1999).
- [3] J. Bardeen, L.N. Cooper, and J.R. Schrieffer, Phys. Rev. **108**, 1175 (1957).
- [4] L.P. Gorkov, Zh. Eksperim. i Teor. Fiz. **36**, 1918 (1959).
- [5] U. Welp, Z.L. Xiao, J.S. Jiang, V.K. Vlasko-Vlasov, S.D. Bader, and G.W. Crabtree, Phys. Rev. B **66**, 212507 (2002).
- [6] T.C. Wu, P.C. Kang, L. Horng, J.C. Wu, and T.J. Yang, J. Appl. Phys. **95**, 6696 (2004).
- [7] M. Baert, V.V. Metlushko, R. Jonckheere, V.V. Moshchalkov, and Y. Bruynseraede, Phys. Rev. Lett. **74**, 3269 (1995).
- [8] K. Harada, O. Kamimura, H. Kasai, T. Matsuda, A. Tonomura, and V.V. Moshchalkov, Science **274**, 1167 (1996).
- [9] Z. Jiang, D.A. Dikin, V. Chandrasekhar, V.V. Metlushko, and V.V. Moshchalkov, Appl. Phys. Lett. **84**, 5371 (2004).
- [10] W. Vinckx, J. Vanacken, V.V. Moshchalkov, S. Mátéfi-Tempfli, M. Mátéfi-Tempfli, S. Michotte, and L. Piraux, Eur. Phys. J. B **53**, 199 (2006).

-
- [11] A. Terentiev, D.B. Watkins, L.E. De Long, L.D. Cooley, D.J. Morgan, and J.B. Ketterson, *Phys. Rev. B* **61**, 9249 (2000).
- [12] G.S. Mkrtchyan and V.V. Shmidt, *Zh. Eksp. Teor. Fiz.* **61**, 367 (1971) (*Sov. Phys. JETP* **34**, 195 (1972)).
- [13] A.T. Fiory, A.F. Hebard, and S. Somekh, *Appl. Phys. Lett.* **32**, 73 (1978).
- [14] A.N. Lykov, *Solid State Commun.* **86**, 531 (1993).
- [15] A. Castellanos, R. Wördenweber, G. Ockenfuss, A.v.d. Hart, and K. Keck, *Appl. Phys. Lett.* **71**, 962 (1997).
- [16] V.V. Moshchalkov, M. Baert, V.V. Metlushko, E. Rosseel, M.J. van Bael, K. Temst, Y. Bruynseraede, and R. Jonckheere, *Phys. Rev. B* **57**, 3615 (1998).
- [17] U. Welp, Z.L. Xiao, V. Novosad, and V.K. Vlasko-Vlasov, *Phys. Rev. B* **71**, 14505 (2005).
- [18] J. Eisenmenger, M. Oettinger, C. Pfahler, A. Plettl, P. Walther, and P. Ziemann, *Phys. Rev. B* **75**, 144514 (2007).
- [19] A. Hoffmann, P. Prieto, and I.K. Schuller, *Phys. Rev. B* **61**, 6958 (2000).
- [20] M.J. Van Bael, K. Temst, V.V. Moshchalkov, and Y. Bruynseraede, *Phys. Rev. B* **59**, 14674 (1999).
- [21] J.I. Martín, M. Vélez, A. Hoffmann, I.K. Schuller and J.L. Vicent, *Phys. Rev. B* **62**, 9110 (2000).
- [22] M. Vélez, J.I. Martín, J.E. Villegas, A. Hoffmann, E.M. Gonzáles, J.L. Vincent and I.K. Schuller, *J. Magn. Magn. Mater.* **320**, 2547 (2008).
- [23] J.E. Villegas, E.M. Gonzáles, Z. Sefrioui, J. Santamaria, and J.L. Vincent, *Phys. Rev. B* **72**, 174512 (2005).

-
- [24] X. Hallet, M. Mátéfi-Tempfli, S. Mátéfi-Tempfli, S. Michotte, L. Piraux, J. Vanacken, and V.V. Moshchalkov, *Appl. Phys. Lett.* **95**, 252503 (2009).
- [25] M. Tinkham, D.W. Abraham, and J. Lobb, *Phys. Rev. B* **28**, 6578 (1983).
- [26] L. Horng, T.J. Yang, R. Cao, T.C. Wu, J.C. Lin, and J.C. Wu, *J. Appl. Phys.* **103**, 07C706 (2008).
- [27] X. Hallet, M. Mátéfi-Tempfli, S. Michotte, L. Piraux, J. Vanacken, V.V. Moshchalkov, and S. Mátéfi-Tempfli, *Small* **5**, 2413 (2009).
- [28] R.B. Dinner, A.P. Robinson, S.C. Wimbush, J.L. MacManus-Driscoll, and M.G. Blamire, *Supercond. Sci. Tech.* **24**, 055017 (2011).
- [29] M. Baert, V.V. Metlushko, R. Jonckheere, V.V. Moshchalkov, and Y. Bruynseraede, *Europhys. Lett.* **29**(2), 157 (1995).
- [30] E. Rosseel, M. Van Bael, M. Baert, R. Jonckheere, V.V. Moshchalkov, and Y. Bruynseraede, *Phys. Rev. B* **53**, 2983 (1996).
- [31] I.B. Khalfin and B.Ya. Shapiro, *Phys. Rev. B* **47**, 11416 (1993).
- [32] A.I. Buzdin, *Physica C* **207**, 359 (1993).
- [33] B.L.T. Plourde, *IEEE Trans. Appl. Supercon.* **19**, 3698 (2009).
- [34] U. Welp, Z.L. Xiao, J.S. Jiang, V.K. Vlasko-Vlasov, S.D. Bader, and G.W. Crabtree, *Phys. Rev. B* **66**, 212507 (2002).
- [35] W.A. Little and R.D. Parks, *Phys. Rev. Lett.* **9**, 9 (1962).
- [36] C. Reichhardt, G. Zimányi, and N. Gronbech-Jensen, *Phys. Rev. B* **64**, 014501 (2001).
- [37] L. Van Look, B.Y. Zhu, R. Jonckheere, B.R. Zhao, Z.X. Zhao, and V.V. Moshchalkov, *Phys. Rev. B* **66**, 214511 (2002).

-
- [38] U. Patel, Z. Xiao, J. Hua, T. Xu, D. Rosenmann, V. Novosad, J. Pearson, U. Welp, W. Kwok, and G. Crabtree, *Phys. Rev. B* **76**, 020508 (2007).
- [39] X.S. Ling, H.J. Lezec, M.J. Higgins, J.S. Tsai, J. Fujita, H. Numata, Y. Nakamura, Y. Ochiai, Chao Tang, P.M. Chaikin, and S. Bhattacharya, *Phys. Rev. Lett.* **76**, 2989 (1996).
- [40] Y. Bruynseraede, T. Puig, E. Rosseel, M. Baert, M.J. Van Bael, K. Temst, V.V. Moshchalkov, and R. Jonckheere, *J. Low Temp. Phys.* **106**, 173 (1997).
- [41] V. Misko, S. Savelev, and F. Nori, *Phys. Rev. Lett.* **95**, 177007 (2005).
- [42] V.R. Misko, S. Savelev, and F. Nori, *Phys. Rev. B* **74**, 024522 (2006).
- [43] J.E. Villegas, M.I. Montero, C.P. Li, and I.K. Schuller, *Phys. Rev. Lett.* **97**, 027002 (2006).
- [44] R.B.G. Kramer, A.V. Silhanek, J.V. de Vondel, B. Raes, and V.V. Moshchalkov, *Phys. Rev. Lett.* **103**, 67007 (2009).
- [45] M. Kemmler, C. Gürlich, A. Sterck, H. Pöhler, M. Neuhaus, M. Siegel, R. Kleiner, and D. Koelle, *Phys. Rev. Lett.* **97**, 147003 (2006).
- [46] M.G. Blamire, R.B. Dinner, S.C. Wimbush, and J.L. MacManus-Driscoll, *Supercond. Sci. Tech.* **22**, 025017 (2009).
- [47] S.C. Wimbush, J.H. Durrell, C.F. Tsai, H. Wang, Q.X. Jia, M.G. Blamire, and J.L. MacManus-Driscoll, *Supercond. Sci. Technol.* **23**, 045019 (2010).
- [48] J.I. Martín, M. Vélez, J. Nogues, and I.K. Schuller, *Phys. Rev. Lett.* **79**, 1929 (1997).
- [49] J.I. Martín, M. Vélez, A. Hoffmann, I.K. Schuller and J.L. Vicent, *Phys. Rev. Lett.* **83**, 1022 (1999).

-
- [50] M.I. Montero, J.J. Akerman, A. Varilci, and I.K. Schuller, *Europhys. Lett.* **63**, 118 (2003).
- [51] D.E. McCumber and B.I. Halperin, *Phys. Rev. B* **1**, 1054 (1970).
- [52] A. Rogachev, A.T. Bollinger, and A. Bezryadin, *Phys. Rev. Lett.* **94**, 017004 (2005).
- [53] N. Giordano, *Phys. Rev. Lett.* **61**, 2137 (1988).
- [54] A.D. Zaikin, D.S. Golubev, A. van Otterlo, and G.T. Zimanyi, *Phys. Rev. Lett.* **78**, 1552 (1997).
- [55] M. Tian, N. Kumar, S. Xu, J. Wang, J.S. Kurtz, and M.H.W. Chan, *Phys. Rev. Lett.* **95**, 076802 (2005).
- [56] W.A. Little, *Phys. Rev.* **156**, 396 (1967).
- [57] A. Bezryadin, *J. Phys. Condens. Mat.* **20**, 43202 (2008).
- [58] J.S. Langer and V. Ambegaokar, *Phys. Rev.* **164**, 498 (1967).
- [59] W.J. Skochpol, M.B. Beasley, and M. Tinkham, *J. Low Temp. Phys.* **16**, 145 (1974).
- [60] J.E. Lukens, R.J. Warburton, and W.W. Webb, *Phys. Rev. Lett.* **25**, 1180 (1970).
- [61] R.S. Newbower, M.R. Beasley, and M. Tinkham, *Phys. Rev. B* **5**, 864 (1972).
- [62] A. Johansson, G. Sambandamurthy, D. Shahar, N. Jacobson, and R. Tenne, *Phys. Rev. Lett.* **95**, 116805 (2005).
- [63] D.S. Hopkins, D. Pekker, P.M. Goldbart, and A. Bezryadin, *Science* **308**, 1762 (2005).
- [64] A. Bezryadin, *J. Phys. Condens. Matter* **20**, 043202 (2008).
- [65] P.W. Anderson and A.H. Dayem, *Phys. Rev. Lett.* **13**, 195 (1964).

-
- [66] S.L. Chu, A.T. Bollinger, and A. Bezryadin, *Phys. Rev. B* **70**, 214506 (2004).
- [67] A. Rogachev and A. Bezryadin, *Appl. Phys. Lett.* **83**, 512 (2003).
- [68] C.N. Lau, N. Markovic, M. Bockrath, A. Bezryadin, and M. Tinkham, *Phys. Rev. Lett.* **87**, 217003 (2001).
- [69] N. Giordano, *Phys. Rev. B* **43**, 160 (1991).
- [70] F. Sharifi, A.V. Herzog, and N.C. Dynes, *Phys. Rev. Lett.* **71**, 428 (1993).
- [71] A.J. Van Run, J. Romijn, and J.E. Mooij, *Jpn. J. Appl. Phys.* **26**, 1765 (1987).
- [72] N. Giordano and E.R. Schuler, *Phys. Rev. Lett.* **63**, 2417 (1989).
- [73] J.M. Martinis, M.H. Devoret, and J. Clarke, *Phys. Rev. B* **35**, 4682 (1987).
- [74] A. Bezryadin, C.N. Lau, and M. Tinkham, *Nature* **404**, 971 (2000).
- [75] M. Tian, J. Wang, J.S. Kurtz, Y. Liu, M.H.W. Chan, T.S. Mayer, and T. Malouk, *Phys. Rev. B* **71**, 104521 (2005).
- [76] D.S. Golubev and A.D. Zaikin, *Phys. Rev. B* **64**, 014504 (2001).
- [77] M. Zgirski, K.P. Riikonen, V. Touboltsev, and K.Y. Arutyunov, *Phys. Rev. B* **77**, 054508 (2008).
- [78] M. Zgirski, K.P. Riikonen, V. Touboltsev, and K.Y. Arutyunov, *Nano Letters* **5**, 1029 (2005).
- [79] A.K. Elmurodov, F.M. Peeters, D.Y. Vodolazov, S. Michotte, S. Adam, F. de Menten de Horne, L. Piraux, D. Lucot, and D. Mailly, *Phys. Rev. B* **78**, 214519 (2008).
- [80] D.Y. Vodolazov, F.M. Peeters, L. Piraux, S. Mátéfi-Tempfli, and S. Michotte, *Phys. Rev. Lett.* **91**, 157001 (2003).

-
- [81] U. Patel, Z.L. Xiao, A. Gurevich, S. Avci, J. Hua, R. Divan, U. Welp, and W.K. Kwok, *Phys. Rev. B* **80**, 012504 (2009).
- [82] U. Patel, S. Avci, Z.L. Xiao, J. Hua, S.H. Yu, Y. Ito, R. Divan, L.E. Ocola, C. Zheng, H. Claus, J. Hiller, U. Welp, D.J. Miller, and W.K. Kwok, *Appl. Phys. Lett.* **91**, 162508 (2007).
- [83] J. Wang, X. Ma, S. Ji, Y. Qi, Y. Fu, A. Jin, L. Lu, C. Gu, X.C. Xie, M. Tian, J. Jia, and Q. Xue, *Nano Res* **2**, 671 (2009).
- [84] A. Bezryadin and B. Pannetier, *J. Low Temp. Phys.* **102**, 73 (1996).
- [85] T.I. Baturina, V.M. Vinokur, A.Y. Mironov, N.M. Chtchelkatchev, D.A. Nasilov, and A.V. Latyshev, *Europhys. Lett.* **93**, 47002 (2011).
- [86] R.A. Webb, R.F. Voss, G. Grinstein, and P.M. Horn, *Phys. Rev. Lett.* **51**, 690 (1983).
- [87] H.S.J. van der Zant, F.C. Fritschy, W.J. Elion, L.J. Geerligs, and J.E. Mooij, *Phys. Rev. Lett.* **69**, 2971 (1992).
- [88] H.S.J. van der Zant, W.J. Elion, L.J. Geerligs, and J.E. Mooij, *Phys. Rev. B* **54**, 10081 (1996).
- [89] M. Tinkham, D.W. Abraham, and C.J. Lobb, *Phys. Rev. B* **28**, 6578 (1983).
- [90] D. Kimhi, F. Leyvras, and D. Ariosa, *Phys. Rev. B* **29**, 1487 (1984).
- [91] S.P. Benz, M.S. Rzchowski, M. Tinkham, and C.J. Lobb, *Phys. Rev. B* **42**, 6165 (1990).
- [92] B. Pannetier, J. Chaussy, R. Rammal, and J.C. Villegier, *Phys. Rev. Lett.* **53**, 1845 (1984).
- [93] T.I. Baturina, D.W. Horsell, D.R. Islamov, I.V. Drebuschak, Y.A. Tsaplin, A.A. Babenko, Z.D. Kvon, A.K. Savchenko, and A.E. Plotnikov, *Physica B* **329**, 1496 (2003).

- [94] T.I. Baturina, Y.A. Tsaplin, A.E. Plotnikov, and M.R. Baklanov, *Physica B* **378**, 1058 (2006).
- [95] K.K. Likharev, *Rev. Mod. Phys.* **51**, 101 (1979).

Chapter 2

Fundamentals of porous silicon and applications

In this chapter, the porous silicon formation process is explained. This process consists of electrochemical etching of silicon wafers in solutions based on hydrofluoric acid. Firstly, the electrochemical etching process is described and the different stages of the porous silicon formation are explained. The anodization parameters that influence the final characteristics of the fabricated layers are also discussed and the porous silicon photoluminescence is briefly explained, as the discovery in the 90s of this property generated the scientific interest on this material.

2.1 History of porous silicon

Porous silicon was discovered in 1956 by Uhrhir [1] at Bell Labs in the USA while performing electropolishing experiments on silicon wafers using an electrolyte containing hydrofluoric acid (HF). He observed that the silicon surface often developed a matt black, brown or red deposit. The deposits were tentatively supposed to be a Si suboxide and for the next decade largely remained an unwanted scientific curiosity. It was Watanabe and co-workers [2, 3] who first reported the porous nature of silicon. He found that under the appropriate conditions of applied current and solution composi-

tion, the silicon did not dissolve uniformly but instead fine holes were produced, which propagated primarily in the $\langle 100 \rangle$ direction in the wafer. Therefore, porous silicon formation was obtained by electrochemical dissolution of silicon wafers in aqueous HF solutions.

A large amount of work has been directed to obtain the understanding of the fundamental characteristics of porous silicon. Much progress has been made following a work of Leigh Canham published in 1990 [4, 5], he found that highly porous material could emit very efficiently visible photoluminescence at room temperature, this phenomenon has shown to arise from quantum confinement effects. Since that time, all features of the structural, optical and electronic properties of the material have been subjected to in-depth scrutiny. During the last twenty years, the optical properties of porous silicon have involved a very intense area of research [6, 7].

Porous silicon is a very promising material due to its excellent mechanical and thermal properties, its obvious compatibility with silicon-based microelectronics [8] and its low cost. Its large surface area within a small volume, its controllable pore sizes, its convenient surface chemistry, and the ability to modulate its refractive index as a function of the pores depth [9] makes porous silicon also a suitable dielectric material for the formation of multilayers [10].

All these features also lead, on one hand, to interesting optical properties by mixing silicon with air in the effective medium approximation. On the other hand the pores allow the penetration of chemical and biological substances, liquids, cells and molecules by changing, in this way, the optical behavior of the original system. These effects inspired research into different applications like optical sensing [11] and biomedical applications [12, 13].

2.2 Basics of the porous silicon formation process

2.2.1 Electrochemical etching of porous silicon

One of the most important advantages of porous silicon is its simple and easy preparation [7]. Since the first studies of Uhrilir [1] and Turner [14], and lately Canham [4], porous silicon has been mainly obtained by electrochemical dissolution of silicon wafers in solutions based on hydrofluoric acid (HF) [15].

A schematic diagram of the porous silicon formation process can be seen in Fig. 2.1. A possible anodization cell employs platinum cathode and silicon wafer anode immersed in a solution containing hydrofluoric acid (HF). Following an electrochemical reaction occurring at the Si surface a partial dissolution of Si settles in.

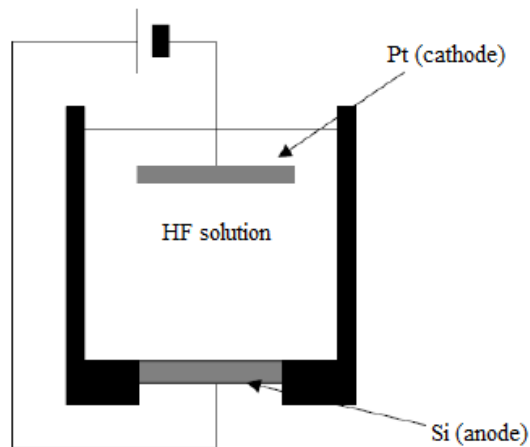


Figure 2.1: *Schematic diagram of the porous silicon anodization circuit.*

Usually, HF is dissolved in an aqueous solution with up to 50% of HF. Due to the hydrophobic character of the clean Si surface [16], absolute ethanol is usually added to the aqueous solution to increase the wettability of the PS surface. In fact, ethanoic solutions infiltrate the pores, while purely aqueous HF solutions do not. This is very important for the lateral homogeneity and the uniformity of the PS layer in depth. In

addition, during the reaction occurs hydrogen evolution and bubbles form and stick on the Si surface in pure aqueous solutions. Ethanol also acts as a surfactant agent and assists in removing hydrogen bubbles from the surface of the Si substrate. Moreover, it has been found that lateral inhomogeneity and surface roughness can be reduced increasing electrolyte viscosity by introducing glycerol to the composition of the HF solution [17]. The dissolution is obtained either controlling the anodic current or the voltage. Generally, it is preferable to work with constant current, because it allows a better control of porosity, thickness and reproducibility of the PS layer.

PS is composed of a silicon skeleton permeated by a network of pores. It is possible to define the characteristics of a particular porous silicon layer in a number of ways. The methods of identification include the average pore diameter and silicon branch widths, porosity, pore and branch orientation, and layer thickness. The specific nature of a layer depends on the fabrication conditions used, including the substrate doping and type, the hydrofluoric acid (HF) concentration, the anodization current density and the anodization time. The techniques used to assess these properties include various microscopy techniques (pore diameter, microstructure and layer thickness), gravimetric analysis [18] (porosity and layer thickness) and gas adsorption isotherms [19] (pore diameter).

Although new analysis techniques have been recently used to study porous silicon, the understanding of PS formation still comes from the I - V relationships, and a basic knowledge of silicon electrochemistry is essential to understand the fundamentals of pores formation [20–22]. Fig. 2.2 shows the typical I - V curves for n- and p-type doped Si in aqueous HF.

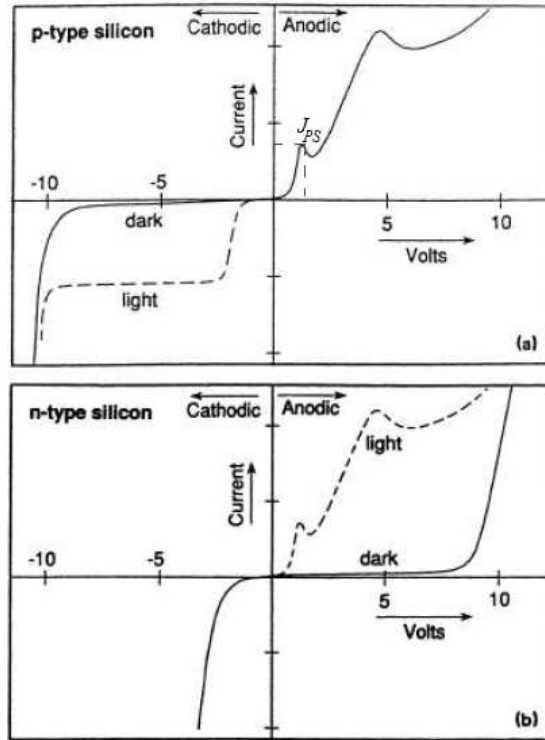


Figure 2.2: I - V curves for n - and p -type doped silicon in aqueous HF . The solid line indicates the dark response and the dashed line shows a response under illumination. The first (lower) current peak J_{PS} corresponds to the formation of a surface anodic oxide formed during electropolishing. The second (higher) current peak marks the beginning of stable current (potential) oscillations with the possible formation of a second type of anodic oxide. The dotted area indicates the useful regime for the formation of PS.

In this section we outline only the basic electrochemical features of the I - V relationships. The I - V curves show some similarities to the normal Schottky diode behavior expected for a semiconductor/electrolyte interface, including photogenerated currents at reverse bias. But there are also some important differences [7]. The first is that while the sign of majority carriers changes between n - and p -type, the chemical reactions at the interface remain the same. Second, the reverse-bias dark currents are at least three orders of magnitude higher than those normally expected for Schottky diodes.

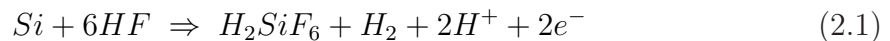
Both n - and p -type Si are stable under cathodic polarization. The only important cathodic reaction is the reduction of water at the silicon/HF interface, with the

simultaneous formation of hydrogen gas. This reaction occurs only at high cathodic overpotentials or, using Schottky-diode terminology, at reverse biased breakdown. Dissolution of silicon occurs only under anodic polarization. At high anodic overpotentials the silicon surface electropolishes and the surface retains a smooth and planar morphology. On the contrary, at low anodic overpotentials the surface morphology is dominated by a dense array of channels penetrating deeply into the bulk of the Si [7].

The pores formation occurs only during the initial rising part of the $I-V$ curve, for a potential value below the potential of the first sharp peak. The current at this peak is named as the electropolishing current (J_{PS}). The zone of the $I-V$ curve at which the pores formation occurs is grey colored in Fig. 2.2. The quantitative values of the $I-V$ curves, as well as the values corresponding to the electropolishing peak, depend on etching parameters and wafer doping. For n-type substrates, this typical $I-V$ behavior is observed only under illumination because a holes supply is needed [23].

2.2.2 Chemistry of the formation of porous silicon

The exact mechanism for pores formation in a silicon substrate is still in question and several mechanisms have been proposed [24]. However, it is generally accepted that holes are required for both electropolishing and pores formation. During pores formation two hydrogen atoms evolve for every Si atom dissolved [25]. The hydrogen evolution diminishes approaching the electropolishing regime and disappears during electropolishing. Current efficiencies are about two electrons per dissolved Si atom during pores formation [26, 27]. The global anodic semi-reactions can be written during pores formation as



The final and stable product for silicon in HF is H_2SiF_6 , or some of its ionized forms; it follows that during the pores formation only two of the four available silicon electrons participate in an interface charge transfer while the remaining two undergo a corrosive hydrogen formation.

While it is generally accepted that pores initiation occurs at surface defects or irregularities, different models have been proposed to explain pores formation. Among the various models proposed for the silicon dissolution reaction, the mechanism presented by Lehmann and Gösele [28] is the most accepted in the porous silicon community. Whether this is the correct dissolution process is unclear [24] but it explains the hydrogen gas evolved during anodization, and the need for a hole supply for the dissolution to occur, a generally accepted requirement [29]. Lehmann and Gösele expanded their model by suggesting that, providing the current density remains below J_{ps} , the pore formation is self-limited by the availability of holes within the silicon branches. For p-type silicon substrates under anodic bias, the limitation of the hole supply may be caused by quantum confinement.

Similarly to most semiconductor junctions, at the Si/electrolyte interface a depletion zone is formed (see Fig. 2.3). The width of the depletion zone depends on the doping density and it is also related to the size of the pores. In addition, the depletion layer width depends on the surface curvature: the anodization preferentially occurs at the pores tips where the curvature is largest. Moreover, when the depletion zones of adjacent pores meet each other, the current flow is suddenly pinched off. As further practical consequence, in stationary conditions, the porosity remains approximately constant, whereas the overall thickness of the porous silicon layer grows essentially linearly in time. Further dissolution occurs only at the pores tips, where enough holes are available. In this way the etching of porous silicon proceeds in depth with an overall directionality which follows the anodic current paths inside silicon.

In the dissolution of n-type silicon, an external source of light is necessary to obtain a sufficient holes flux density [30]. In fact, the dissolution of n-type silicon hardly occurs

without illumination, but it is possible in wafers with a high doping level [31]. The etching process leads to a very regular pores growth.

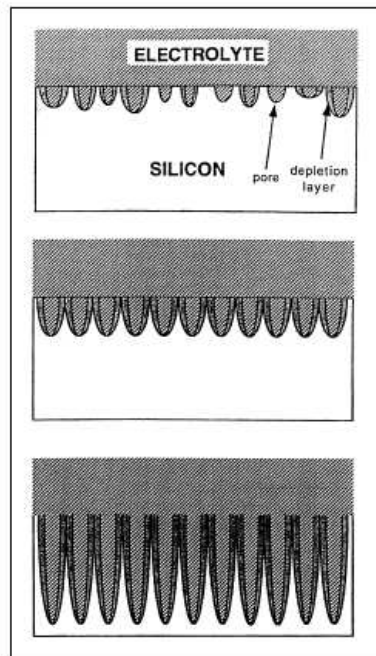


Figure 2.3: Pores formation in porous silicon. The upper figure shows the initial stage, where the pores develop randomly on the silicon surface. In the middle, the self-regulating process is shown. When the depletion zones around each pore overlap, the pore growth changes from an isotropic growth to a highly directional growth. The bottom figure shows how the dissolution advances only at the pore tips.

Up to this point, we can say that the main requirements for porous silicon formation are:

- The silicon wafer must be anodically biased. This corresponds to forward biasing for p-type doped silicon, and reverse biasing for n-type doped silicon;
- For n-type doped and semi-insulating p-type doped silicon, light must be supplied;
- Current densities below the critical value, J_{PS} , must be used.

The first two conditions are due to the fact that holes are consumed during the silicon etching. When the third condition is not fulfilled, the reaction is limited by mass transfer to the solution: holes pile up at the silicon-HF interface and electropolishing occurs. For all the three conditions mentioned above, the holes play an important role: in fact, PS formation is a self-regulated mechanism, with holes depletion as the limiting agent. The dissolution reaction begins at defects on the silicon wafer surface, the pores are formed and their walls are eroded until they are emptied of the holes. The overall etching process is self-adjusting and the average pore size is given only by the electrochemical parameters.

2.2.3 Pore size and morphology

The existing nomenclature, adopted by the International Union of Pure and Applied Chemistry (IUPAC), distinguishes three categories for the PS with regard to the pore dimensions [32]:

- micropores (average pore diameter $d \leq 2 \text{ nm}$);
- mesopores (average pore diameter $2 \text{ nm} < d < 50 \text{ nm}$);
- macropores (average pore diameter $d \geq 50 \text{ nm}$).

However, in the following I will call the porous substrates utilized in this thesis with the term *nanoporous*, since it is current custom in the superconductivity community to use this nomenclature for templates in which pores have dimensions of the order of tenth of nanometers.

The categorization above is related only to the pore diameter, but does not contain much information about the pore morphology. The term pore morphology is used for properties like shape (smooth, branched, etc.), orientation, interconnection of pores,

etc. The morphology is the least quantifiable aspect of PS. It is very difficult to characterize systematically the morphology of PS, which is extremely rich with respect to variations in pores size, shape and spatial distribution. In terms of the pore morphology, it can be summarized that microporous and mesoporous silicon exhibit typically a sponge-like structure with densely and randomly branched pores, which do not show a clear orientation. The tendency to branch increases with decreasing pores diameter. In contrast, macroporous silicon can have discrete pores with smooth walls and with short branches.

The pores grow preferentially along $\langle 100 \rangle$ direction and towards the source of positive carriers (holes), which are involved in the electrochemical dissolution reaction, probably because the (100) planes present the most favored geometry for the chemical attach [15, 33].

Moreover, the formation of PS is selective with respect to the doping of the substrate. Some general trends on the layer morphology can be derived for different types of starting silicon substrates. For p-type doped silicon both size and interpore spacing are very small, typically between 1 and 5 nm, and the pores network appears very homogeneous and interconnected. As the dopant concentration increases, pores size and interpore spacing increases. The structure becomes anisotropic, with long voids running perpendicular to the surface.

For n-type doped silicon the situation is more complicated. Generally, pores in n-type doped silicon are much larger than in p-type doped silicon, and pores size and interpore spacing decrease with increasing dopant concentration. Generally, the pores tend to form a randomly directed filamentary structure and large straight channels approaching the electropolishing regime. Lightly doped n-type substrates anodized in the dark have low porosity (1-10 %), with pores in the micrometer range. Under illumination higher values of porosity can be achieved, and mesopores are formed together with macropores. The final structure depends strongly on anodization conditions, especially on light intensity [30] and current density [7]. While highly n- and p-type

doped silicon show similar structures.

2.2.4 Anodization parameters

The PS formation process with electrochemical anodization has been widely developed by many authors [34–36]. As I wrote above, all the properties of PS, such as porosity, thickness, pore diameter and microstructure depend on anodization parameters. These conditions include HF concentration, current density, wafer type and resistivity, anodization duration, illumination (required for n-type silicon) and temperature (see Table 2.1).

The porosity is defined as the fraction of void within the PS layer and can be easily determined by weighing the silicon substrate both before and after anodization (m_1 and m_2 respectively), and again after a rapid dissolution of the whole porous layer in a 3% KOH solution (m_3) [7]. The porosity (P) is then calculated by

$$P(\%) = \frac{(m_1 - m_2)}{(m_1 - m_3)} \quad (2.2)$$

For p-type doped substrates, and for a fixed HF concentration the porosity increases with increasing current density. For fixed current density, the porosity decreases with decreasing HF concentration (see Fig. 2.4). Fixing the HF concentration and the current density, the porosity increases with the thickness.

	Porosity	Etch rate	Critical current
HF concentration	decreases	decreases	increases
Current density	increases	increases	–
Anodization time	increases	almost constant	–
Temperature	–	–	increases
Wafer doping (p-type)	decreases	increases	increases
Wafer doping (n-type)	increases	increases	–

Table 2.1: *Effect of anodization parameters on PS formation. An increase of the parameters of the first column leads to a variation of the elements in the rest of columns.*

This happens because of the extra chemical dissolution of the porous silicon layer in HF. The thickness of a porous silicon layer is determined by the time that the current density is applied, that is the anodization time. To have a thicker layer, a longer anodization time is required.

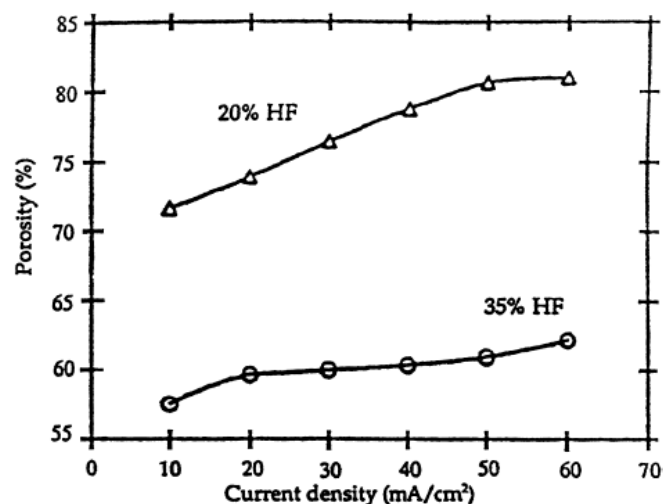


Figure 2.4: *Porosity as a function of current densities for different HF concentrations, for highly doped p-type silicon substrate [7].*

For heavily n-type doped Si, the porosity as a function of current density is quite different from the corresponding curves obtained for p-type doped substrates. The porosity exhibits a sharp minimum (see Fig. 2.5). For higher current densities the

behavior is similar to the p-type doped substrates, but for lower current densities the porosity increases sharply. This large increase in porosity is not explained simply by chemical dissolution but it is due to a difference in microstructure.

The formation of PS is selective with respect to the doping of the substrates. Heavily doped regions are etched faster than low doped regions [37, 38].

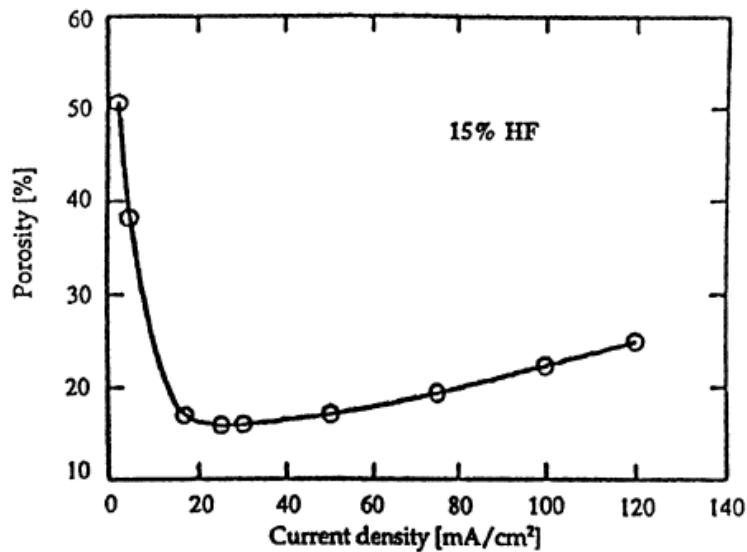


Figure 2.5: Porosity is a function of current densities for highly doped n-type silicon substrate [7].

An advantage of the formation process of porous silicon is that once a porous layer has been formed, no electrochemical etching occurs during the following current density variations. Hence, the porosity can be modulated in depth [39]. A longer permanence time of silicon in HF solution results in a higher mass of chemically dissolved silicon. This effect is more important for lightly doped silicon, while it is almost negligible for heavily doped silicon. This is due to the lower specific surface area. All these characteristics contribute to the easy formation of porous silicon structures, with no need to use excessively expensive equipment.

Bibliography

- [1] A. Uhlir, Bell Syst. Tech. J. **35**, 333 (1956).
- [2] Y. Watanabe and T. Sakai, Rev. Electron. Commun. Labs. **19**, 899 (1971).
- [3] Y. Watanabe, Y. Arita, T. Yokoyama, and Y. Igarashi, J. Electrochem. Soc. **122**, 1351 (1975).
- [4] L.T. Canham, Appl. Phys. Lett. **57**, 1046 (1990).
- [5] A.G. Cullis, L.T. Canham, and P.D.J. Calcott, J. Appl. Phys. **82**, 909 (1997).
- [6] A. Halimaoui, C. Oules, G. Bromchil, A. Bsiesy, F. Gaspard, R. Herino, M. Ligeon, and F. Muller, Appl. Phys. Lett. **59**, 304 (1991).
- [7] O. Bisi, S. Ossicini, and L. Pavesi, Surf. Sci. Rep. **38**, 1 (2000).
- [8] K.D. Hirschman, L. Tsybeskov, S.P. Duttagupta, and P.M. Fauchet, Nature **384**, 338 (1996).
- [9] C.C. Striemer and P.M. Fauchet, Appl. Phys. Lett. **81**, 2980 (2002).
- [10] C. Mazzoleni and L. Pavesi, Appl. Phys. Lett. **67**, 2983 (1995).
- [11] V.S.Y. Lin, K. Motesharei, K.P.S. Dancil, M.J. Sailor, and M.R. Ghadiri, Science **278**, 840 (1997).
- [12] S. Chan, P.M. Fauchet, Y. Li, L.J. Rothberg, and B.L. Miller, Phys. Status Solidi A **182**, 541 (2000).

-
- [13] F. Cunin, T.A. Schmedake, J.R. Link, Y. Li, J. Koh, S.N. Bhatia, and M.J. Sailor, *Nature Mater.* **1**, 39 (2002).
- [14] D. R. Turner, *J. Electrochem. Soc.* **105**, 402 (1958).
- [15] R.L. Smith and S.D. Collins, *J. Appl. Phys.* **71**, 1 (1992).
- [16] L.T. Canham, *Appl. Phys. Lett.* **63**, 337 (1993).
- [17] S. Setzu, S. Letant, P. Solsona, R. Romestain, and J.C. Vial, *J. Lumin.* **80**, 129 (1999).
- [18] D. Brumhead, L.T. Canham, D.M. Seekings, and P.J. Tufton, *Electrochimica Acta* **38**, 191 (1993).
- [19] R. Herino, G. Bomchil, K. Barla, and C. Bertrand, *J. Electrochem Soc.* **134**, 1994 (1987).
- [20] H. Föll, *Appl. Phys. A* **53**, 8 (1991).
- [21] X.G. Zhang, R.L. Smith, and S.D. Collins, *J. Electrochem. Soc.* **136**, 1 (1989).
- [22] J.B. Flynn, *J. Electrochem. Soc.* **105**, 715 (1958).
- [23] M.I.J. Beale, I.D. Benjamin, M.J. Uren, N.G. Chew, and A.G. Cullis, *Appl. Phys. Lett.* **46**, 86 (1985).
- [24] R.L. Smith and S.D. Collins, *J. Appl. Phys.* **71**, 1 (1992).
- [25] C. Pickering, M.I.J. Beale, D.J. Robbins, P.J. Pearson, and R. Greef, *J. Phys. C* **17** 6535 (1984).
- [26] M.I.J. Beale, J.D. Benjamin, M.J. Uren, N.G. Chew, and A.G. Cullis, *J. Crystal Growth* **73**, 622 (1985).
- [27] V. Lehmann and H. Föll, *J. Electrochem. Soc.* **137**, 653 (1990).
- [28] V. Lehmann and U. Gösele, *Appl. Phys. Lett.* **58**, 856 (1991).

- [29] R. Memming and G. Schwandt, *Surface Science* **4**, 109 (1966).
- [30] J. Jakubowicz, *Superlattice Microst.* **41**, 205 (2007).
- [31] H. Jungblut, J. Jakubowicz, S. Schweizer, and H.J. Lewerenz, *J. Electroanal. Chem.* **572**, 41 (2002).
- [32] P. Müller, *IUPAC Manual of Symbols and Technology, Pure Appl. Chem.* **31**, 578 (1972).
- [33] P.C. Searson, J. Macalay, and F.M. Ross, *J. Appl. Phys.* **72**, 253 (1992).
- [34] A. Bruyant, G. Léron del, P.J. Reece, and M. Gal, *Appl. Phys. Lett.* **82**, 3227 (2003).
- [35] J. Charrier, M. Guendouz, L. Haji, and P. Joubert, *Phys. Stat. Sol. (a)* **182**, 431 (2000).
- [36] L. De Stefano, L. Moretti, A.M. Rossi, and I. Rendina, *Sen. Actuators A* **104**, 179 (2003).
- [37] H. Higa and T. Asano, *Jpn. J. Appl. Phys.* **35**, 6648 (1996).
- [38] M. Ligeon, F. Muller, R. Herino, F. Gaspard, A. Halimaoui, and G. Bomchil, *J. Appl. Phys.* **66**, 3814 (1989).
- [39] E. Lorenzo, C.J. Oton, N.E. Capuj, M. Ghulinyan, D. Navarro Urrios, Z. Gaburro, and L. Pavesi, *Applied Optics* **44**, 5415 (2005).

Chapter 3

Matching effects: experimental results

In this chapter, firstly resistive transitions on a perforated Nb thin film with a lattice of holes with the period of the order of tens of nanometers are presented. Bumps in the dR/dH versus H curves are observed at the first matching field and its fractional values, $1/4$, $1/9$ and $1/16$. This effect is related to different vortex lattice configurations made available by the underlying lattice of holes. Then, I introduce another experimental result that is high field vortex matching effects in superconducting Nb thin films with a periodic nanometer-sized square array of antidots. Nb thin films containing a regular square array of antidots with 17 nm diameter and 50 nm inter-pore spacing have been fabricated using a relatively simple lithographic process. The critical current density $J_c(H)$ curves, obtained by electric transport measurements, exhibit commensurability effects with pronounced maxima just above the expected $H_1 = 0.830$ Tesla and $H_{1/2} = 0.415$ Tesla matching fields, down to temperatures as low as 2.3 K.

3.1 Evidence of fractional matching states

As I have already discussed before, recent progress in the fabrication of nanostructures provide the possibility to realize superconducting thin films containing artificial defects as pinning sites with well-defined size, geometry and spatial arrangement [1, 2]. In particular, the use of regular array of pinning centers such as antidots [1, 3–5] or magnetic dots [2, 6–8] brings to new commensurability effects, which give additional insight into the pinning properties of vortices. The most notable phenomenon for these studies is the so-called matching effect which occurs when the vortex lattice is commensurate with the periodic pinning array. As a result, at the matching field, the critical current density, J_c , is drastically enhanced [2, 3, 9] and moreover, as a consequence of the Little-Parks effect [10], the upper critical magnetic field is increased at the matching values. Recently antidot arrangements with a big variety of symmetries have been investigated [11–13].

If the artificial structure of defects is created by lithographic technique, the matching fields are usually in the range of a few Oersteds. For this reason, matching effects are observed in a very narrow temperature region, close to the critical temperature T_c , for a reduced value $t = T/T_c \geq 0.95$. In order to both increase the matching field and decrease the temperature where the effect is present, the period of the pinning structure should be reduced to less than 100 nm. This gives, in fact, the possibility to increase H_1 up to 1 Tesla or even higher. A reasonable method to achieve this goal is to use self-assembled substrates, such as, for example, Al_2O_3 templates with characteristic features in the nanometric scale [14]. The pore diameter in Al_2O_3 substrates could easily be varied in the range 25-200 nm with porosity (i.e. interpore spacing, a) around 50%, and this gives the possibility to achieve matching fields of thousands of Oersteds [14].

Very recently, another very promising material for self-assembled substrates and an optimum candidate for the Nb growth was proposed, namely, porous silicon (PS)

[15]. As already mentioned in the second chapter, PS is constituted by a network of pores immersed in a nanocrystalline matrix [16] and it is a material which offers a considerable technological interest in different fields, as for instance micro-and optoelectronics [17] and gas sensing [18, 19]. The diameter of pores, \emptyset , in PS can easily be varied from 200 nm down to 5 nm by using substrates with appropriate doping (n or p) and different regimes of anodization. The porosity, in fact, can be varied in the range 30-90% by adjusting parameters such as the acid solution, the anodizing current density and the illumination of the substrate during the anodization. The regularity of the pores arrangement, however, is of the order of 10% lower than the one observed in Al_2O_3 templates obtained by electrochemical oxidation [20]. It has been demonstrated [15] that thin Nb films deposited on PS substrates can inherit their structure made of holes. The resulting samples then consist of porous Nb thin films with in plane geometrical dimensions, a and \emptyset , comparable with the superconducting coherence length, $\xi(T)$. In these samples, matching fields of the order of 1 Tesla were experimentally observed [15].

Aim of this section is to deepen the study of the matching effect in superconducting Nb thin films deposited on PS. Superconducting properties were investigated by transport measurements in the presence of magnetic fields applied perpendicularly to the samples surface, down to $t = 0.52$. As a consequence of the high density of the pore network, the (H, T) phase diagram presents a deviation from the classic linear dependence. This effect appears at the first matching field $H_1 \approx 1$ Tesla, a value larger than those typical of periodic pinning arrays obtained both by lithographic techniques and by using another kind of self-organized templates. Moreover a new effect related to the commensurability between the vortex lattice and the underlying pinning structure was found. It consists in the appearance of pronounced structures in the derivative of the $R(H)$ curves, dR/dH , which can be observed in correspondence of the first matching field and its fractional values.

3.1.1 Sample fabrication

Porous layers have been fabricated at the University of Minsk (Belarus), by electrochemical anodic etching of n-type, 0.01 Ωcm , monocrystalline silicon wafers. The electrochemical dissolution has been performed in 48% water solution of HF, applying a current density of 20 mA/cm². The anodization time was chosen in the range of 0.5 - 4 min in order to get porous layers with a thickness ranging from 0.5 to 4 μm . The pores extend on a surface of about 1 cm². The integral porosity has been estimated by gravimetry to be of about 50% [21]. The resulting porous substrates have diameter $\emptyset = 10$ nm and interpore spacing $a = 20$ nm for some substrates and $a = 40$ nm for others. For the lattice with $a = 40$ nm, if the formula $H_1 = \Phi_0/a^2$ for the square lattice is used, the expected first matching field is $H_1 = 1.3$ Tesla.

Nb thin films have been grown, at the University of Salerno, on the top of the porous Si substrates in an UHV dc diode magnetron sputtering system with a base pressure in the low 10^{-8} mbar regime and sputtering Argon pressure of 3.5×10^{-3} mbar. In order to reduce the possible contamination of the porous templates, the substrates have been heated at 120°C for one hour in the UHV chamber. The deposition was then realized at room temperature after the cool off of the substrates. The films have been deposited at typical rates of 0.33 nm/s, controlled by a quartz crystal monitor calibrated by low-angle X-ray reflectivity measurements. Since the effect of the periodic template would be reduced when the film thickness, d_{Nb} , exceeds the pore diameter, \emptyset , [15] the Nb thickness was chosen to be 8.5 nm for porous substrates with $a = 40$ nm and 9 nm for the ones with $a = 20$ nm. A reference Nb thin film 8.5 nm thick has been grown on a non-porous Si substrate in the same deposition run, i.e. under identical deposition conditions. For the sake of clarity the samples will be named using the initials Si followed by a number indicating the nominal substrate interpore distance, a , and Nb followed by a number for the Nb thickness. For example, Si40-Nb8.5 is the Nb film 8.5 nm thick, grown on the porous substrates with $a = 40$ nm.

3.1.2 Experimental results and discussion

A typical field emission scanning electron microscopy (FESEM) micrograph (magnification=600000) of the top of the Nb thin film Si20-Nb9 is shown in Fig. 3.1. The pores restrict the solid angle from which low energy electrons can escape, thus rendering the pores dark and the top surface light. The surface appearance, far from being perfectly ordered, however, clearly reveals the holes in the Nb layer. The image also reveals that the pore entrances are not regular circles.

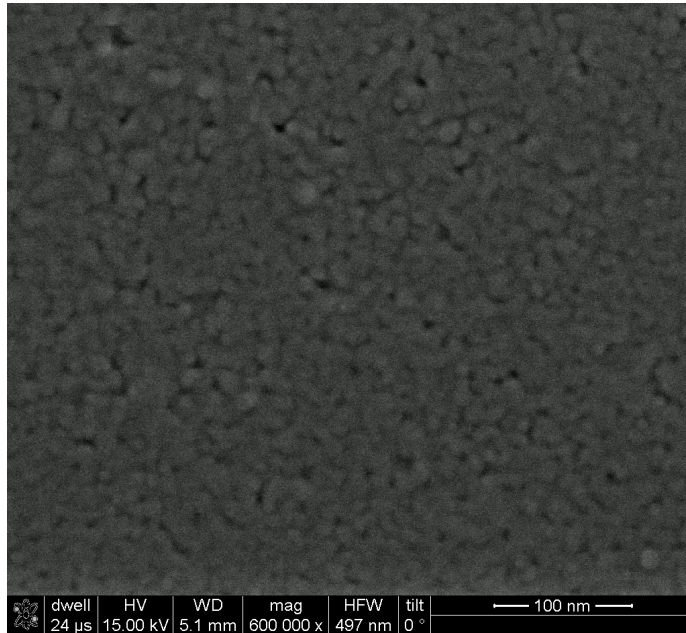


Figure 3.1: *FESEM image (magnification=600000) of a Nb film 9 nm thick deposited on the porous substrate with interpore spacing $a = 20$ nm.*

The superconducting properties were resistively measured in a ^4He cryostat using a standard dc four-probe technique on unstructured samples. The critical temperature was defined at the midpoint of the $R(T)$ transition curves. The value of the transition temperatures of the film grown on the porous substrate with $a = 40$ nm and of the reference sample in the absence of the magnetic field were $T_c = 3.83$ K and $T_c = 4.53$ K, respectively (see Fig. 3.2).

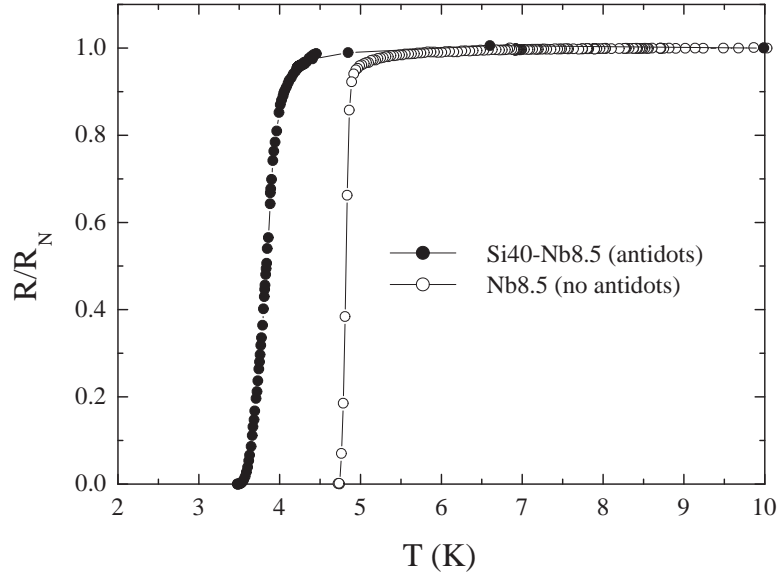


Figure 3.2: Normalized $R(T)$ transition curves for the Nb film with antidots ($Si_{40}-Nb_{8.5}$, solid circles) and for the reference sample ($Nb_{8.5}$, open circles).

The critical temperature depression in the case of the porous sample is consistent with what already reported in literature for films grown both on Al_2O_3 [14] and on PS [15]. The first step for the characterization of the behavior of the porous Nb sample in the presence of perpendicular magnetic field is the determination of its (H, T) phase diagram. The temperature dependence of the perpendicular upper critical field, $H_{c2\perp}$, was obtained performing resistance vs field, $R(H)$, measurements at fixed values of the temperature with a temperature stability of 1 mK. $H_{c2\perp}$ was defined at the midpoint of each of the $R(H)$ curves.

In Fig. 3.3 the (H, T) phase diagrams of the Nb thin films are shown. As already mentioned in the first chapter, the perpendicular upper critical field of superconducting films of thickness d obeys a linear temperature dependence [22]

$$H_{c2\perp}(T) = \frac{\Phi_0}{2\pi\xi_{0\parallel}^2} \left(1 - \frac{T}{T_c} \right) \quad (3.1)$$

where $\xi_{0\parallel}$ is the Ginzburg-Landau coherence length parallel to the sample surface at $T = 0$. The temperature dependence of ξ_{\parallel} is $\xi_{\parallel}(T) = \xi_{0\parallel}/\sqrt{1 - T/T_c}$. Another superconducting parameter to be held into account is the magnetic field penetration depth, λ , whose temperature dependence is $\lambda(T) = \lambda_0/\sqrt{1 - T/T_c}$, where λ_0 is the penetration depth at $T = 0$.

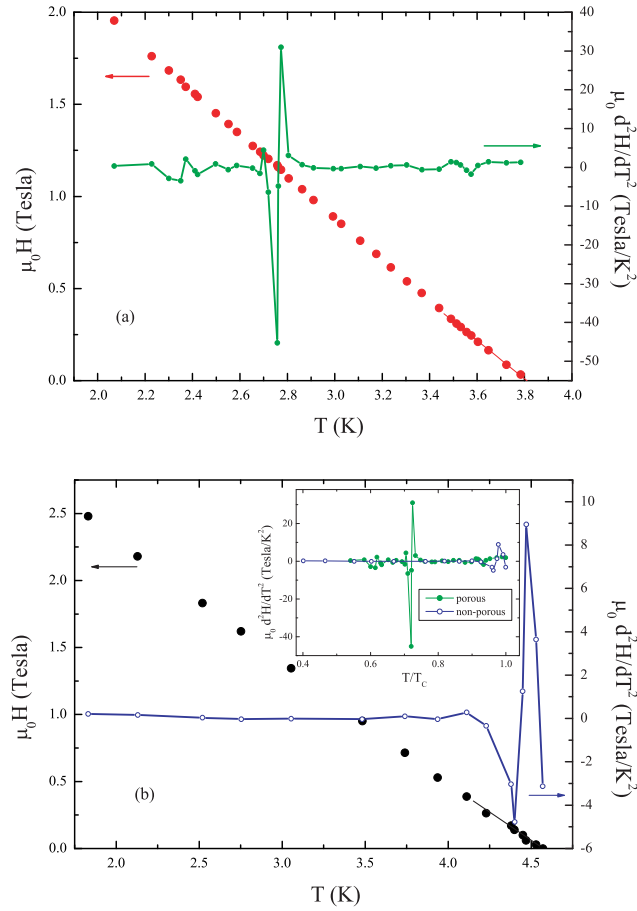


Figure 3.3: *Left scale: Perpendicular upper critical field $H_{c2\perp}$ vs temperature of the Nb thin film with $d_{Nb} = 8.5$ nm grown on (a) porous template and (b) non-porous reference substrate. The linear fits to the data close to T_c are also shown. Right scale: $dH_{c2\perp}^2/dT^2$ versus temperature. The inset shows the comparison between the second derivatives as functions of the reduced temperature of two samples, grown on the porous template (full circles) and on the non-porous template (open circles).*

The $H_{c2\perp}(T)$ curve obtained for the Nb film deposited on porous Si template, reported in Fig. 3.3(a), presents some peculiarities, which indicate that the superconducting

properties are influenced by the introduction of the porous array. In fact, if the $H_{c2\perp}$ second derivative versus the temperature is plotted we can see that it changes its sign from positive to negative at $H \approx 1.16$ Tesla. This field value is very close to the nominal first matching field that we expect for the porous Si template, $H_1 \approx 1.30$ Tesla, assuming a square porous array. This change in concavity was already reported in a previous study on the same kind of samples, and it was ascribed to the formation of a commensurate vortex structure [15]. From the measured value of H_1 it follows that the period of the porous template is $a = 42$ nm. In the following we will identify $a_0 \equiv 42$ nm. In Fig. 3.3(b) is reported the $H_{c2\perp}(T)$ curve for the Nb reference film of the same thickness deposited on the non-porous template. As expected the $H_{c2\perp}(T)$ behavior is linear over the all temperature range and the $H_{c2\perp}$ second derivative versus temperature does not present any peculiarity except for a shallow peak near T_c . In the inset of Fig. 3.3(b), for sake of comparison, the $dH_{c2\perp}^2/dT^2$ versus the reduced temperature is reported for both the Nb films, in order to point out the difference in their magnitude. A fit to the data close to T_c with the expression for $H_{c2\perp}(T)$ reported above, yields a value of the Ginzburg-Landau coherence length at $T = 0$, $\xi_{0\parallel} = 9.1$ nm and $\xi_{0\parallel} = 9.5$ nm, resulting in a superconducting coherence length $\xi_S = 5.8$ nm and $\xi_S = 6.0$ nm, for the Nb porous sample and the Nb reference film, respectively. The values of $\xi_{0\parallel}$ are significantly smaller than the BCS coherence length of Nb, $\xi_0 = 39$ nm [23], indicating that our films are in dirty limit regime with an electron mean free path of $l = 1.38 \xi_{0\parallel}^2 / \xi_0 \approx 3$ nm [24]. Since the film dimensions in the xy plane are larger than $\xi_{\parallel}(T)$, the expression for $H_{c2\perp}(T)$, reported above, is verified in the whole temperature range. The Ginzburg-Landau parameter, $\kappa = \lambda(0)/\xi_{0\parallel}$, can be estimated using the expression $\kappa = 0.72\lambda_L/l = 9.6$, where $\lambda_L = 39$ nm is the London penetration depth of Nb [23]. Ratios of $\xi_{0\parallel}/a \approx 0.2$ and $\lambda(0)/a \approx 2.1$, measured for $a_0 = 42$ nm, are larger than in previous works [25, 26] on perforated Nb samples, and indicate that we are in presence of individual vortex pinning [27]. Moreover, the pore diameter, \emptyset , in our PS template is comparable with the vortex core dimension at $T = 0$, $\emptyset \approx \xi_{0\parallel}$. This means that the saturation number, $n_S = \frac{\emptyset}{4\xi_S(T)}$, defined as the maximum number

of vortices that fits into a pore with diameter \emptyset , is less or equal to 1, so that each pore can trap only one fluxon [28]. Subsequently multiquanta vortex lattice [1] cannot be observed in our system.

Now I move to a more careful inspection of the $R(H)$ curves of the Nb porous film. This will lead to the observation of a peculiar behavior of these transitions. In Figs. 3.4(a) and 3.4(b) $R(H)$ curves obtained for two different values of the temperature, $T = 3.490$ K and $T = 3.531$ K, respectively, are presented.

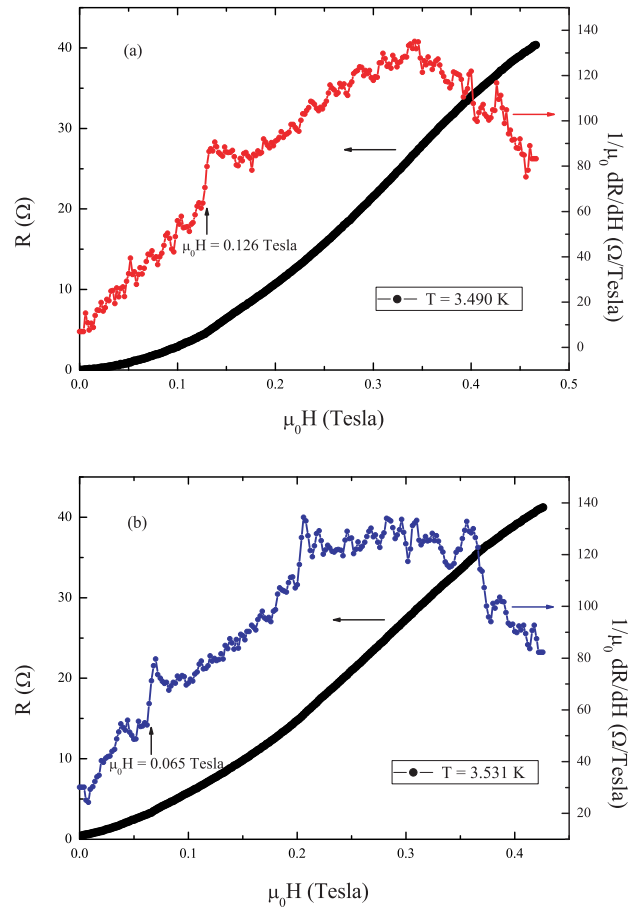


Figure 3.4: Left scale: $R(H)$ measurement at (a) $T = 3.490$ K and (b) $T = 3.531$ K. Right scale: dR/dH versus the applied magnetic field. In both panels the arrow indicates the field where the bump is present.

At first glance both the curves are rather smooth and do not present any structures or enlargements due, for example, to sample inhomogeneities. However if the dependence

of the first derivative dR/dH versus the applied magnetic field is analyzed, some distinct features can be observed. In particular in both the curves a small local maximum is present at specific values of the magnetic field. Let's focus on the position where the bumps, as indicated by an arrow in Fig. 3.4, start to develop. The bump in the first derivative reflects the presence of a small dip in the corresponding magnetic field dependence of the resistance $R(H)$ at the same value of H . This effect was ascribed to a pinning enhancement when the period of the vortex structure is commensurate with the period of the antidots [29]. The bumps in the dR/dH appear indeed in our curves at values of the magnetic fields H_n when the magnetic flux threading each unit cell is equal to the flux quantum, Φ_0 , or to fractional values of Φ_0 . In Fig. 3.4(a), where the $R(H)$ measurement at $T = 3.490$ K is shown, the peculiarity in dR/dH is, in fact, observed at $H_{bump} \approx 0.126$ Tesla. The period of the vortex lattice at this field value is $a_0^{(3)} = 128$ nm, i.e. about three times the interpore spacing of this analyzed sample, $a_0 = 42$ nm. Consequently this field value corresponds to one-ninth of the matching field $H_1/9 \approx 0.129$ Tesla. Similarly, in Fig. 3.4(b) where the $R(H)$ measurement at $T = 3.531$ K is shown, the bump in dR/dH develops at $H_{bump} \approx 0.065$ Tesla. The period of the vortex array at this field is then $a_0^{(4)} = 178$ nm, which is about four times the interpore spacing of this sample. Consequently this field value corresponds to one-sixteenth of the matching field $H_1/16 \approx 0.072$ Tesla. An additional bump structure is present at $H \approx 0.2$ Tesla. However, this field value does not correspond to any commensurate vortex configuration (see discussion below) and does not survive repeating the measurement in the same temperature range. For this reason it will be not considered in the following analysis.

In Fig. 3.5, where the $R(H)$ measurement at $T = 3.513$ K is shown, the peculiarity in dR/dH is observed at $H \approx 0.255$ Tesla. This field value corresponds to one-fourth of the first matching field $H_1/4 \approx 0.29$ Tesla. The period of the vortex lattice at this field value is $a_0^{(2)} = 90$ nm, i.e. about two times the interpore spacing of this analyzed sample. All the field values reported above have been calculated assuming a square lattice. On the contrary, if a triangular array is considered for the pores the measured

field values do not match with calculated ones.

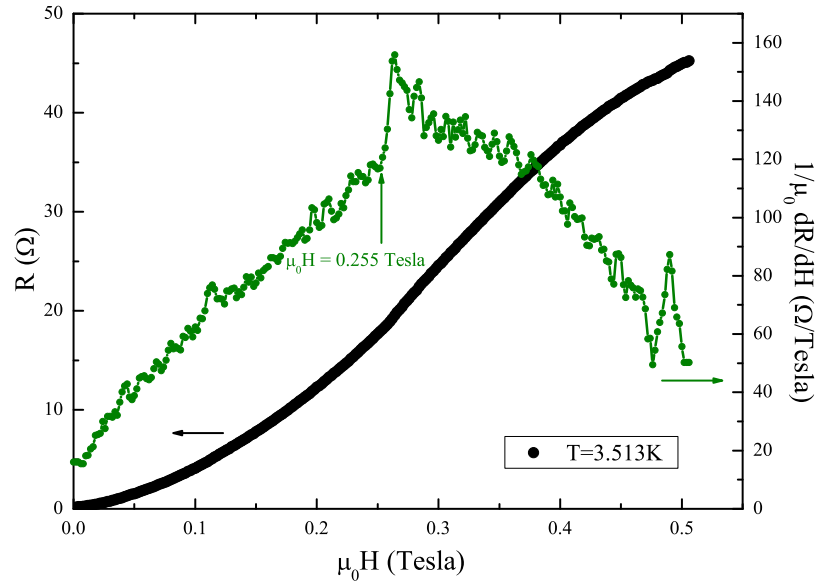


Figure 3.5: *Left scale: $R(H)$ measurement at $T = 3.513$ K of the sample $Si_{40}Nb_{8.5}$. Right scale: dR/dH versus the applied magnetic field. The arrow indicates the field where the bump is present.*

Many $R(H)$ measurements at different temperatures have been performed and the behavior of all the corresponding dR/dH curves has been analyzed. A selection of these curves is reported in Fig. 3.6. Some of them have been obtained by sweeping the field upward and downward and no hysteresis has been detected. For instance, the curves at $T = 2.551$ K and $T = 3.304$ K present a bump at $H_{bump} = H_1$ and $H_{bump} = H_1/4$, respectively. By comparison a curve with no bump, measured at temperature $T = 2.805$ K, is also shown. In all curves the fields at which the bumps are observed are related to the first matching field through the relation: $H = H_1/n^2$ with $n = 1, \dots, 4$.

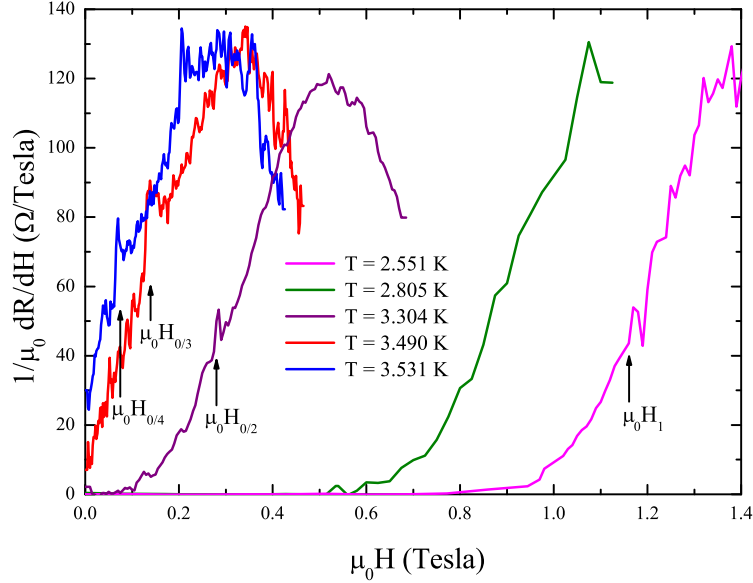


Figure 3.6: First derivatives, dR/dH , as a function of the applied magnetic field at different temperatures. The arrows indicate the field where the bump is present for each temperature.

The temperatures at which bumps are observed, the corresponding fields and their values normalized to H_1 , the ξ_S values, the vortex-vortex distances, $a_{k/l}$, and their values normalized to a_0 , are summarized in Table 3.1.

T (K)	H_{bump} (T)	H_{bump}/H_1	ξ_S (nm)	$a_{k/l}$ (nm)	$a_{k/l}/a_0$
2.551	1.160	1	10.02	42.0	1.00
3.304	0.275	1/4	15.66	87.0	2.07
3.490	0.126	1/9	19.44	128.0	3.05
3.531	0.065	1/16	20.76	178.0	4.24

Table 3.1: Temperatures at which the bumps are observed, corresponding fields and their values normalized to H_1 , ξ_S values at that temperature, vortex-vortex distances, $a_{k/l}$, and their values normalized to $a_0 = 42$ nm.

We argue that the presence of the observed bumps in the dR/dH curves can be related to different vortex lattice arrangements made possible by the array of holes. The

specific vortex lattice configurations occurring at the first matching field and at its fractional values are shown in Fig. 3.7.

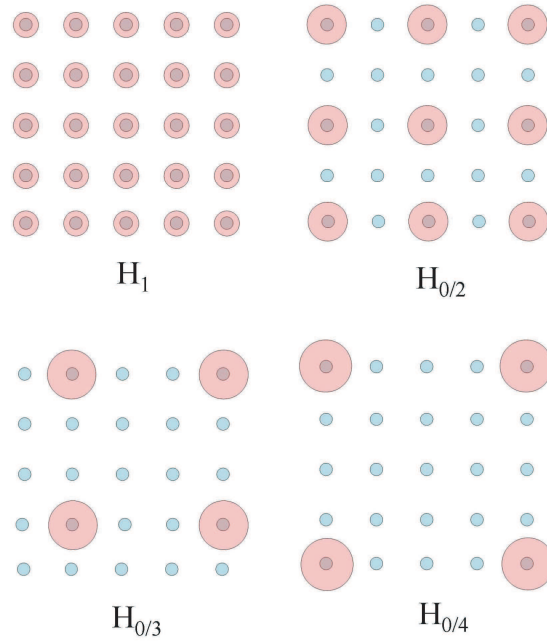


Figure 3.7: *Vortex lattice configurations occurring at the first matching field and its fractional values. Increasing the temperature the vortices diameter and their reciprocal distance increase, as reported in Table 3.1. Blue circles represent the holes, pink ones represent the vortices.*

In the case of $H_{bump}/H_1 = 1$ a commensurate square vortex configuration is formed, where each pore is occupied by a fluxon and the side of this square array is just $a_0 = 42$ nm. Increasing the temperature the vortices diameter ($\approx 2\xi_S$) and their reciprocal distance increase, as reported in Table 3.1. When $H_{bump}/H_1 = 1/4, 1/9$ and $1/16$ a square vortex lattice is again obtained with $a = 87$ nm, 128 nm and 178 nm, respectively. This means that the pores act as an ordered template of strong pinning centers, which is able to preserve the long-range positional order of the flux lattice also at low fields value, i.e. at higher vortex spacing. As already pointed out the optimization of the vortex structures leads to the formation of larger square flux lattices with respect

to the underlying artificial pinning array with the lattice constant a exactly equal to na_0 . The vortices tend to be placed as far from each other as possible due to the repulsive interaction between them and at the same time they want to follow the imposed square potential induced by the antidots. This constraint gives

$$a = a_0\sqrt{l^2 + k^2} \quad (3.2)$$

where l and k are integer numbers. Therefore, we should expect the fractional matching fields at [30]

$$H = H_{k/l} = \frac{\Phi_0}{a^2} = \frac{\Phi_0}{a_0^2(l^2 + k^2)} = \frac{H_1}{(l^2 + k^2)} \quad (3.3)$$

We observed bumps at fractional matching fields $H_{0/2}$, $H_{0/3}$ and $H_{0/4}$. The other bumps expected from the equation above at fractional fields $H_{k/l}$ with $k \neq 0$ have not been observed. All the fields values at which the bumps in the dR/dH appear are shown as points of coordinates (H_{bump}, T) in Fig. 3.8.

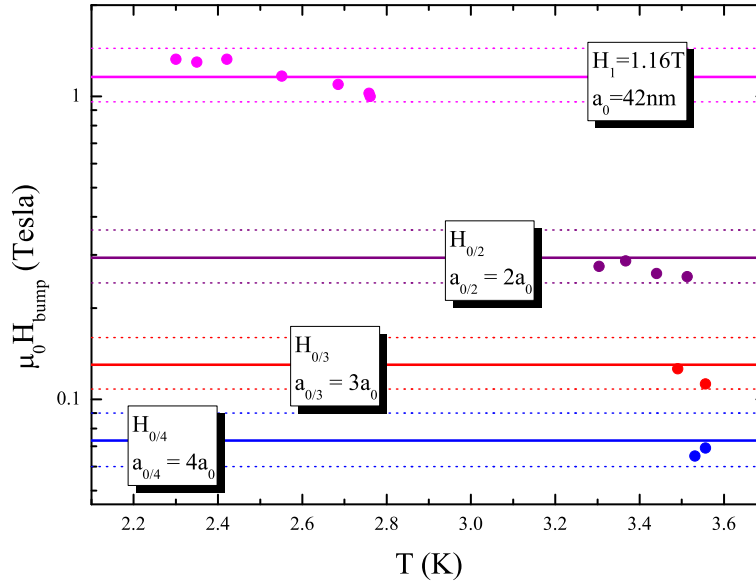


Figure 3.8: The points of coordinates (H_{bump}, T) identify the values of the fields and temperatures at which bumps have been observed in the dR/dH curves at fixed temperatures. The solid lines correspond to the different matching field orders achieved with the inter-pore spacing $a_0 = 42$ nm, while the dotted lines are obtained forasmuch as the regularity of the pore distance is achieved within the 10 percents of the average distance.

In this figure the solid lines correspond to the matching fields of different order, as calculated assuming an inter-pore spacing $a_0 = 42$ nm, through the formula $H_1 = \Phi_0/a_0^2$. The dotted lines are obtained considering a deviation from the corresponding mean inter-pore distance of the order of 10% [15]. It is worth noticing that all the data fall into the range theoretically estimated, suggesting that the observed peculiarities in the $R(H)$ curves can be indeed ascribed to commensurability effect between the porous structure of the Nb film and the vortex lattice. The distribution of the experimental points is consistent with the observation that a certain temperature dependence of the matching effect can be found for the case of short-range ordered templates [11]. We would also point out that the effect is observable in our sample only up to $H = H_1$, due to the very high value of the first matching field. In fact, to see a bump in the dR/dH curve at the second matching field $H_2 = 2H_1 = 2.32$ Tesla, from a linear

extrapolation of the $H_{c2\perp}$ curve, it follows that we should measure a $R(H)$ curve at $T = 1.73$ K, temperature which cannot be reached in our experimental setup.

All the field values reported above have been calculated assuming a square lattice. The measured field values do not match with the ones calculated if a triangular array for the pores is considered. In fact, at $T = 3.490$ K [see Fig. 3.4(a)] the structure in the dR/dH curve for a triangular lattice would have been observed at a field $2/\sqrt{3}$ times higher than $H_{0/3} = 0.126$ Tesla, where no peculiar feature has been detected. This supports our assumption of considering a square lattice of holes in our system.

In conclusion, matching effects have been reported for Nb thin film grown on porous silicon. Due to the extremely reduced values of the interpore distance the effect is present at fields values higher than 1 Tesla and down to reduced temperatures as low as $t \simeq 0.52$. The commensurability manifests both in the (H, T) phase diagram and in the $R(H)$ transitions. The latter in particular reveal the formation of fractional matching states. As it was argued in many works the vortex configuration at fractional matching fields are characterized by striking domain structure and associated grain boundaries [31, 32]. The presence of multiple degenerate states with domain formation at the fractional field, directly observed with scanning Hall probe microscopy [31], seems to be high probable in our films.

3.2 J_c enhancement due to antidots

If a transport current is applied to a homogeneous ideal type-II superconductor vortices start to move at relatively small critical current density, J_c , with an associated onset of dissipation. This evidence, which represents one of the main factors restricting the field of possible applications of superconducting materials, imposes the need of a J_c enhancement which can be obtained, for example, by forcing and optimizing the vortex confinement in these systems [33]. Vortex pinning has been largely investigated and it has been shown that artificially produced periodic arrays of dots [2] and antidots [1, 3–5, 11] can drastically increase the J_c of superconductors. As already pointed out at the beginning of this chapter, nanolithographic techniques have been used to obtain submicrometer sized regular vortex pinning arrays giving the first matching field H_1 of the order of mT. Moreover, in these systems matching effects detected by transport measurements have been observed only for temperatures very close to the superconducting transition temperature, T_c (at $t = T/T_c \approx 0.99$) [3, 12, 34–36]. An increase of H_1 has been successfully realized using self-assembled templates as substrates for Nb thin films. Since typical interpore distances were in these cases less than 100 nm, matching effects have been observed for field values approaching 1 Tesla [14, 15, 37].

Due to the extremely reduced values of the interpore distance, I have obtained high field vortex matching effects in perforated Nb thin films down to reduced temperature t as low as 0.33. Perforated Nb films, 25-nm thick, containing a square lattice of pores of diameter $\emptyset = 17$ nm and interpore distance $a = 50$ nm, have been obtained by electron beam lithography (EBL) and lift-off procedure. To allow transport measurements, by means of which matching phenomena have been observed in the $J_c(H)$ dependence, the samples were additionally patterned into bridges. The behavior of $J_c(H)$ as well as the maxima locations have been also found to be consistent with the ones calculated in the framework of time dependent Ginzburg-Landau model [38].

3.2.1 Sample fabrication

The samples have been realized at the University of Salerno and they have a bridge geometry consisting of two macroscopic continuous Nb banks contacting the [length(l) \times width(w) = $30 \times 20 \mu\text{m}^2$] nanoporous Nb film, as shown in the inset of Fig. 3.9(a).

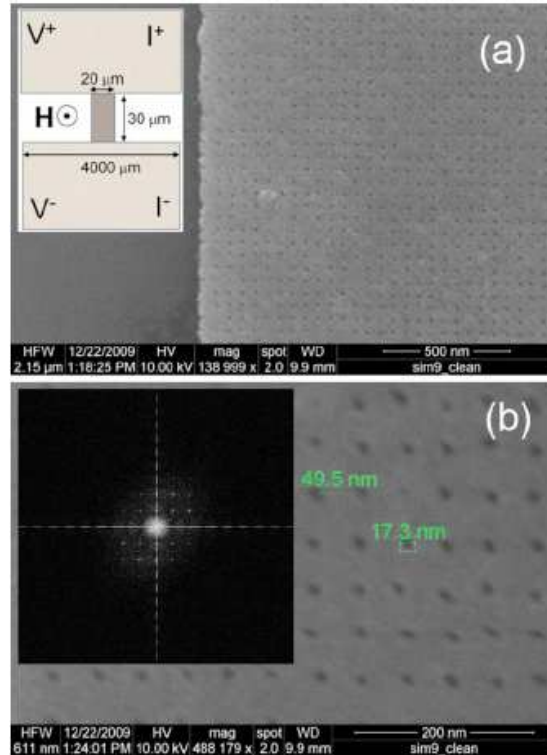


Figure 3.9: (a) FE-SEM images of a portion of the nanoporous Nb film. A sketch (not on scale) of the sample geometry is shown in the inset. (b) Zooming-in on individual pores with indication of inter-pore distance and pore diameter. In the inset we show the Fourier transform calculated on a $1 \times 1 \mu\text{m}^2$ area of the image in (a).

The banks have been realized using standard optical lithography, while the nanoporous film has been realized using EBL and a lift-off procedure¹. The EBL was performed in an FEI Inspect-F field emission scanning electron microscope (FE-SEM) equipped with a Raith Elphy Plus pattern generator. A 100-nm thick positive tone resist consisting of 2% polymethylmethacrylate (PMMA) 950000 molecular weight dissolved in anisole

¹For the realization of these samples I wish to thank Dr. G. Carapella.

was spin-coated onto a Si/SiO_2 substrate and baked at 180 °C in a convection oven for 30 min. The writing was carried out using a beam current of 10.5 pA, an acceleration voltage of 30 KV, a write-field of $100 \times 100 \mu\text{m}^2$ and an area step size of 49.5 nm. After exposure, PMMA development was carried out in a methyl isobutyl ketone and isopropyl alcohol solution (1-MIBK:3-IPA) for 30 s, followed by rinsing in IPA and deionized water. With the above exposure parameters, the clearance dose of our PMMA was $300 \mu\text{C}/\text{cm}^2$. To achieve the square lattice of antidots shown in Fig. 3.9(a), we used an area dose of about $100 \mu\text{C}/\text{cm}^2$. Such a dose is enough to create, after development, a resist mask consisting of a square lattice of circularly shaped indentations (i.e., regions where resist is thinned) with a diameter of about 50 nm and with a lattice constant equal to the used step size. A 3 min of light Ar sputter etching, at 4.1×10^{-3} mbar and a self bias of 400 V, fully cleans the indentations down to the substrate, but the PMMA region complementary to the indentations is not cleaned. The resulting mask consists of a square lattice of resist dots of about 17-nm diameter and a separation again equal to the used step size. On this mask we deposit a 25-nm thick and 99.98% pure Nb film by rf magnetron sputtering in a high-vacuum system with a base pressure of 6.9×10^{-8} mbar in 99.999 % pure Ar at 4.4×10^{-3} mbar with a rate of 2.2 nm/s. After lift-off in acetone, a Nb film with the square lattice of antidots shown in Fig. 3.9(a) is finally achieved. The square antidot lattice is quite regular, as more evident from the magnified FE-SEM image shown in Fig. 3.9(b) and from the Fourier transform calculated on a $1 \times 1 \mu\text{m}^2$ area of the image in Fig. 3.9(a) we show in the inset. The very small interpore distance of our porous Nb film, achieved here by means of a relatively simple sputter-etching-assisted EBL process, rivals the best results obtained using more complex techniques, such as the block-copolymer-assisted lithography [39], or the technique based on Anodized Alumina Oxide templates [14, 40, 41]. Also, our process allows to obtain a lattice of defects with a square symmetry, while using the other two processes lattices with (often only local) hexagonal symmetry are achieved.

3.2.2 Experimental results and discussion

The $V(I)$ characteristics have been measured in a ^4He cryostat using a standard dc four-probe technique at different temperatures with the magnetic field applied perpendicularly to the samples plane. During the measurement the temperature stabilization was around 1 mK. The values of J_c have been extracted using an electric field criterion of 1.67 V/m (corresponding to a voltage threshold of 50 μV in the samples) for all the temperatures and fields.

For the sample I report here (sample S1) the critical temperature $T_c = 6.9$ K was determined by transport measurements using a resistance criterion of 50% of the low temperature normal state resistance, R_N . The corresponding width of the resistive transition, defined as $\Delta T_c = T_c^{90\%R_N} - T_c^{10\%R_N}$, was $\Delta T_c \approx 100$ mK at zero field and with a bias current $I = 10$ μA ($J = 2 \times 10^7$ A/m²). The normal state resistivity, ρ_n , of this sample was equal to 46 $\mu\Omega\text{cm}$. To determine the superconducting coherence length $\xi_{0\parallel}$ we measured the (H, T) phase diagram. From the slope close to T_c of the $T_c(H)$ curve, shown in the inset of Fig. 3.10(a), and from the Eq. 3.1 we estimate $\xi_{0\parallel} = 8.2$ nm. This value is much smaller than the BCS coherence length of Nb, $\xi_0 = 39$ nm [23], so the sample is in the dirty limit regime with an electron mean free path $l = 1.38\xi_{0\parallel}^2/\xi_0 = 2.4$ nm. The Ginzburg-Landau parameter $\kappa = \lambda/\xi$ (λ is the magnetic field penetration depth) can be estimated, in the dirty limit, using the expression $\kappa = 0.72 \lambda_L/l \approx 12$, where $\lambda_L = 39$ nm is the London penetration depth of Nb [23]. This result implies that the investigated sample is a type-II superconductor. For the sake of comparison also a sample [S0 in Fig. 3.10(a)] with a 19-nm thick continuous Nb film has been measured. For this sample $T_c = 5.86$ K, $\Delta T_c = 40$ mK, $\rho_n = 34$ $\mu\Omega\text{cm}$, $\xi_{0\parallel} = 8.6$ nm, $l = 2.6$ nm, and $\kappa = 11$. All these values are very similar to the corresponding ones of the porous sample indicating that the procedure of fabrication of the antidots does not significantly alter the superconducting properties of the Nb film. The reduced values for T_c measured in both samples are mainly related to their small thickness even though they are a bit lower with respect to the ones previously

reported in the literature for high quality rf sputtered thin films of Nb [42].

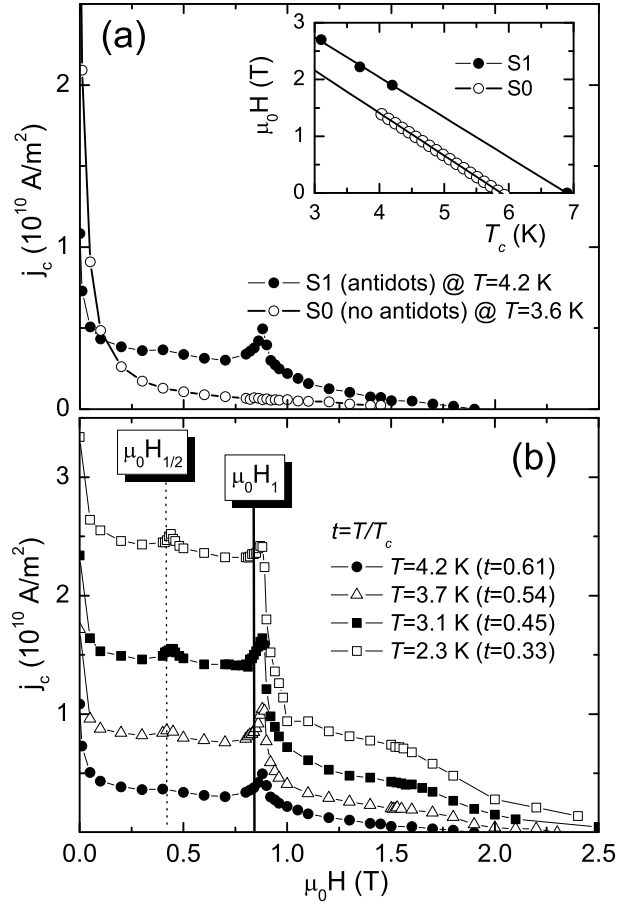


Figure 3.10: (a) Magnetic field dependence of the critical current density for the Nb film with antidots (S1, solid circles) and for the reference sample (S0, open circles) at two temperatures corresponding to same reduced temperature $t = 0.61$. In the inset are shown the $T_c(H)$ curves of both samples. (b) Critical current density versus the magnetic field measured at four different temperatures for the Nb film with antidots. Thick (dashed) vertical lines indicate integer (rational) theoretically expected matching fields.

In Fig. 3.10(a) we show the magnetic field dependence of the critical current density for the porous sample at $T = 4.2$ K and the reference Nb film taken at $T = 3.6$ K, which corresponds to the same reduced temperature $t = T/T_c = 0.61$. Comparing the two sets of data we see that, except at very low fields, the sample with holes has J_c values which are approximately two times larger than the corresponding values obtained on the virgin sample indicating that a stronger confinement of the vortex lattice has been

obtained in the porous sample. However, what is much more interesting is that the curve for the sample with holes exhibits a very pronounced maximum at 0.880 T. This value is very close to the expected first matching field $H_1 = 0.830$ T as estimated from the interpore spacing $a = 50$ nm, being a square porous array.

Fig. 3.10(b) shows the $J_c(H)$ dependence for the porous Nb film taken at four different temperatures, corresponding to a range from 0.61 to 0.33 for t . At $t = 0.33$ and $H = 0$ the measured $J_c \approx 4 \times 10^{10}$ A/m² is less than one order of magnitude smaller than the depairing current density J_{dp} whose expression [43] at zero magnetic field is given by

$$J_{dp}(t) = 7.84 \left(\frac{(k_B T_c)^3}{e^2 \hbar v_F (\rho_n l) \rho_n} \right)^{1/2} (1-t)^{3/2} \quad (3.4)$$

Using the above parameters for the Nb film with antidots, we estimate $J_{dp}(t=0.33) \approx 2.1 \times 10^{11}$ A/m². All the curves show a clear peak just above the expected first matching field followed by a strong decrease which becomes more pronounced at lower temperatures. Also, in the $J_c(H)$ curves a maximum appears at $H = 0.440$ T, just above the expected half-harmonic matching field $H_{1/2} = 0.415$ T, which becomes clearer and clearer as the temperature is lowered. Apart from this peak which is related to the very well-known *checkerboard* vortex arrangement appearing in a square array of antidots [44], the form of the curves strongly resembles those obtained on Nb thin films with a triangular array of pinning centers [11]. Except for $T = 4.2$ K where matching fields $H_m = mH_1$ with $m > 1$ are larger than the upper critical field, the lack of observation of higher order matching phenomena can be easily explained considering the value of the saturation number n_s , i.e., the maximum number of vortices which can fit into a pore of diameter \emptyset . If we consider its expression [28] $n_s = \frac{\emptyset}{4\xi_S(T)}$ where $\xi_{||}(T) = \xi_{0||}/\sqrt{1-T/T_c}$ we obtain for our sample at $T = 2.3$ K that n_s is less than one and this still holds if the high-field expression [45] $n_s \sim [\frac{\emptyset}{4\xi_S(T)}]^2$ is considered. Another estimation has been given (but for a triangular array of cylindrical

cavities) [46] according to which double occupancy of pinning sites is possible only if $\emptyset > 2[\xi_{\parallel}(T)d^2]^{1/3}$. In our case $2[\xi_{\parallel}(T)d^2]^{1/3} \approx 51$ nm and the above condition is not satisfied. So each hole can trap only one fluxon and multiquanta vortex lattice [1] is not allowed in our system.

In conclusion, we obtained by a simple sputter-etching-assisted EBL process a regular square array of nanometer-sized pinning centers on Nb thin films. The $J_c(H)$ values, measured by transport measurements on patterned samples, are found to be considerably larger than those measured on a Nb film without antidots at the same reduced temperature and exhibit pronounced maxima just above the expected $H_1 = 0.830$ T and $H_{1/2} = 0.415$ T matching fields, down to $T = 2.3$ K ($t = 0.33$). Our experiment shows an increase of the critical current density at high fields and far from the superconducting transition temperature, a result promising in view of practical high-field applications of thin film superconductors.

Bibliography

- [1] V.V. Moshchalkov, M. Baert, V.V. Metlushko, E. Rosseel, M.J. Van Bael, K. Temst, and Y. Bruynseraede, *Phys. Rev. B* **57**, 3615 (1998).
- [2] A. Hoffmann, P. Prieto, and I.K. Schuller, *Phys. Rev. B* **61**, 6958 (2000).
- [3] A.T. Fiory, A.F. Hebard, and S. Somekh, *Appl. Phys. Lett.* **32**, 73 (1978).
- [4] A.N. Lykov, *Solid St. Commun.* **86**, 531 (1993).
- [5] A. Castellanos, R. Wördenweber, G. Ockenfuss, A.v.d. Hart, and K. Keck, *Appl. Phys. Lett.* **71**, 7 (1997).
- [6] J.I. Martín, M. Vélez, J. Nogués, and I.K. Schuller, *Phys. Rev. Lett.* **79**, 1929 (1997).
- [7] M.J. Van Bael, K. Temst, V.V. Moshchalkov, and Y. Bruynseraede, *Phys. Rev. B* **59**, 24674 (1999).
- [8] M. Vélez, J.I. Martín, J.E. Villegas, A. Hoffmann, E.M. González, J.L. Vincent, and I.K. Schuller, *J. Magn. Magn. Mater.* **320**, 2547 (2008).
- [9] A.V. Silhanek, L. Van Look, R. Jonckheere, B.Y. Zhu, S. Raedts, and V.V. Moshchalkov, *Phys. Rev. B* **72**, 014507 (2005).
- [10] W.A. Little and R.D. Parks, *Phys. Rev. Lett.* **9**, 9 (1962).
- [11] J. Eisenmenger, M. Oettinger, C. Pfahler, A. Plettl, P. Walther, and P. Ziemann, *Phys. Rev. B* **75**, 144514 (2007).

- [12] M. Kemmler, C. Gürlich, A. Sterk, H. Pöhler, M. Neuhaus, M. Siegel, R. Kleiner, and D. Koelle, *Phys. Rev. Lett.* **97**, 147003 (2006).
- [13] J. Van de Vondel, C.C. de Souza Silva, B.Y. Zhu, M. Morelle and V.V. Moshchalkov, *Phys. Rev. Lett.*, **94**, 057003 (2005).
- [14] W. Vinckx, J. Vanacken, V.V. Moshchalkov, S. Mátéfi-Tempfli, M. Mátéfi-Tempfli, S. Michotte, L. Piraux, and X. Ye, *Physica C* **459**, 5 (2007).
- [15] M. Trezza, S.L. Prischepa, C. Cirillo, R. Fittipaldi, M. Sarno, D. Sannino, P. Ciambelli, M.B.S. Hesselberth, S.K. Lazarouk, A.V. Dolbik, V.E. Borisenko, and C. Attanasio, *J. Appl. Phys.* **104**, 083917 (2008).
- [16] O. Bisi, S. Ossicini, and L. Pavesi, *Surf. Sci. Rep.* **38**, 1 (2000).
- [17] R.T. Collins, P.M. Fauchet, and M.A. Tischler, *Phys. Today* **50**, 24 (1997).
- [18] H. Cheraga, S. Belhousse, and N. Gabouze, *Appl. Surf. Sci.* **238**, 495 (2004).
- [19] V. Lysenko, S. Perichon, B. Remaki, B. Champagnon, and D. Barbier, *J. Appl. Phys.* **86**, 6841 (1999).
- [20] S. Mátéfi-Tempfli, M. Mátéfi-Tempfli, and L. Piraux, *Thin Solid Films* **516**, 3735 (2008).
- [21] S.K. Lazarouk, A.V. Dolbik, V.A. Labunov, and V.E. Borisenko, *Physics, Chemistry and Application of Nanostructures*, (World Scientific) 2007, p. 223.
- [22] M. Tinkham, *Introduction to Superconductivity*, (McGraw-Hill Inc) 1996.
- [23] W. Buckel, *Supraleitung*, 3rd edition (Physik-Verlag, Weinheim) 1984.
- [24] V.V. Schmidt, *The Physics of Superconductors*, edited by P. Müller and A.V. Ustinov (Springer, Berlin-Heidelberg) 1997.
- [25] U. Welp, Z.L. Xiao, J.S. Jiang, V.K. Vlasko-Vlasov, S.D. Bader, G.W. Crabtree, J. Liang, H. Chik, and J.M. Xu, *Phys. Rev. B* **66**, 212507 (2002).

-
- [26] W. Vinckx, J. Vanacken, V.V. Moshchalkov, S. Mátéfi-Tempfli, M. Mátéfi-Tempfli, S. Michotte, and L. Piraux, *Eur. Phys. J. B* **53**, 199 (2006).
- [27] E.H. Brandt, *Phys. Lett.* **77A**, 484 (1980).
- [28] G.S. Mkrtchyan and V.V. Shmidt, *Zh. Eksp. Teor. Fiz.* **61**, 367 (1971). [*Sov. Phys. JETP* **34**, 195 (1972)].
- [29] U. Patel, Z.L. Xiao, J. Hua, T. Xu, D. Rosenmann, V. Novosad, J. Pearson, U. Welp, W.K. Kwok, and G.B. Crabtree, *Phys. Rev. B* **76**, 020508(R) (2007).
- [30] M. Baert, V.V. Metlushko, R. Jonckheere, V.V. Moshchalkov, and Y. Bruynseraede, *Europhys. Lett.* **29(2)**, 157 (1995).
- [31] S.B. Field, S.S. James, J. Barentine, V. Metlushko, G. Crabtree, H. Shtrikman, B. Ilic, and S.R.J. Brueck, *Phys. Rev. Lett.* **88**, 6 (2002).
- [32] A.N. Grigorenko, S.J. Bending, M.J. Van Bael, M. Lange, V.V. Moshchalkov, H. Fangohr, and P.A.J. de Groot, *Phys. Rev. Lett.* **90**, 23 (2003).
- [33] V. Misko, S. Savel'ev, and F. Nori, *Phys. Rev. Lett.* **95**, 177007 (2005).
- [34] L. Horng, J.C. Wu, T.C. Wu, and S.F. Lee, *J. Appl. Phys.* **91**, 8510 (2002).
- [35] L. Van Look, B.Y. Zhu, R. Jonckheere, B.R. Zhao, Z.X. Zhao, and V.V. Moshchalkov, *Phys. Rev. B* **66**, 214511 (2002).
- [36] A.D. Thakur, S. Ooi, S.P. Chockalingam, J. Jesudasan, P. Raychaudhuri, and K. Hirata, *Appl. Phys. Lett.* **94**, 262501 (2007).
- [37] M. Trezza, C. Cirillo, S.L. Prischepa, and C. Attanasio, *Europhys. Lett.* **88**, 57006 (2009).
- [38] P. Sabatino, C. Cirillo, G. Carapella, M. Trezza, and C. Attanasio, *J. Appl. Phys.* **108**, 053906 (2010).

-
- [39] A.M. Popa, P. Niedermann, H. Heinzelmann, J.A. Hubbell, and R. Pugin, *Nanotechnology* **20**, 485303 (2009).
- [40] X. Hallet, M. Mátéfi-Tempfli, S. Michotte, L. Piraux, J. Vanacken, V.V. Moshchalkov, and S. Mátéfi-Tempfli, *Appl. Phys. Lett.* **95**, 252503 (2009).
- [41] X. Hallet, M. Mátéfi-Tempfli, S. Michotte, L. Piraux, J. Vanacken, V.V. Moshchalkov, and S. Mátéfi-Tempfli, *Small* **5**, 2413 (2009).
- [42] S.A. Wolf, J.J. Kennedy, and M. Niesenoff, *J. Vac. Sci. Technol.* **13**, 145 (1976).
- [43] M.Y. Kupriyanov and V.F. Lukichev, *Fiz. Nizk. Temp.* **6**, 445 (1980) [*Sov. J. Low Temp. Phys.* **6**, 210 (1980)].
- [44] A.N. Grigorenko, G.D. Howells, S.J. Bending, J. Bekaert, M.J. Van Bael, L. Van Look, V.V. Moshchalkov, Y. Bruynseraede, G. Borghs, I.I. Kaya, and R.A. Stradling, *Phys. Rev. B* **63**, 052504 (2001).
- [45] M.M. Doria, S.C.B. de Andrade, and E. Sardella, *Physica C* **341**, 1199 (2000).
- [46] A.I. Buzdin, *Phys. Rev. B* **47**, 11416 (1993).

Chapter 4

Vortex pinning with artificial magnetic nanostructures

Pinning interactions between superconducting vortices in Nb ultrathin films and magnetic Ni nanowires were studied to clarify the nature of pinning mechanisms. Superconducting properties have been investigated by transport measurements in the presence of magnetic fields applied perpendicularly to the samples surface. As a consequence of the high density of the pore network, the (H, T) phase diagram presents a deviation from the classic linear dependence. This effect appears at the first matching field H_1 and its multiple values.

4.1 Introduction

As widely discussed in chapter 1, vortex dynamics is an active research field due to the richness and variety of the physics it presents. The superconducting material, defect structures, temperature and applied magnetic field are the main factors that strongly affect the behavior of the vortices and give rise to complex phase diagrams [1, 2]. More recently, the use of ferromagnetic materials as pinning centers has also attracted much attention [3–8]. The way has been paved by Otani and coworkers [9]

who used a GdCo dots array on top of a Nb film in which the magnetization of the dots was in-plane (i.e., parallel to the superconducting film). The magnetic fields of the magnetic dots were acting as pinning centers for the vortices. Since then, many experimental [8, 10–14] and theoretical [15, 16] works have been performed. Notably, Hoffmann et al. [10] compared experimentally the vortex pinning in superconducting films deposited on top of square arrays of magnetic and non magnetic dots of different sizes. For equal size of the dots, the number and the amplitude of the matching effects were more pronounced with ferromagnetic dots. The enhancement of the superconducting properties due to the field of the ferromagnetic dots rather than to a local thickness modulation was thus proved. In addition, large enough dot magnetization may create vortices in the superconducting film [17]. This resulted not only in the observation of clear pinning effects when the vortex lattice interacts with arrays of magnetic dots [18–20], but also produced a rich behavior of the vortex dynamics which can be tuned by modifying the properties of the pinning array [5]. It should be pointed out that, in order to understand vortex pinning with artificial arrays, it is necessary to consider the role played by individual dot properties such as size and magnetic state. In particular, the ability to tune *in situ* the pinning potentials through changes of the magnetic configuration presents a unique opportunity provided by magnetic pinning centers. However, up to now the observation of these effects were restricted to relatively low magnetic fields (due to relatively large geometrical pinning lattice parameters), to temperatures very close to the superconducting transition and to low- T_c superconductors. This is because lithographic techniques are not able to produce, in an efficient manner, large area pinning lattices with a small period. Alternative methods to the lithographic patterning using templates of self-assembled nanostructures [7] and of nanoporous materials are promising approaches for applications.

In this chapter, 500 nm thick nanoporous alumina templates have been used to produce an antidots lattice in a thin superconducting film. This alumina membrane, with periodic triangular lattice, has been utilized to grow electrochemically in the pores an array of long ferromagnetic nanowires (Ni) arranged parallel to each other

and with small interdistance. Then, a thin insulating layer of Al_2O_3 (20 nm thick) has been sputtered on the top of the filled template. Finally 32 nm (and 40 nm) thick Nb film has been deposited on the surface. The porous alumina membranes used in this study have diameter $\varnothing = 60$ nm and interpore spacing $a = 120$ nm. Superconducting properties have been investigated in these structures by transport measurements in the presence of magnetic fields applied perpendicularly to the samples surface. As a consequence of the high density of the pore network, the (H, T) phase diagram presents a deviation from the classic linear dependence. This effect appears at the first matching field H_1 and its multiple values.

4.2 Sample fabrication

Porous alumina membranes have been fabricated at the University of Minsk (Belarus). These templates have been prepared by using a two-step anodization procedure on a Si/SiO_x/Ta substrate as shown in Fig. 4.1. First, a 60 nm thick Ta film was deposited on a thermally oxidized 76 mm Si wafer by e-beam evaporation with the rate (1.0 ± 0.2) nm/s and with a base pressure of 1.3×10^{-5} mbar. The substrates have been heated up to 250°C, then they have been cooled down to 150°C and 1500 nm Al film was subsequently evaporated on the top of the Ta layer with a base pressure of 1.4×10^{-6} mbar and deposition rate of (5.0 ± 0.5) nm/s [see Fig. 4.1(a)]. The deposition rates were controlled by a quartz crystal monitor. Afterwards by using standard photolithography an open window of 1 cm² area has been realized on the top surface of Al film. The remaining part of the surface was covered by positive photoresist. The anodization has been performed in a 0.3 M H₂C₂O₄ solution at 40 V and 12°C. The first anodization process was performed for 30 min [Fig. 4.1(b)]. Then, the oxide was dissolved in a mixture solution of 1.8 wt % H₂CrO₄ and 7.4 wt % H₃PO₄ at 65°C. After complete dissolution of the oxide structure [Fig. 4.1(c)], the surface of the Al

film keeps the regular hexagonal texture of the self-organized pore tips, which act as a self-assembled mask for a second anodization process.

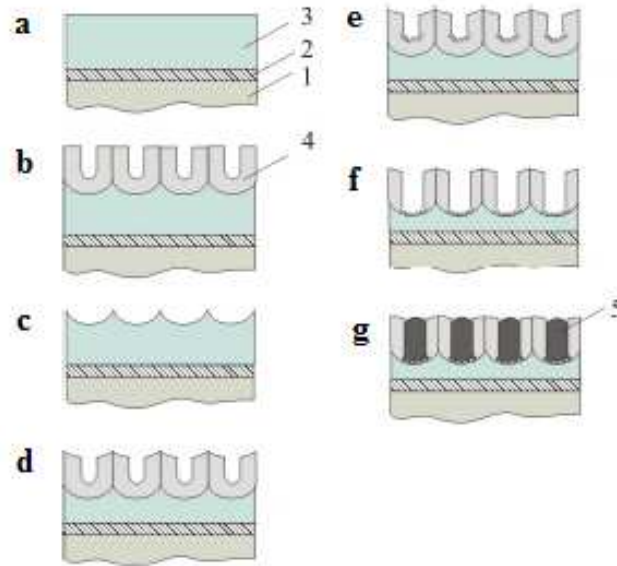


Figure 4.1: A schematic representation of the different steps of the anodization process of Al and of the growth of Ni in porous AAO membrane. The number 1 indicates the Si/SiO_x wafer, 2 the Ta film, 3 the Al film, 4 the Al₂O₃ membrane and 5 the Ni nanowires.

The second anodization process has been performed for 20 min under the same condition [Fig. 4.1(d)]. After a second anodization, a relatively ordered nanopores array is obtained with straight pores from top to bottom having a thickness of about 300-350 nm and a pore diameter, \varnothing , of 35-40 nm. At the end of the second anodization process, the voltage was reduced stepwise from 40 to 10 V with rate 1.0 V/s [Fig. 4.1(e)], which corresponds to the barrier oxide thickness less than 10 nm. Further reduction of the anodization potential may cause the oxide structure to completely peel off of the metal substrate during the deposition. The residual barrier layer is thinned by chemical pore widening (\varnothing increasing up to 50-60 nm) and has been etched in 5% H₃PO₄ at 20°C for 20 min [Fig. 4.1(f)]. The thinning of the barrier layer leads to a considerable decrease in the potential barrier for the electrons to tunnel through the barrier layer, when the metal is deposited at the pore tips. Thus, lower voltages are necessary for the pores

electrochemical filling and the porous alumina oxide can be maintained on the aluminum film. Electrochemical deposition of nickel has been performed in two-electrode cell in controlled potential mode at room temperature with use potentiostat P-5827M by applying a constant voltage -2.2 V for a period of 7 minutes [Fig. 4.1(g)]. The graphite plate has been used as an auxiliary electrode. The geometric area exposed for coating was 1 cm^2 on one side. The composition of the plating bath was as follows: 200g/l $\text{NiSO}_4 \times 7\text{H}_2\text{O}$, 40 g/l $\text{NiCl}_2 \times 6\text{H}_2\text{O}$, 30g/l H_3BO_3 and 70g/l Na_2SO_4 . The pH of such electrolyte was 5.2 and the deposition has been carried out at room temperature with continuous stirring. The topography of the obtained Ni nanopillars has been studied by AFM Nanotop NT-206. Before the analysis the amorphous alumina has been chemically removed in a hot phosphoric-chromic mixture and in concentrated hydrochloric acid. The obtained AFM image of a part of the template surface $4 \times 4\ \mu\text{m}^2$ square is shown in Fig. 4.2.

A thin insulating layer of Al_2O_3 (20 nm thick) has been grown, at the University of Salerno, depositing Al on the top of the porous alumina membranes in an UHV dc diode magnetron sputtering system with a base pressure in the low 10^{-8} mbar regime and sputtering Argon pressure of 5.0×10^{-3} mbar. The Al films have been deposited at typical rates of 0.014 nm/s, controlled by a quartz crystal monitor. The insulating layers have been realized in two steps and between the two consecutive Al depositions the samples have been exposed to the air to obtain the formation of a reliable oxide layer. Moreover, in order to optimize the process, the membranes have also been heated.

Finally, Nb thin films have been grown on the top of the porous membranes in the same sputtering system using a sputtering Argon pressure of 3.5×10^{-3} mbar. In order to reduce the possible contamination of the porous templates, the membranes have been heated at 120°C for one hour in the UHV chamber. The deposition was then realized at room temperature after the cool-off of the substrates. The Nb films have been deposited at typical rates of 0.33 nm/s, controlled by a quartz crystal monitor calibrated by low-angle X-ray reflectivity measurements. Since the effect of

the periodic template would be reduced when the film thickness, d_{Nb} , exceeds the pore diameter, \emptyset , [21] the Nb thickness was chosen to be not larger than 40 nm.

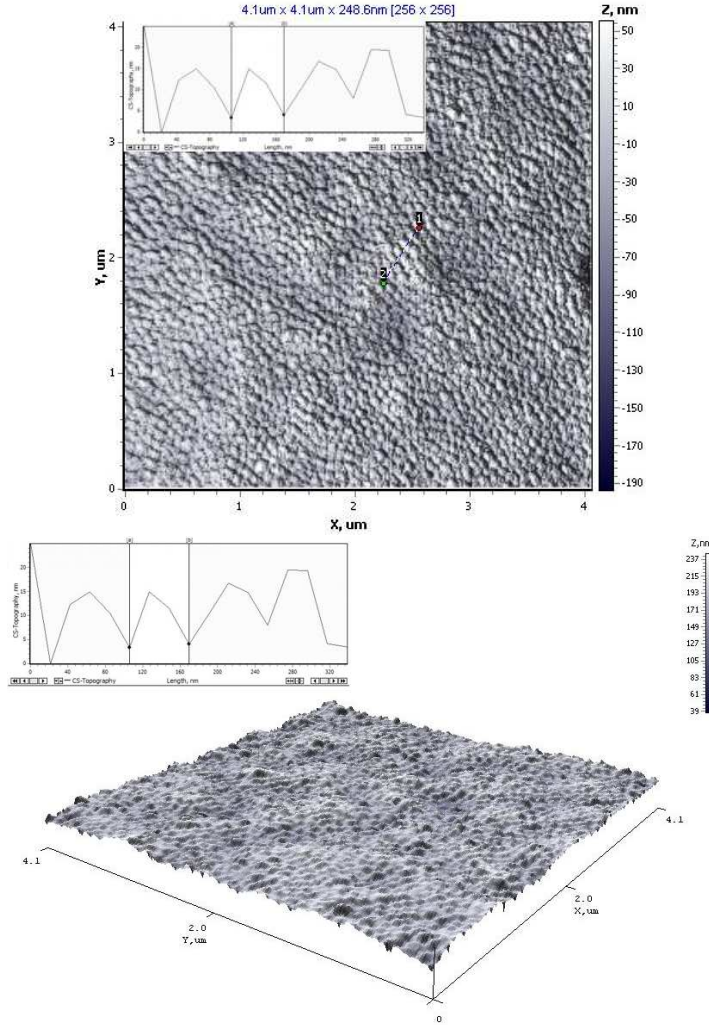


Figure 4.2: AFM image of the surface of porous AAO with Ni grown inside pores. In the inset is shown the profile of the Ni nanopillars.

In the same deposition run, i.e. under identical deposition conditions, a reference Nb film has been deposited on a non-porous Si substrate on which, before, an insulating layer of Al_2O_3 (20 nm thick) had been grown.

In this way, the samples used for this study are ferromagnet/insulator/superconductor (F/I/S) trilayers, the ferromagnet is separated from the superconductor by a thin in-

insulating layer so that only the electromagnetic interaction is involved. A schematic representation showing the deposition of a 20 nm thick Al_2O_3 insulating layer and a 40 nm thick Nb film on the extremities of an array of Ni nanowires embedded in a nanoporous alumina template, is reported in figure 4.3.

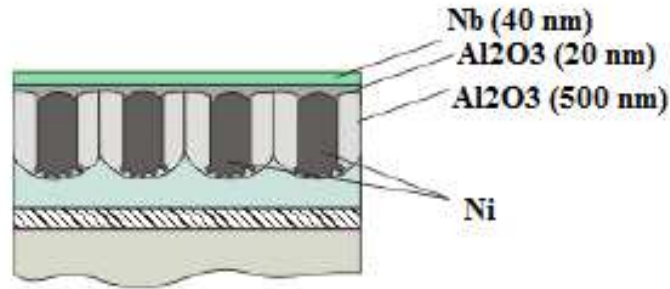


Figure 4.3: A schematic representation showing the deposition of a 20 nm thick Al_2O_3 insulating layer and a 40 nm thick Nb film on the extremities of an array of Ni nanowires embedded in a nanoporous alumina template.

4.3 Experimental results and discussion

In an uniform superconducting material, the minimum energy for a vortex lattice created by a magnetic field H corresponds to a triangular lattice in which the distance among the vortices is given by [22]

$$a_0 = \left(\frac{2\Phi_0}{\sqrt{3}H} \right)^{1/2} \quad (4.1)$$

where Φ_0 is the quantum of flux. However, in the presence of a periodic array of defects, the vortex lattice can adopt different highly ordered configurations [5]. As widely discussed in the first chapter, this results in an enhanced pinning between the vortex lattice and the array of defects when a matching condition is fulfilled, giving

rise to pronounced minima in the dissipation that have been observed in different symmetry regular arrays of magnetic pinning centers [18–20].

Our porous substrates have pores with diameter $\varnothing = 60$ nm and interpore spacing $a = 120$ nm. For this lattice, if the formula 4.1 for the triangular array is used, the expected first matching field is $H_1 = 166$ mTesla.

The superconducting properties were resistively measured using a standard dc four-probe technique in a ^4He cryostat that allows to control the temperature with stability of 1 mK. The magnetic field H was always applied perpendicularly to the plane of the film. The critical temperatures T_c , estimated at the midpoint of the $R(T)$ transition curves, and other parameters of two investigated samples are listed in Table 4.1. For the sake of clarity the samples will be named using the acronym AON-Nb followed by a number for the Nb thickness. For example, AON-Nb32 is the Nb film 32 nm thick, grown on the porous alumina template with an array of Ni nanowires. AO-Nb40 indicates a Nb film, 40 nm thick, deposited on a non porous substrate.

Sample	$a(\text{nm})$	$d_{\text{Nb}}(\text{nm})$	$H_1(\text{mT})$	$T_c(\text{K})$
AON-Nb32	120	32	166	6.25
AON-Nb40	120	40	166	5.65
AO-Nb40	–	40	–	5.80

Table 4.1: *Characteristics of porous alumina templates, with magnetic Ni nanowires, and properties of Nb films deposited on such substrates. a indicates the interpore spacing, d_{Nb} the Nb thickness, H_1 the first matching field, T_c the critical temperature. The pore diameter \varnothing is equal to 60 nm for the two porous samples.*

In Fig. 4.4 is reported the superconducting phase diagram, obtained measuring $R(T)$ transitions at fixed magnetic field, for a 40 nm thick Nb film sputtered on an array of Ni nanowires (sample AON-Nb40, blue line) and the one for a Nb film of the same thickness deposited on a non porous alumina template (AO-Nb40, green line).

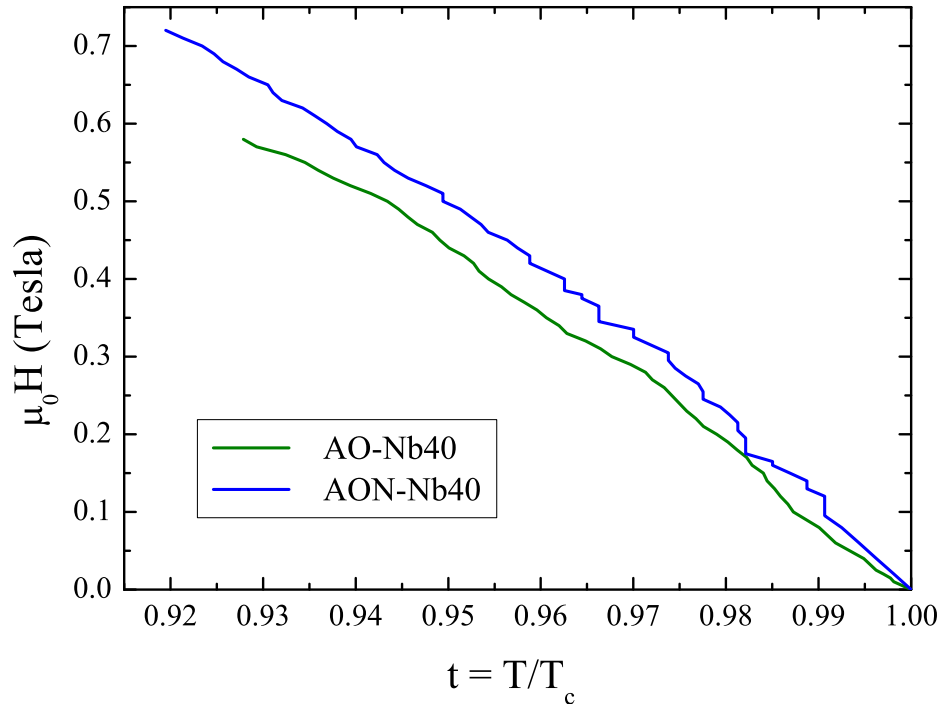


Figure 4.4: *Perpendicular upper critical field $H_{c2\perp}$ vs reduced temperature of the sample AON-Nb40 (blue line) and of the sample AO-Nb40 (green line).*

At first glance it is clearly visible that the introduction of the porous array strongly modifies the behavior of the perpendicular critical field. $H_{c2\perp}(T)$ is, in fact, characterized by a strong nonlinear temperature dependence near T_c , demonstrating the strong influence of the magnetic state of the pins on the superconducting properties of the Nb film. As expected, the $H_{c2\perp}(T)$ behavior of the sample AO-Nb40 is smoother, over the all temperature range, than the one of the sample AON-Nb40 grown on a periodic array of magnetic nanowires. Superconductivity takes place below the corresponding curves. The critical magnetic field is strongly enhanced for the porous film, which means that the sample can be used at much higher fields before vortices start to move causing dissipation [7].

Figure 4.5 shows the superconducting (H, T) phase diagram for the sample AON-Nb40 obtained inverting the axes with respect to figure 4.4.

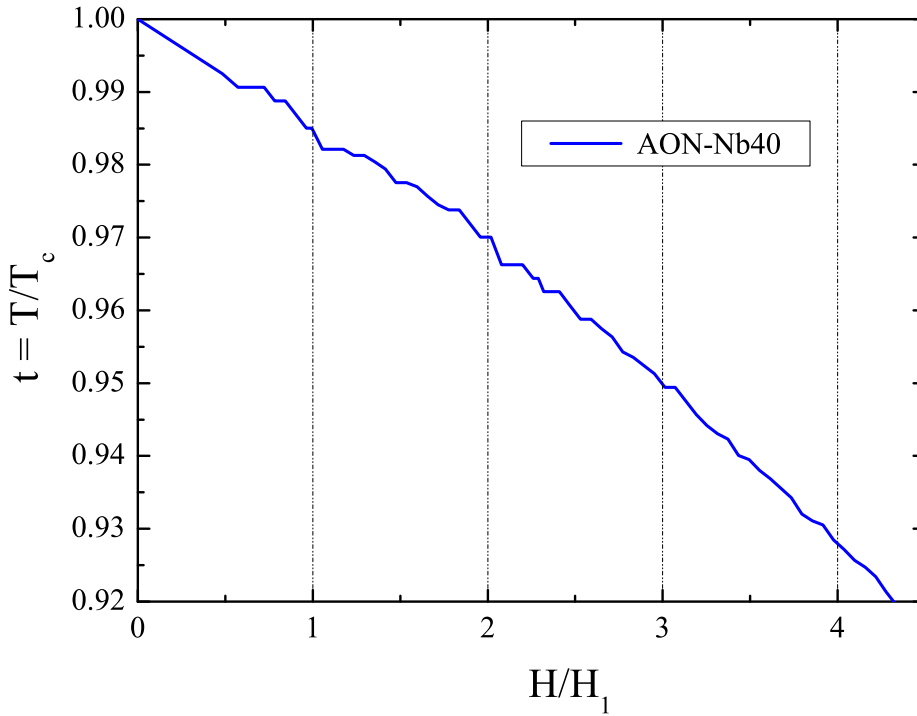


Figure 4.5: Superconducting phase diagram of the sample AON-Nb40. The magnetic field is normalized to the first matching field while t is the reduced temperature. The dotted lines correspond to the different matching field orders achieved with the interpore spacing $a = 120$ nm.

A more careful inspection of the (H, T) phase diagram of the sample AON-Nb40 shows that in the curve some vertical features are present at specific values of the magnetic field. This effect is ascribed to a pinning enhancement when the period of the vortex structure is commensurate with the period of the magnetic pins. This unusual behavior of T_c in the (H, T) diagram appears indeed at values of the magnetic fields H_n when the magnetic flux threading each unit cell is equal to the flux quantum, Φ_0 , or to multiple values of Φ_0 . In Fig. 4.5 the dotted lines correspond to the matching fields of different orders, as calculated assuming an interpore spacing $a = 120$ nm, through the formula 4.1. In correspondence to these vertical features the critical temperature becomes higher for these applied magnetic fields; they have a period coinciding with the first matching field H_1 and are due to fluxoid quantization effects [12]. This confirms

that superconductivity nucleates in multiply connected regions of the film as typically observed in superconducting wire networks [12, 23].

The same behavior is present in the (H, T) phase diagram of the 32 nm thick Nb film sputtered on an array of Ni nanowires (Fig. 4.6). We can still observe a strong nonlinear temperature dependence of $H_{c2\perp}(T)$ near T_c and an enhancement of the critical temperature, as indicated by the vertical features in the diagram, when the period of the vortex structure is commensurate with the period of the Ni pins. The dotted lines emphasize the matching fields of different order.

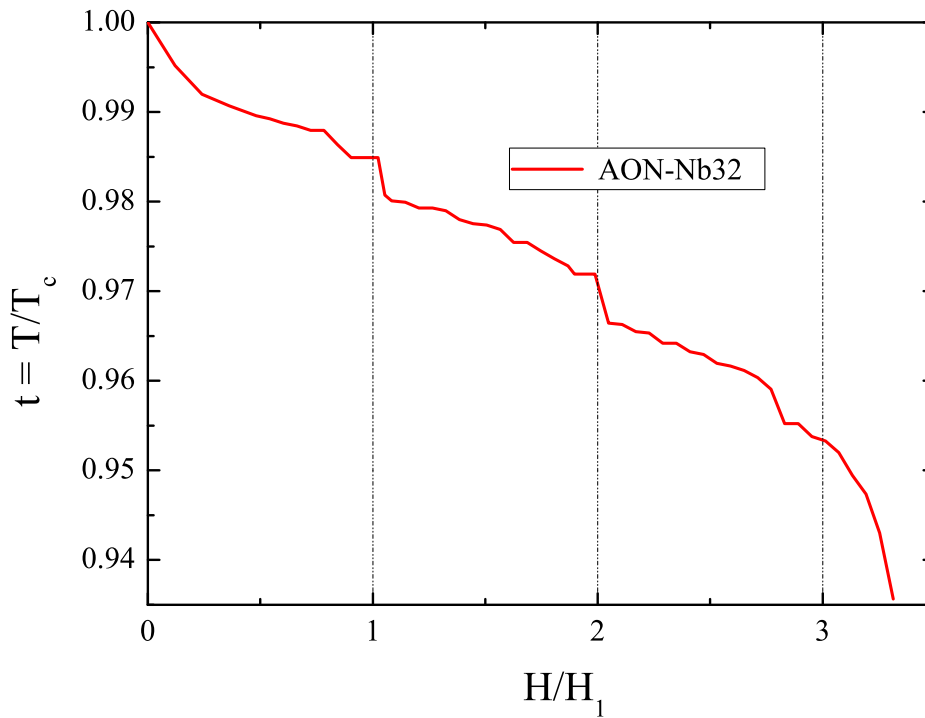


Figure 4.6: *Superconducting phase diagram of the sample AON-Nb32. The magnetic field is normalized to the first matching field while t is the reduced temperature. The dotted lines correspond to the different matching field orders achieved with the interpore spacing $a = 120$ nm.*

By comparing the two curves above, it is worth underlining that the behavior of the sample AON-Nb40 is more rugged than the one of the sample AON-Nb32. In fact, in the phase diagram (H, T) of the sample AON-Nb40 additional vertical features are visible at different magnetic fields. However, these field values do not correspond to any commensurate vortex configuration. We believe that such response is due to the fact that the effect of the periodic template could be reduced when the film thickness, d_{Nb} , is comparable with the pore diameter \emptyset .

In conclusion, we used nanoporous alumina templates to grow dense arrays of ferromagnetic nanowires serving as magnetic pinning centers in nearby Nb thin films. Matching effects have been observed up to the 3rd matching field. Such matching fields are typically higher than the ones previously reported using lithographically defined magnetic pinning patterns. The magnetic interaction between the nanowires array and the thin superconducting film has been undoubtedly recognized through an appreciable enhancement of the critical temperature when the period of the vortex structure is commensurate with the period of the Ni pins.

Bibliography

- [1] A.M. Campbell and J.E. Evetts, *Adv. Phys.* **21**, 199 (1972).
- [2] G. Blatter, M.V. Feigel'man, V.B. Geshkenbein, A.I. Larkin, and V.M. Vinokur, *Rev. Mod. Phys.* **66**, 1125 (1994).
- [3] M.J. Van Bael, K. Temst, V.V. Moshchalkov, and Y. Bruynseraede, *Phys. Rev. B* **59**, 14674 (1999).
- [4] J.I. Martín, M. Vélez, A. Hoffmann, I.K. Schuller and J.L. Vicent, *Phys. Rev. B* **62**, 9110 (2000).
- [5] M. Vélez, J.I. Martín, J.E. Villegas, A. Hoffmann, E.M. Gonzáles, J.L. Vincent and I.K. Schuller, *J. Magn. Magn. Mater.* **320**, 2547 (2008).
- [6] J.E. Villegas, E.M. Gonzáles, Z. Sefrioui, J. Santamaria, and J.L. Vincent, *Phys. Rev. B* **72**, 174512 (2005).
- [7] X. Hallet, M. Mátéfi-Tempfli, S. Mátéfi-Tempfli, S. Michotte, L. Piraux, J. Vanacken, and V.V. Moshchalkov, *Appl. Phys. Lett.* **95**, 252503 (2009).
- [8] W. Gillijns, A.V. Silhanek, and V.V. Moshchalkov, *Phys. Rev. B* **74**, 220509 (2006).
- [9] Y. Otani, B. Pannetier, J. Nozières, and D. Givord, *J. Magn. Magn. Mater.* **126**, 622 (1993).
- [10] A. Hoffmann, P. Prieto, and I.K. Schuller, *Phys. Rev. B* **61**, 6958 (2000).

-
- [11] A.V. Silhanek, W. Gillijns, M.V. Milosevic, A. Volodin, V.V. Moshchalkov, and F.M. Peeters, *Phys. Rev. B* **76**, 100502 (2007).
- [12] M. Lange, M.J. Van Bael, Y. Bruynseraede, and V.V. Moshchalkov, *Phys. Rev. Lett.* **90**, 197006 (2003).
- [13] Z. Yang, M. Lange, A. Volodin, R. Szymczak, and V.V. Moshchalkov, *Nat. Mater.* **3**, 793 (2004).
- [14] S. Haindl, M. Weisheit, T. Thersleff, L. Schultz, and B. Holzapfel, *Supercond. Sci. Technol.* **21**, 045017 (2008).
- [15] M.V. Milosevic, S.V. Yampolskii, and F.M. Peeters, *Phys. Rev. B* **66**, 174519 (2002).
- [16] I.K. Marmorkos, A. Matulis, and F.M. Peeters, *Phys. Rev. B* **53**, 2677 (1996).
- [17] I.F. Lyuksyutov and V.I. Pokrovsky, *Phys. Rev. Lett.* **81**, 2344 (1998).
- [18] J.I. Martín, M. Vélez, J. Nogués, and I.K. Schuller, *Phys. Rev. Lett.* **79**, 1929 (1997).
- [19] D.J. Morgan and J.B. Ketterson, *Phys. Rev. Lett.* **80**, 3614 (1998).
- [20] Y. Jaccard, J.I. Martín, M.C. Cyrille, M. Vélez, J.L. Vicent, and I.K. Schuller, *Phys. Rev. B* **58**, 8232 (1998).
- [21] M. Trezza, S.L. Prischepa, C. Cirillo, R. Fittipaldi, M. Sarno, D. Sannino, P. Ciambelli, M.B.S. Hesselberth, S.K. Lazarouk, A.V. Dolbik, V.E. Borisenko, and C. Attanasio, *J. Appl. Phys.* **104**, 083917 (2008).
- [22] M. Tinkham, *Introduction to Superconductivity*, McGraw-Hill Inc. (1996).
- [23] B. Pannetier, J. Chaussy, R. Rammal, and J.C. Villegier, *Phys. Rev. Lett.* **53**, 1845 (1984).

Chapter 5

1D superconductivity in porous Nb ultrathin films

In this chapter, I report on the measurements of the transport properties of superconducting Nb ultrathin bridges grown by UHV magnetron sputtering on porous Si substrates. The films are about 10 nm thick and inherit from the substrate a structure made of holes with diameter of 10 nm and interpore spacing in the range 20-40 nm. Due to their reduced dimensions, they are sensitive to thermal fluctuations typical of 1D superconductors and exhibit a nonzero resistance below the superconducting transition temperature, T_c . Clear hysteresis and finite jumps in the I - V curves are also observed.

5.1 Introduction

With the rapid development of nanotechnology, superconductivity in one dimensional (1D) nanowires has attracted considerable attention in the last two decades [1–9]. These systems are very interesting because they provide unique experimental test-beds to investigate and discover novel superconducting phenomena in confined geometries. This great interest rises since the superconducting nanowires involve such fundamental

phenomena as macroscopic quantum tunneling, quantum phase transitions and environmental effects [2, 10–12], and in addition they can find applications in classical and possibly quantum information-processing devices. New developments in this way lead to the concept of a quantum computation, in which electronic devices, carrying bits of information, can exist in a quantum superposition of macroscopically distinct states and therefore can act as quantum bits (qubits) [13]. The central challenge in the study of thin superconducting wires is to understand how the superconductivity is affected when approaching the 1D limit. Continual advances in the fabrication techniques have allowed researchers to create wires of ever shrinking size, resulting in an increasing number of observed effects that shed light on this basic question. Earlier studies have predicted that, when the wire width is comparable with its superconducting coherence length $\xi(T)$, intrinsic thermal [4, 14] and quantum [5, 11, 15] fluctuations play an increasingly important role, causing the wires to remain resistive much below the superconducting transition temperature T_c with phase slip processes responsible for this phenomenon. At high temperatures (but below T_c) this resistance is caused by thermally activated phase slips (TAPS), in which the system makes a transition across a potential barrier between two different metastable states. At sufficiently low temperatures the general expectation is that the system would tunnel through the barrier between two metastable states, constituting a quantum phase slip event (QPS).

Recently a radically different approach to nanostructures fabrication based on self-assembled growth, such as chemically anisotropic etching of single crystals, has attracted much attention also in the superconducting nanowire field. These processes are useful for generating low-cost simple patterns of nanostructures in a single step, assuring a high reproducibility as well [3, 16, 17].

In this chapter I present experimental results obtained on superconducting Nb ultrathin films grown on porous Si substrates. The films are 9-12 nm thick and inherit from the substrate the structure made of pores with 10 nm-diameter and spacing between holes from 20 to 40 nm. Typical features of 1D superconductivity such as non

zero resistance below T_c as well as hysteresis and finite jumps in the I - V characteristics have been observed in our samples.

5.2 Sample fabrication

Porous layers have been fabricated by electrochemical anodic etching of n-type, 0.01 Ωcm , monocrystalline silicon wafers. The electrochemical dissolution has been performed in 48% water solution of HF, applying a current density of 20 mA/cm². The anodization time was chosen in the range of 0.5 - 4 min in order to get porous layers with a thickness ranging from 0.5 to 4 μm . The pores extend on a surface of about 1 cm². The integral porosity has been estimated by gravimetry to be of about 50% [18]. The resulting porous substrates have diameter $\varnothing = 10$ nm and interpore spacing (center-center distance) $a = 20$ -40 nm. Nb thin films have been grown on top of the porous Si substrates in an UHV dc diode magnetron sputtering system with a base pressure in the low 10^{-8} mbar regime and sputtering Argon pressure of 3.5×10^{-3} mbar. In order to reduce the possible contamination present in the porous templates, the substrates have been heated at 120°C for one hour in the UHV chamber. The deposition was then realized at room temperature after the cool off of the substrates. The films have been deposited at typical rates of 0.33 nm/s, controlled by a quartz crystal monitor calibrated by low-angle X-ray reflectivity measurements. In this way, an array of interconnected superconducting wires was formed on the substrates, the single wire width, w , being the distance between the edges of two consecutive pores. Therefore is $w = 10$ nm (30 nm) for the sample grown on the substrate with $a = 20$ nm (40 nm). It is worth underling that the single wire width, w , is comparable with the zero-temperature superconducting coherence length of our samples, $\xi(0) \simeq 10$ nm [19]. Since the effect of the periodic template would be reduced when the film thickness, d_{Nb} , exceeds the pore diameter, \varnothing [19, 20], the Nb thickness was chosen to be in the

range of 9 nm - 12 nm. Finally, a typical four-probe geometry has been realized on the samples by using standard optical lithography. The dimensions of the obtained bridges were $\Lambda = 10\text{-}20 \mu\text{m}$ for the width and $L = 100 \mu\text{m}$ for the length.

5.3 Experimental results and discussion

The superconducting properties were resistively measured in a ^4He cryostat using a standard dc four-probe technique.

All the Nb films deposited on porous Si, their names and thicknesses, as well as the substrate characteristics are summarized in Table 5.1. For the sake of clarity the samples were named using the initials Si followed by a number indicating the nominal interpore distance, a , Nb by a number indicating the Nb thickness and by another number for the bridge width. For example, Si40-Nb12- Λ 20 is the porous Nb bridge 20 μm wide and 12 nm thick, grown on the porous substrate with $a = 40$ nm.

Sample	$a(\text{nm})$	$d_{\text{Nb}}(\text{nm})$	$\Lambda(\mu\text{m})$	$T_c(\text{K})$
Si20-Nb9- Λ 10	20	9	10	3.60
Si40-Nb10- Λ 10	40	10	10	4.23
Si40-Nb12- Λ 20	40	12	20	3.87

Table 5.1: Characteristics of porous Si templates and properties of Nb films deposited on such substrates. a indicates the interpore spacing, d_{Nb} the Nb thickness, Λ the bridge width, T_c the critical temperature. The pore diameter \varnothing is 10 nm for all the samples.

From the a , \emptyset and Λ values of the analyzed samples we can estimate the number of the interconnected wires present in each bridge which are 330 for Si20-Nb9- Λ 10, 200 for Si40-Nb10- Λ 10 and 400 for Si40-Nb12- Λ 20. The numbers listed above are likely to be corrected considering a deviation from the corresponding mean interpore distance of the order of 10% [19]. A schematic representation showing the sample Si20-Nb9- Λ 10 is reported in figure 5.1.

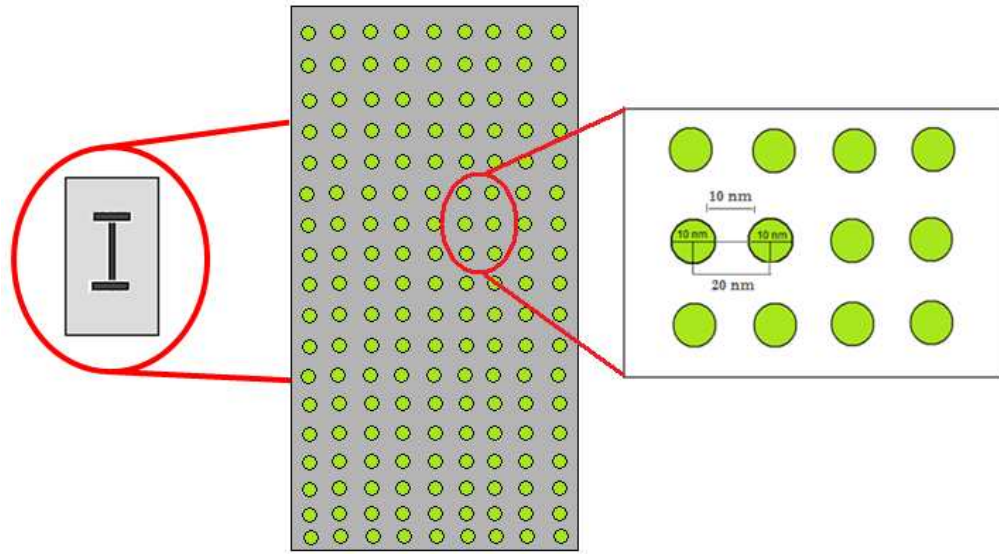


Figure 5.1: A schematic representation showing the sample Si20-Nb9- Λ 10. The single wire width, w , being the distance between the edges of two consecutive pores is $w = 10$ nm for this sample grown on the substrate with $a = 20$ nm.

5.3.1 Resistive transition

Superconducting nanowires never show zero resistance, although resistance does decrease exponentially upon cooling [6]. As already discussed in the first chapter, the origin of this resistive behavior lies in the occurrence of thermally activated slips of the phase of the Ginzburg-Landau order parameter. During a phase slip, a small normal segment appears on the nanowire for a short time causing the loss of phase coherence

[21]. In Fig. 5.2 are reported the $R(T)$ transition curves, normalized to the resistance at 10 K, of porous Nb bridges of different widths and thicknesses grown on the porous substrates Si20 and Si40, namely samples Si40-Nb10- Λ 10 and Si40-Nb12- Λ 20. For each curve, we observe a first resistance drop at higher temperature which corresponds to the superconducting transition of the larger Nb porous electrodes [4, 12]. The resistance value immediately below this drop is taken as the normal resistance R_N of the interconnected wires. The critical temperature values estimated at the midpoint of the $R(T)$ transition curves are reported in Table 5.1.

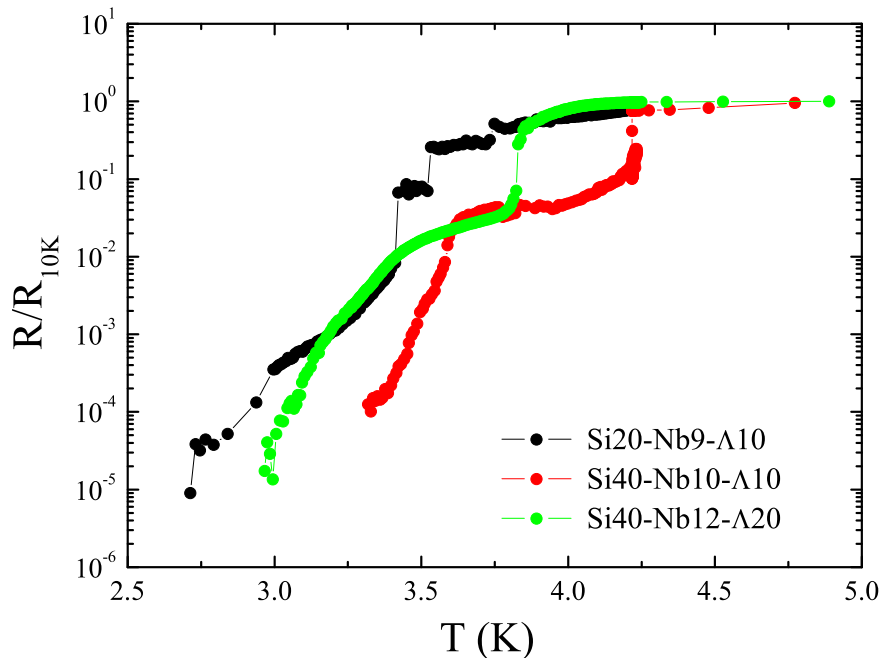


Figure 5.2: $R(T)$ transition curves, normalized to the resistance at $T = 10$ K, of Nb ultrathin bridges of different widths and thicknesses grown on the porous substrates Si20 and Si40.

Moreover, it can be observed that the samples exhibit a nonzero resistance over a large temperature range. This behavior, typical of 1D system, can be compared to the one shown in Figs. 1.21 and 1.28(a). The width of the resistance transitions, defined as $\Delta T_c = T_c^{90\%R_N} - T_c^{10\%R_N}$, reaches in fact values up to 0.6 K for the sample Si20-Nb9- Λ 10, namely in the case of the narrowest values. Also, it is worth underlining

that the resistance of the samples drops about five orders of magnitude within this temperature range below T_c . These curves are significantly broader than the ones observed in similar plane porous Nb films [19], reported, for sake of comparison, in Fig. 5.3 where $\Delta T_c \sim 0.2$ K. These films were also grown on porous Si substrates but, since they were unpatterned, a much larger number of interconnected superconducting wires were present and consequently the superconducting properties, typical of 1D systems, were not observed. Moreover this comparison between patterned and unpatterned samples makes us confident to exclude that sample dishomogeneity (i.e. granularity) can be responsible of the $R(T)$ broadening [22].

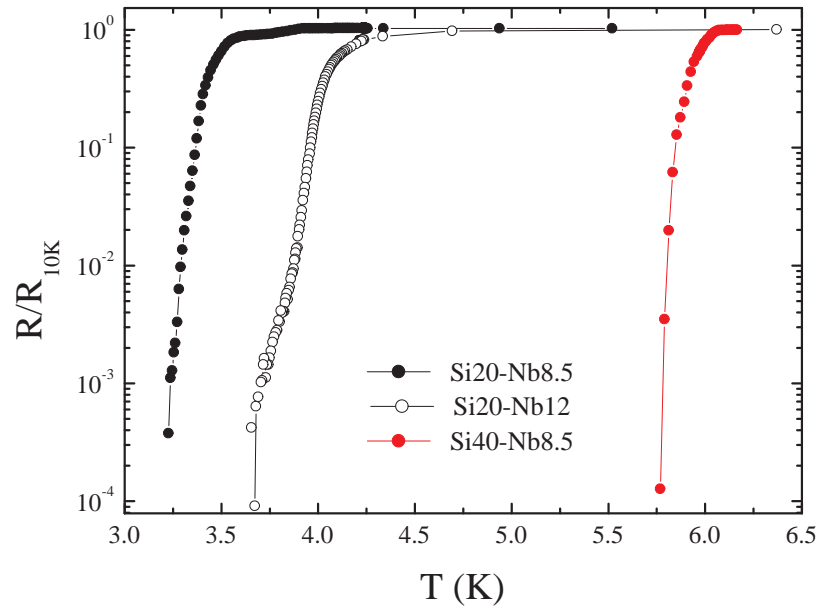


Figure 5.3: $R(T)$ transition curves, normalized to the resistance at $T = 10$ K, of plane porous Nb films of different thicknesses grown on the porous substrates Si20 and Si40.

5.3.2 I - V measurements

I - V characteristics have been measured at different temperatures and magnetic fields under current drive condition. The magnetic field was applied perpendicularly to the plane of the substrate. During the measurement the temperature stabilization was around 1 mK. In order to minimize any heating effect the bridges have been kept in contact with liquid helium. The current biasing has been realized by sending rectangular current pulses to the samples, with the current-on time being of 12 ms followed by a current-off time of 1 s. Any single voltage value has been acquired at the maximum value of the current. Here we report the current-voltage characteristics for the sample Si20-Nb9- Λ 10, which shows the maximum value of ΔT_c . In Fig. 5.4 I - V curves measured at different applied magnetic fields and at the temperature of 3.53 K ($t = 0.95$), are shown. All the curves were recorded sweeping the current up and down and clear hysteresis has been detected. Finite jumps were also observed, as highlighted in the inset of Fig. 5.4, providing further evidence that phase slip phenomena are present since each jump corresponds to phase slip lines entering the sample [23, 24]. This behavior is very similar to that reported in Fig. 1.32. When the current is swept down a continuous behavior is found without any jump between different resistive states. On the contrary, during the sweeping up we can notice that the voltage progression is peaked instead of following monotonic steps [23, 24]. We believe that such behavior is related to the fact that in the interconnected wires there is a competition between 1D and non-1D superconductivity [25].

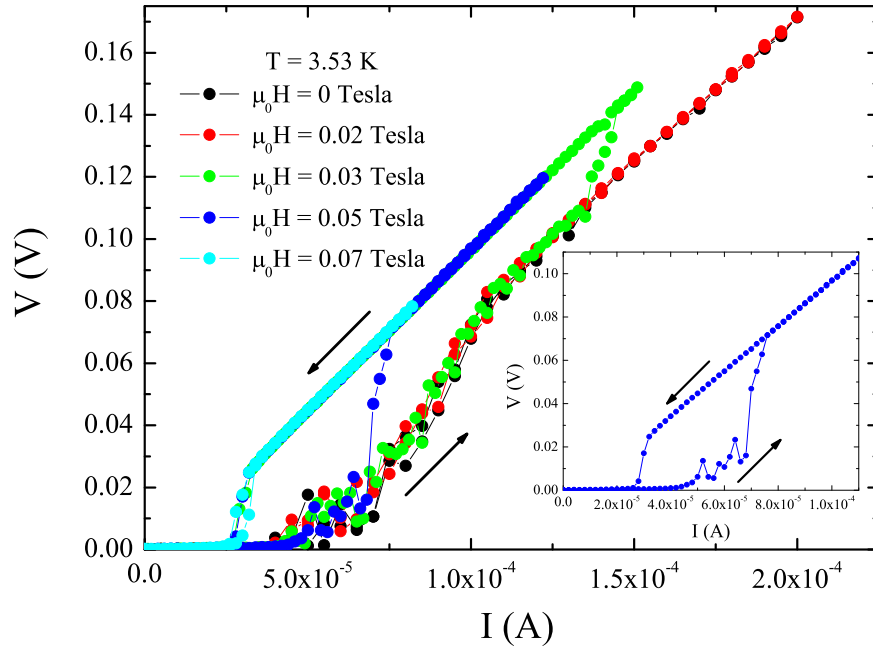


Figure 5.4: *Current-voltage characteristics of the sample $\text{Si}_{20}\text{-Nb}_9\text{-}\Lambda_{10}$ at different applied magnetic fields and at $T = 3.53$ K. The inset is an enlargement of the I - V measurement at $\mu_0 H = 0.05$ Tesla.*

The hysteresis in the I - V curves disappears increasing the applied magnetic field.

Again for the sample $\text{Si}_{20}\text{-Nb}_9\text{-}\Lambda_{10}$, in figure 5.5 I - V curves measured at different applied magnetic fields at the temperature of 3.30 K ($t = 0.88$), are shown. Clear hysteresis and finite jumps were again observed.

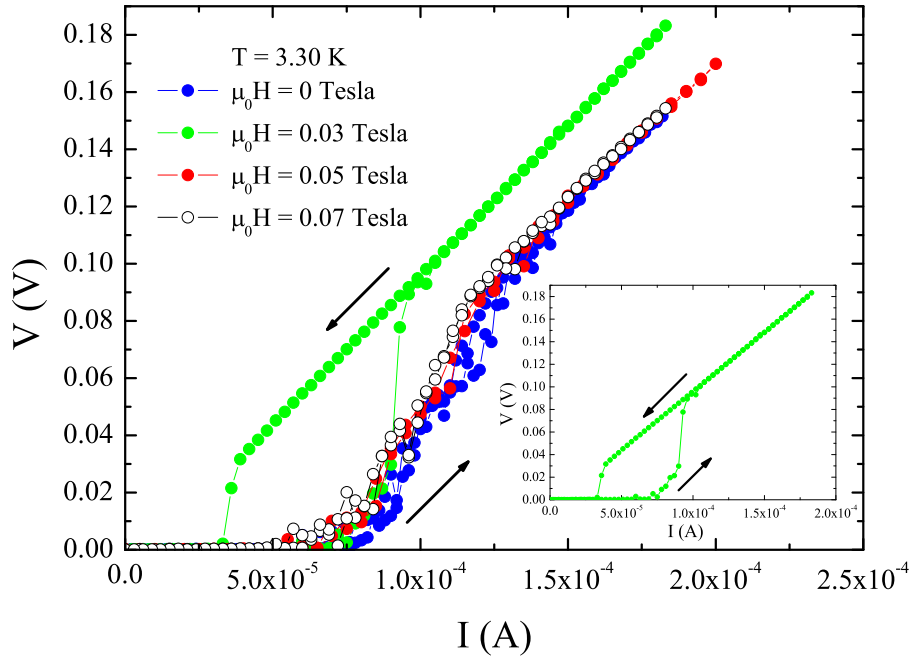


Figure 5.5: *Current-voltage characteristics of the sample Si20-Nb9- Λ 10 at different applied magnetic fields and at $T = 3.30$ K. The inset is an enlargement of the I - V measurement at $\mu_0 H = 0.03$ Tesla.*

Comparing Figs. 5.4 and 5.5, we can observe that at the lowest reduced temperature the hysteresis disappears at a lower applied magnetic field than the ones detected at the reduced temperature $t = 0.95$.

In conclusion, we have studied transport properties of superconducting Nb ultrathin bridges grown on porous Si substrates where the pore diameter is 10 nm and the interpore spacing is 20-40 nm. The samples exhibit a nonzero resistance over a broad temperature range and clear hysteresis with finite jumps in the I - V curves. These features are more pronounced in the sample Si20-Nb9- Λ 10 which is characterized by the narrowest value of the single superconducting wire widths. All these observations are typical of 1D superconductivity.

Bibliography

- [1] A.V. Herzog, P. Xiong, F. Sharifi, and R.C. Dynes, Phys. Rev. Lett. **76**, 668 (1996).
- [2] P. Xiong, A.V. Herzog, and R.C. Dynes, Phys. Rev. Lett. **78**, 927 (1997).
- [3] D.Y. Vodolazov, F.M. Peeters, L. Piraux, S. Mátéfi-Tempfli, and S. Michotte, Phys. Rev. Lett. **91**, 157001 (2003).
- [4] A. Rogachev, A.T. Bollinger, and A. Bezryadin, Phys. Rev. Lett. **94**, 017004 (2005).
- [5] M.L. Tian, N. Kumar, S.Y. Xu, J.G. Wang, J.S. Kurtz, and M.H.W. Chan, Phys. Rev. Lett. **95**, 076802 (2005).
- [6] K.Y. Arutyunov, D.S. Golubev, and A.D. Zaikin, Physics Reports **464**, 1 (2008).
- [7] M. Zgirski, K.P. Riikonen, V. Touboltsev, and K. Arutyunov, Nano Lett. **5**, 1029 (2005).
- [8] F. Altomare, A.M. Chang, M.R. Melloch, Y.G. Hong, and C.W. Tu, Phys. Rev. Lett. **97**, 017001 (2006).
- [9] X.Y. Bao, Y.F. Zhang, Y.P. Wang, J.F. Jia, Q.K. Xue, X.C. Xie, and Z.X. Zhao, Phys. Rev. Lett. **95**, 247005 (2005).
- [10] D.S. Golubev and A.D. Zaikin, Phys. Rev. B **64**, 014504 (2001).
- [11] N. Giordano, Phys. Rev. Lett. **61**, 2137 (1988).

- [12] C.N. Lau, N. Markovic, M. Bockrath, A. Bezryadin, and M. Tinkham, *Phys. Rev. Lett.* **87**, 217003 (2001).
- [13] J. Ku, V. Manucharyan, and A. Bezryadin, *Phys. Rev. B* **82**, 134518 (2010).
- [14] D.E. McCumber and B.I. Halperin, *Phys. Rev. B* **1**, 1054 (1970).
- [15] A.D. Zaikin, D.S. Golubev, A. van Otterlo, and G.T. Zimanyi, *Phys. Rev. Lett.* **78**, 1552 (1997).
- [16] S. Michotte, L. Piraux, S. Dubois, F. Pailloux, G. Stenuit, and J. Govaerts, *Physica C* **377**, 267 (2002).
- [17] S. Michotte, S. Mátéfi-Tempfli, and L. Piraux, *Appl. Phys. Lett.* **82**, 4119 (2003).
- [18] S.K. Lazarouk, A.V. Dolbik, V.A. Labunov, and V.E. Borisenko in *Physics, Chemistry and Application of Nanostructures*, World Scientific 223, (2007).
- [19] M. Trezza, S.L. Prischepa, C. Cirillo, R. Fittipaldi, M. Sarno, D. Sannino, P. Ciambelli, M.B.S. Hesselberth, S.K. Lazarouk, A.V. Dolbik, V.E. Borisenko, and C. Attanasio, *J. Appl. Phys.* **104**, 083917 (2008).
- [20] M. Trezza, C. Cirillo, S.L. Prischepa, and C. Attanasio, *Europhys. Lett.* **88**, 57006 (2009).
- [21] D.S. Hopkins, D. Pekker, P.M. Goldbart, and A. Bezryadin, *Science* **308**, 1762 (2005).
- [22] A.V. Herzog, P. Xiong, and R.C. Dynes, *Phys. Rev. B* **58**, 14199 (1998).
- [23] P. Mikheenko, X. Deng, S. Gildert, M.S. Colclough, R.A. Smith, C.M. Muirhead, P.D. Prewett and J. Teng, *Phys. Rev. B* **72**, 174506 (2005).
- [24] A.K. Elmurodov, F.M. Peeters, D.Y. Vodolazov, S. Michotte, S. Adam, F. de Menten de Horne, L. Piraux, D. Lucot, and D. Mailly, *Phys. Rev. B* **78**, 214519 (2008).

- [25] G.C. Tettamanzi, A. Potenza, S. Rubanov, C.H. Marrows, and S. Prawer, *Nanotechnology* **21**, 168002 (2010).

Conclusions

It is well known that the use of regular array of pinning centers such as antidots or magnetic dots brings to new commensurability effects between the vortex lattice and the pinning array, giving additional insight into the pinning properties of superconducting materials. The most notable phenomenon for these studies is the so-called matching effect which occurs when the vortex lattice is commensurate with the periodic pinning array. If the artificial structure of defects is created by lithographic technique, the matching fields are usually in the range of a few Oersteds and consequently matching effects are observed only in a very narrow temperature region, close to the critical temperature T_c , for a reduced value $t = T/T_c \geq 0.95$. In order to both increase the matching field and decrease the temperature where the effect is present, the period of the pinning structure should be reduced to less than 100 nm. This gives, in fact, the possibility to increase the first matching field H_1 up to 1 Tesla or even higher. A reasonable method to achieve this goal is to use self-assembled substrates.

In this thesis porous silicon was used as self-assembled substrate to grow Nb ultra-thin films (thickness of the order of 10 nm). For general applications, porous silicon is a very promising and attractive material due to its excellent mechanical and thermal properties, its obvious compatibility with silicon-based microelectronics, its quick formation process and its low cost. Moreover, Si based substrates are good candidates for the Nb growth and the characteristic pore features of these substrates are the smallest used in superconducting field. In fact, the period of the pores array is smaller than the one obtained by typical lithographic techniques of more than one

order of magnitude and smaller dimensions imply high matching fields down to lower temperatures. Resistive transitions on perforated Nb ultrathin films with a lattice of holes with the period of the order of ten nanometers were shown in chapter 3. Due to the extremely reduced values of the interpore distance matching effects are present for fields higher than 1 Tesla and down to reduced temperatures as low as $t \simeq 0.52$. The commensurability manifests both in the (H, T) phase diagram and in the $R(H)$ transitions. In particular, the latter reveals the formation of fractional matching states. This effect has been related to different vortex lattice configurations made available by the underlying lattice of holes.

In addition to regular array of holes (antidots) more recently the use of ferromagnetic materials as pinning centers has attracted much attention. The introduction of the ferromagnetic dots produce an enhancement of the superconducting properties and matching effects are more pronounced. However, also for this case, the observation of matching effects were restricted up to now to relatively low magnetic fields and high temperatures. Nanoporous alumina templates were used to grow dense arrays of ferromagnetic nanowires serving as magnetic pinning centers in the nearby Nb ultrathin films. As a consequence of the high density of the pore network, the (H, T) phase diagram presents a deviation from the classic linear dependence up to the 3rd matching field. The interaction between the nanowires array and the thin superconducting film has been recognized also through an appreciable enhancement of the critical temperature with respect to the case of a Nb film deposited on a plain alumina substrate. These results were reported in chapter 4 of this thesis.

Finally, in chapter 5 we investigated the transport properties of superconducting Nb ultrathin bridges deposited on porous silicon. With respect to the films studied in chapter 3 in these patterned samples a much smaller number of interconnected superconducting wires were present. The samples exhibit a nonzero resistance over a broad temperature range (up to five orders of magnitude) and clear hysteresis with finite jumps in the I-V curves. Both these observations are typical for 1D superconductors.

Publications

1. **M. Trezza**, S.L. Prischepa, C. Cirillo, R. Fittipaldi, M. Sarno, D. Sannino, P. Ciambelli, M.B.S. Hesselbert, S.K. Lazarouk, A.V. Dolbik, V.E. Borisenko, and C. Attanasio, *Superconducting properties of Nb thin films deposited on porous silicon templates*, J. Appl. Phys. **104**, 083917 (2008).
2. **M. Trezza**, C. Cirillo, S.L. Prischepa, and C. Attanasio, *Evidence of fractional matching states in nanoperforated Nb thin film grown on porous silicon*, Europhys. Lett. **88**, 57006 (2009).
3. **M. Trezza**, C. Cirillo, C. Attanasio, A.V. Dolbik, and S.L. Prischepa, *Transport properties of Nb thin films deposited on porous Si substrates*, in “Physics, Chemistry and Application of Nanostructures”, V.E. Borisenko, S.V. Gaponenko, and V.S. Gurin Editors, pag. 220, World Scientific, Singapore (2009).
4. **M. Trezza**, S.L. Prischepa, C. Cirillo, and C. Attanasio, *Transport properties of nanoperforated Nb thin films*, Physica C **470**, 957 (2010).
5. P. Sabatino, C. Cirillo, G. Carapella, **M. Trezza**, and C. Attanasio, *High field vortex matching effects in superconducting Nb thin films with a nanometer-sized square array of antidots*, J. Appl. Phys. **108**, 053906 (2010).
6. S.V. Redko, E.B. Chubenko, A.A. Klyshko, K.I. Kholostov, V.P. Bondarenko, S.L. Prischepa, **M. Trezza**, C. Cirillo, and C. Attanasio, *Temperature dependence of resistivity of porous Silicon formed on n+ substrates*, in “Nanomaterials:

Applications and Properties ”, A. Progrebnjak, T. Lyutyty, and S. Protsenko Editors, pag. 320 (2011).

7. **M. Trezza**, S.L. Prischepa, C. Cirillo, and C. Attanasio, *1D superconductivity in porous Nb ultrathin films*, Physica C, accepted for publication (doi: 10.1016/j.physc.2012.01.001).
8. **M. Trezza**, C. Cirillo, A.I. Vorobjeva, E.A. Outkina, S.L. Prischepa, and C. Attanasio, *Vortex pinning with artificial magnetic nanostructures*, in preparation.
9. **M. Trezza**, C. Cirillo, S.L. Prischepa, and C. Attanasio, *Phase-slip phenomena in porous Nb ultrathin films*, in preparation.

Acknowledgments

I would like to express my gratitude to all those who gave me the possibility to complete this thesis and supported me in the course of these three years.

First and foremost, I would like to thank my thesis advisor Prof. Carmine Attanasio for encouraging me to undertake the PhD giving me the opportunity to work on such an exciting project. I'm grateful to him for his continual support and his precious advices. I have learned more from him than he probably knows.

A big thank you to Dr. Carla Cirillo for her help training me in everything from samples fabrication to data analysis, for always keeping the atmosphere in the lab very enjoyable, for her encouragement and especially for her friendship.

I am also grateful to Prof. S.L. Prischepa for sharing nice and long measuring days in the lab, and for the stimulating discussions about physics and anything else.

Many colleagues and Professors provided valuable information that helped me during the work of the last three years, and I am grateful to all of them for their assistance.

I would like to express my love to my family, thank you for your constant support and for always believing that I would succeed. Thank you to all my good friends. Even though I cannot name them all here, I will always cherish their support and the time spent with them.